MODELING AND UNDERSTANDING CORONAL LOOP DYNAMICS DURING SOLAR FLARES

by

John Edward Unverferth IV

A dissertation submitted in partial fulfillment
of the requirements for the degree

of

Doctor of Philosophy

in

Physics

MONTANA STATE UNIVERSITY
Bozeman, Montana

July 2020

ACKNOWLEDGEMENTS

First, I would like to thank my advisor Dana Longcope for the patience and time he has put into helping me become the scientist I am today. Also, I appreciate the guidance and advice that my committee members have provided over the course of my graduate studies. I would like to thank my parents, Jack Unverferth and Beth Unverferth, for encouraging me to learn about science and follow my passion for it. Thanks so much to Margaret Jarrett, without her advice I would not have made it this far. Also, thanks to the many friends who have helped me through, including the other graduate students who were in my year. Without them this would have been much harder, if not impossible.

TABLE OF CONTENTS

TABLE OF CONTENTS – CONTINUED

LIST OF TABLES

LIST OF FIGURES

LIST OF FIGURES – CONTINUED

LIST OF FIGURES – CONTINUED

Figure Page

LIST OF FIGURES – CONTINUED

LIST OF FIGURES – CONTINUED

Figure Page

LIST OF FIGURES – CONTINUED

LIST OF FIGURES – CONTINUED

LIST OF FIGURES – CONTINUED

LIST OF FIGURES – CONTINUED

LIST OF FIGURES – CONTINUED

Figure Page

LIST OF FIGURES – CONTINUED

LIST OF FIGURES – CONTINUED

LIST OF FIGURES – CONTINUED

ABSTRACT

Magnetic reconnection is widely considered to be the mechanism behind solar flares. Models powered by reconnection manage to explain many of the observational features seen in a flare. However, these models miss or contradict important elements of the flare. Here we consider three effects overlooked by models. First, the role played by the magnetic canopy in determining the chromospheric response in a flare. Second, how variations in magnetic field strength along the current sheet impact the evolution of flare loops. Third, how flux tube interactions with the current sheet can lead to sub-Alfvénic motion, bringing dynamics in line with observations. These three effects were investigated with the use of one dimensional and thin flux tube models. This allowed for the dynamics to be considered independent of the reconnection process that generated the flux tubes. The canopy interaction revealed that the creation of an expansion followed by a constriction, a chamber in the flux tube, leads to multiple solutions. The solutions include smooth flow and standing shocks in the chamber. The standing shock increases the emission of the flow, as well as slowing it to subsonic speeds. The shocked solution shifts the ensemble of flux tubes to have a distribution that would indicate slower speeds than expected. The structure of the current sheet magnetic field leaves a signature on the flux tube. Each case leads to a difference in emission. Retraction through a constricting field creating a plug of material leading to a bright emission in the apex. This contrasts with retraction through an expanding field which generates high temperatures, but as a fainter emission. The interaction of drag in the current sheet allowed for the retraction to proceed at slower rates. The slower retraction matches observations of features in flares more accurately. The slower retraction also increases the brightness of the synthetic current sheet. This increased brightness brings the current sheet closer to the observed brightness. These investigations found that there was benefit to considering these additional effects. Each one of these effects was found to bring the models more in line to what observations note.

CHAPTER ONE

INTRODUCTION

The solar atmosphere is a complex, layered, structure reaching outward from the surface of the Sun. The extent to which it extends varies depending upon the definition of the outer edge, but reaches out many solar radii (Carroll & Ostlie, 2007; Schrijver & Siscoe, 2011). Activity in the solar atmosphere is a primary driver of magnetospheric and planetary atmospheric responses (Lemen et al., 2012). The energy that the solar atmosphere emits comes from the core of the Sun, where fusion releases massive quantities of energy (Zirin, 1988; Foukal, 1990; Carroll & Ostlie, 2007). This energy is then carried outward by convection and radiation (Zirin, 1988; Foukal, 1990; Schrijver & Siscoe, 2011). As the energy diffuses outward from the core, it must flow down a temperature gradient, which leaves each successive shell of material cooler. This leads to the surface of the Sun being around 6000 kelvin while the core is thought to be around fifteen million kelvin (Foukal, 1990; Carroll & Ostlie, 2007). This cooling trend reverses a short distance above the surface resulting in the upper atmosphere reaching millions of kelvin (Zirin, 1988; Foukal, 1990). This so-called 'coronal heating problem' and the mechanism behind it have driven decades of solar studies along with dozens of space-based observatories and missions (Zirin, 1988; Foukal, 1990).

The atmosphere starts at the surface, set by the optical depth of the plasma reaching unity (Carroll & Ostlie, 2007). This layer, the photosphere, is where plasma reaches a critical density that allows for the escape of light instead of reabsorption (Carroll & Ostlie, 2007). As mentioned above, the plasma here is relatively cool at

6000 kelvin and light here is primarily emitted as a continuum reminiscent of a black body at that temperature (Carroll & Ostlie, 2007; Schrijver & Siscoe, 2011). Due to the relatively low temperatures, plasma here is not fully ionized and so signatures of neutral atoms and even molecular species are observed (Faurobert & Arnaud, 2002; Penn et al., 2016; Jaeggli et al., 2018). The primary driver of dynamics in the photosphere is convective motions (Zirin, 1988; Foukal, 1990; Carroll & Ostlie, 2007). These take the form of a random pattern of convective cells dredging up hotter material from deeper within the Sun (Zirin, 1988; Foukal, 1990; Carroll & Ostlie, 2007). This pattern on the solar surface is collectively called granulation with each individual cell referred to as a granule (Zirin, 1988; Foukal, 1990; Carroll & Ostlie, 2007).

Above the photosphere lies the chromosphere. The temperature in the chromosphere is significantly hotter than the photosphere, ranging from approximately 10,000 to 100,000 kelvin (Carroll & Ostlie, 2007). The chromosphere is also less dense than the photosphere, and this decreases further as altitude increases (Zirin, 1988; Foukal, 1990; Schrijver & Siscoe, 2011). The higher temperature and the reduced density contribute to the difficulty of observing the chromosphere in the visible continuum, as it is outshone by the photosphere (Carroll & Ostlie, 2007). This level of the atmosphere is complex, displaying a highly dynamic layer (Zirin, 1988; Foukal, 1990; Solanki & Steiner, 1990; Rutten, 2007; Hasan, 2008; Schrijver & Siscoe, 2011). The range of temperatures in the chromosphere allow for the formation of many different ionized species (Carroll & Ostlie, 2007). Careful analysis of spectral lines from these species offers insight into the evolution and dynamics of the chromosphere (Rutten, 2007).

Above the chromosphere is a thin region of rapidly increasing temperature plasma which results in the so-called transition region (Carroll & Ostlie, 2007). This is the interface between the chromosphere below and the corona above. It fluctuates depending on energy release in either region, often being pushed downward by activity in the corona (Fisher et al., 1985; Schrijver & Siscoe, 2011). This layer is thin due to the increased thermal conductivity in plasma as the temperature rises (Schrijver & Siscoe, 2011).

The corona is the outermost layer of the solar atmosphere (Carroll & Ostlie, 2007). It begins above the transition region and extends to the beginning of the solar wind (Carroll & Ostlie, 2007). This layer continues the trend of decreasing density, with the densities here being lower than the chromosphere and transition regions (Carroll & Ostlie, 2007). This tenuous plasma is the hottest in the solar atmosphere, being heated to millions of kelvins (Carroll & Ostlie, 2007). Higher resolution observations of the corona brought a surprise. Instead of appearing similar to the regions below, the corona appears organized into collections of loops connecting distant points on the solar surface (Zirin, 1988; Foukal, 1990; Schrijver & Siscoe, 2011; Reale, 2014). Investigations showed this to be the result of the presence of strong magnetic fields (Zirin, 1988; Foukal, 1990; Schrijver & Siscoe, 2011). These fields confine the plasma along their length (Zirin, 1988; Foukal, 1990; Schrijver & Siscoe, 2011). Further investigations show some of these field lines are closed, creating the visible loops, while others open to the interplanetary medium and contribute to the solar wind streaming off the Sun (Zirin, 1988; Foukal, 1990; Schrijver & Siscoe, 2011).

This chapter is divided into several sections to provide a background of important concepts that will be needed later on. Each section builds upon the previous, and seeks to provide enough information on its topic that the subsequent sections and chapters are clear. The intent is to establish an understanding of the field prior to the work presented in Chapters 2-4. Section 1 introduces the concept of a magnetic active region. In Section 2 we consider the most energetic event in the solar system, a solar flare. Magnetic reconnection is the focus of Section 3 where we discuss this plasma phenomenon that powers these outbursts in the corona. Section 4 introduces the thin flux tube model, a useful tool that is used heavily in Chapters 3 and 4. Section 5 explores unsolved questions that motivate the work presented in the following chapters.

1.1 Solar Active Regions

Solar active regions are areas of intense magnetic activity in the solar atmosphere (van Driel-Gesztelyi & Green, 2015). The plasma that makes up the Sun is host to a strong magnetic field below the surface generated by the solar dynamo (Parker, 1975). The large-scale field resembles a dipole when viewed at a distance, depending on solar activity (Zirin, 1988; Foukal, 1990; Schrijver & Siscoe, 2011; Sanderson et al., 2003; Carroll & Ostlie, 2007; Michael et al., 2018). Close to the surface, the field shows more complexity and can be considered in two components: network flux and magnetic active regions. Supergranulation and granulation dredge material up from deeper in the Sun, and move around small elements of flux, referred to as network flux which forms on the boundaries of supergranules (Howard & Stenflo, 1972; Muller, 1983; Zwaan, 1987; Berger & Title, 1996). The other component is a more compact and organized collection of flux, a magnetic active region (Zwaan, 1987).

Magnetic active regions alter the appearance of the plasmas they are embedded in. In the photosphere, active regions tend to either darken or brighten plasma. The magnetic field strength in an active region can reach thousands of gauss (Livingston, 2002). Strong magnetic fields generate a magnetic pressure, which contributes to the total pressure. This contribution leads to a reduction in the gas density to maintain total pressure balance in the region of flux (Foukal, 1990; Priest, 2014). This results in bright points as the reduced density allows for a deeper line of sight, which then

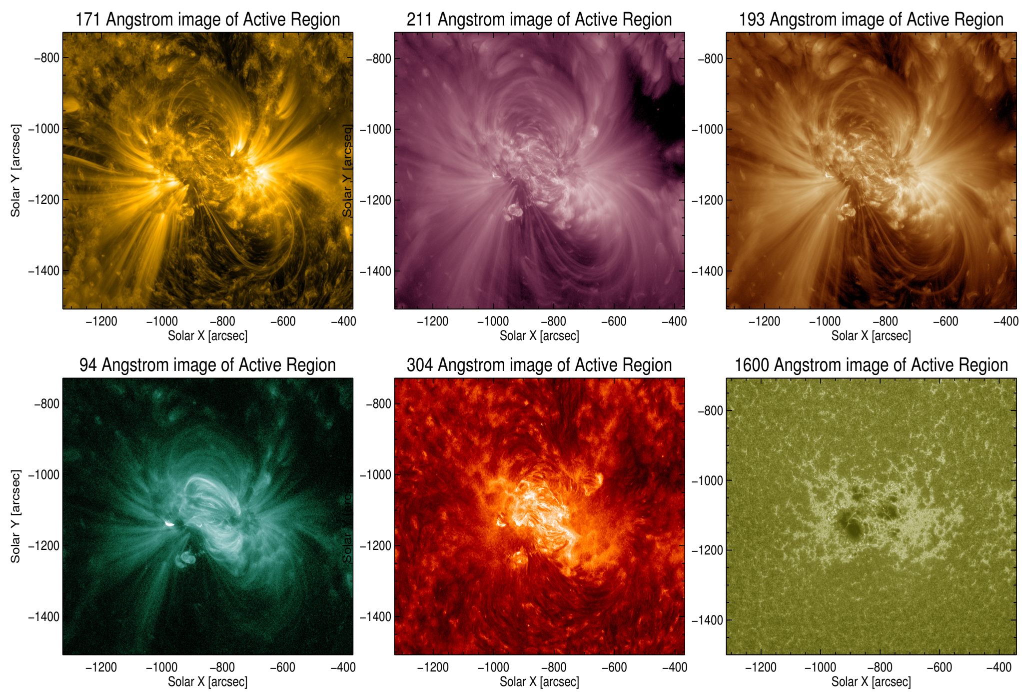

Figure 1.1: Solar active region observed in multiple wavelengths. Top row and bottom left observing in iron emission lines at coronal temperatures (Lemen et al., 2012). Bottom middle observing in helium-II, showing cooler emission lower down(Lemen et al., 2012). Bottom right shows much cooler emission from carbon-IV near the bottom of the atmosphere (Lemen et al., 2012).

reveals hotter material (Berger & Title, 1996; Nisenson et al., 2003). Active regions can create an area with similar enhanced brightness, known as plage (Muller, 1983; Zirin, 1988; Foukal, 1990; Priest, 2014).

Strong enough magnetic field has a different effect. Instead of small brightenings, the plasma becomes dark and cool (Zwaan, 1987). Strong enough magnetic field has the ability to suppress convection, trapping hot plasma below (Zirin, 1988; Foukal, 1990; Priest, 2014). The suppressed convection increases the turnover time of the plasma, which remains at the surface longer and cools more as a result (Zirin, 1988). This cooler material radiates less than its surroundings, appearing dark on the surface (Zirin, 1988). Due to this striking contrast, we have records of sunspots going back several centuries, starting roughly with the development of the telescope, with more fragmentary records dating back further (Carrington, 1859b; Foukal, 1990; Solanki, 2003). In Fig. 1.1 there is an active region viewed in six different wavelengths, highlighting different regions of the atmosphere. The lower right panel shows the darkening explained above, while the other panels show emission from different regions of the solar atmosphere. The bottom middle panel shows emission in 304 Å, light emitted by singly ionized helium.

Active regions contain more than just photospheric emission in the visible, however. The top row of panels and the lower left panel show emission in the corona from different ionized states of iron. These regions show different responses to the presence of magnetic fields. In the higher atmosphere, the plasma is more visible in other wavelengths where different mechanisms contribute to the emissivity (Zirin, 1988; Foukal, 1990; Schrijver & Siscoe, 2011). These other wavelengths present observational challenges: needing precise interferometric measurements in the radio to resolve spatial detail, or space-borne observatories to see past Earth's atmospheric absorption in ultraviolet and X-rays (Zirin, 1988; Foukal, 1990; Schrijver & Siscoe, 2011).

1.1.1 Evolution and Structure

The magnetic flux that comprises an active region is sourced from the solar interior in the convection zone (Parker, 1975). In the interior a twisted collection of flux reaches total pressure balance with its surrounding. For a magnetized plasma the magnetic field contributes to the total pressure (Foukal, 1990; Priest, 2014). Consequently, this flux rope is less dense due to the higher field. With the same temperature, and less material, the flux rope is buoyant and rises through the solar interior (Zwaan, 1987). When the rope reaches the surface, it pokes through and

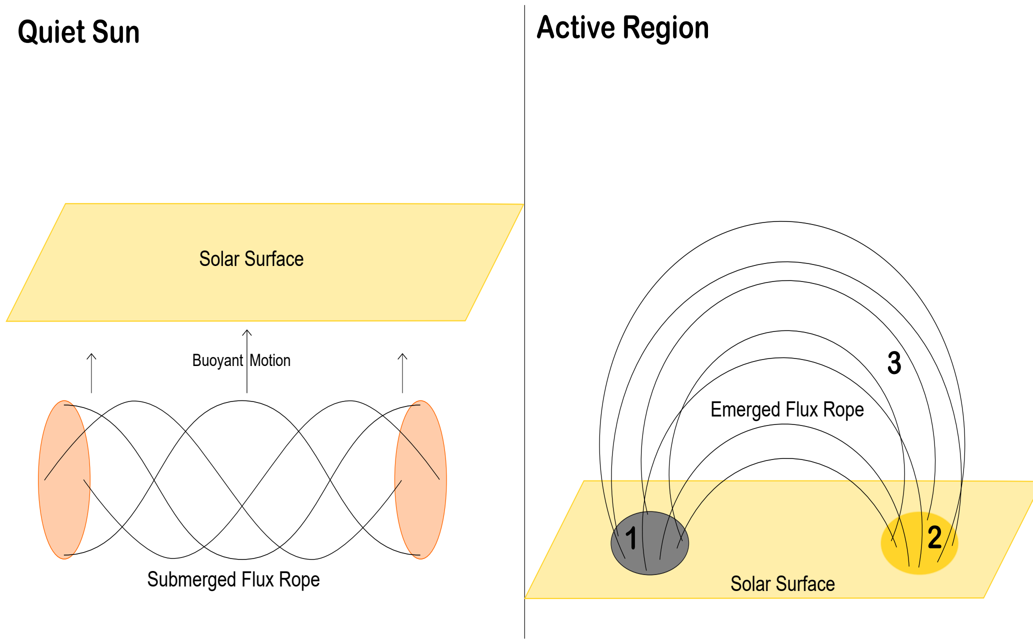

Figure 1.2: Cartoon depicting the emergence of a flux rope from the convective interior into the atmosphere. The initially submerged flux rope becomes buoyant and breaches the surface. There the fields(3) spread to connect the two regions of the flux rope. These surface regions may form sunspots(1) or plage(2) where the flux rope enters the surface.

unfurls into the atmosphere. Now there is a large, on the order of $10^{20} - 10^{22}$ Mx, collection of flux anchored between the two ends of the emerged flux rope (Zwaan, 1987; Kazachenko et al., 2017).

Once the active region is established, if the field is compact and strong enough, it will slow convection and lead to a sunspot at one or both ends (Zirin, 1988). Typically, the leading footpoint is more compact than the trailing one (Lites et al., 1998). Over time the flux is spread out by photospheric motions (McIntosh, 1981; Foukal, 1990). This results in the weakening and eventual breakup of the active region (McIntosh, 1981; Foukal, 1990).

The active region exists from the photosphere to corona, and the evolution in each layer is governed by the interplay of the gas pressure and the magnetic field (Priest, 2014). As the plasma rises, the relative importance of gas pressure and the magnetic field can be evaluated with a ratio known as the plasma beta. Plasma beta is the ratio of the gas to magnetic pressure in a magnetic plasma, $\beta = 8\pi P/B^2$ (Priest, 2014). A value of plasma beta larger than one indicates that the gas dynamics guide the motion, and values below one indicate that the magnetic field guides the motion (Priest, 2014). Intermediate values are a complex case, as neither gas dynamics nor magnetic fields can be ignored.

Beside the plasma beta parameter, there is another important condition on the Sun, the frozen flux condition. In a highly conductive plasma, like on the Sun, charge carriers move quickly enough to remove most electric fields very quickly, on the order of a plasma period (Priest & Forbes, 2000). This creates a condition where the magnetic field is unable to be changed through the evolution of an electric field. The magnetic field is therefore frozen to a fluid element and moves with the fluid (Priest & Forbes, 2000).

The photosphere and solar interior are regions where the plasma beta exceeds one (Gary, 2001; Schrijver & Siscoe, 2011). This high beta means the field is anchored to the fluid, and is simply dragged along with little to no effect on the fluid motion. Here, we can expect the atmosphere to behave mostly like a gaseous atmosphere – organized into stratified layers.

The chromosphere is a complex region where the plasma beta takes on values near one, and can have high and low beta regions near each other (Gary, 2001; Schrijver & Siscoe, 2011). In the chromosphere, energetic events in the magnetic field may be slowed or held in place by surrounding plasma. Conversely, bulk movement of material may be confined to one or several field lines. In either case, these motions could perturb adjacent regions.

In the corona, the plasma beta is small as the density continues to drop with height faster than the magnetic field (Gary, 2001; Schrijver & Siscoe, 2011). In this low beta environment, the frozen flux condition leads to plasma flows moving along field lines, tracing them out. This is how an active region produces such bright loops and other structures. With the plasma confined to field lines, each coronal loop can be considered isolated. This is a result of the confined plasma transferring energy and momentum along field lines far more efficiently than across them leading to very little interaction with the other loops. With transfer of heat being orders of magnitude slower across field lines than along it, each loop mainly exchanges energy and momentum with its foot points in the lower atmosphere (Rosner et al., 1978; Bradshaw et al., 2019). This leads to each loop evolving quasi-independently, though nearby loops may evolve similarly if their footpoints share similar conditions.

1.1.2 The Magnetic Canopy

In an active region, the magnetic field can be broken into a series of smaller collections of field lines, or "flux tubes" (Foukal, 1990; Priest, 2014). Each of these flux tubes is anchored to high beta regions at either end. An ideal flux tube, i.e. no fragmenting or splitting of flux along the length of the tube, contains the same flux at both foot points (Foukal, 1990; Priest, 2014). With each end containing the same flux, then as the tube moves through regions of different magnetic field strengths it will change cross-sectional area. We expect the field strength to change as it moves farther from its sources in the photosphere, or as flux tubes get squeezed together (Unverferth & Longcope, 2018). This variation in field strength is key to the formation and structure of a magnetic canopy.

Flux, for this purpose, begins at the photosphere where it is in a high plasma beta environment, meaning the gas dynamics control movement. As mentioned previously, the flux appears in discrete bundles and is moved around by the random convective motions in the photosphere. Due to this, flux that emerges from the surface into the photosphere may find the path to the low beta corona altered as these motions move it back and forth in the photosphere. Flux tubes that emerge near to or on the edge of another collection of strong flux may experience a complex connection to the corona; the presence of nearby flux may prevent the flux tube from rising vertically as it would in isolation (Gabriel, 1976).

As height increases, plasma beta drops and the magnetic field exerts more influence. As plasma beta drops the magnetic field becomes the dominant driver in plasma motions and the plasma is confined to field lines. Due to this switchover, the magnetic field transitions from the configuration the plasma forced it into, to filling space with magnetic flux. We expect this transition to happen relatively low in the atmosphere, only a few megameters off the surface, compared to the height of the flux tube, which can reach tens of megameters (Gabriel, 1976). Therefore, most of the flux tube from an active region then exists in a low beta regime. The transition from a high to low plasma beta has profound effects on the flux tube, as it changes from being confined by the plasma, to confining plasma to itself. The tube must change its area as it ascends, expanding as it reaches farther from the foot points (Zwaan, 1987). The existence of surrounding flux tubes prevent each one from expanding without limit, and results in the corona being full of magnetic field. The details of how a flux tube area changes as a function of height are discussed more in-depth in Chapter 2.

1.2 Solar Flares

A solar flare is the most energetic event in the solar system and is strong enough to have a direct impact on Earth. While observing sunspots in 1859, Carrington recorded the first observations of a solar flare (Carrington, 1859a; Schrijver & Siscoe, 2010; Benz, 2017). This event was seen as a rapid increase in brightness followed by a fast decay. Shortly after this observation, Earth experienced a large geomagnetic event with aurora occurring much farther equator-ward than normal (Schrijver & Siscoe, 2010).

A solar flare is powered by a rapid release of energy, typically stored in an active region (Zirin, 1988). This rapid release of energy leads to an extreme brightening of local plasma. The brightening is an effect of the energy release being converted into heat and compression of plasma, enhancing its radiation output (Cargill & Priest, 1982; Forbes & Malherbe, 1986; Priest, 2014). For our purposes, flares are classified according to the scale of their flux in X-rays, with A being the smallest, scaling up through B,C M, and X (Zirin, 1988). These events are a product of the large scale magnetic field and photospheric motions (Zirin, 1988). Field lines in the corona as mentioned above, are tied to specific locations on the surface. These locations move with the random motions of the photosphere, and that movement is reflected in the corona. These movements can lead to the buildup of stress in the corona, which moves the field away from the potential state, where it has the lowest energy. These motions can braid adjacent field lines, or mix them to raise the energy stored in the field (Berger & Asgari-Targhi, 2009; Yeates et al., 2014). When the stored energy is too great, some mechanism engages, and the magnetic field releases its stored energy (Sweet, 1958; Parker, 1957; Petschek, 1964; Vasyliunas, 1975). The magnetic field undergoes changes and can relax to a lower energy state. This change in the field allows for the conversion of stored magnetic energy to bulk motion, heating, and charged particle acceleration (Vasyliunas, 1975).

1.2.1 Flare Observations

The release of energy in a flare can be detected throughout the electromagnetic spectrum (Fletcher et al., 2011; Benz, 2017). Each piece of the spectrum gives us insight into different processes such as particle acceleration and the shape of the magnetic field.

The radio and hard X-ray emission are thought to share electrons as a common source, due to well correlated emission profiles (Kundu et al., 1982; Somov & Kosugi, 1997; Dabrowski & Benz, 2009). These low and high energy wavelengths are the result of various motions of an electron. The high energy hard X-rays are the result of bremsstrahlung emission and is typically seen at the foot points of flare loops and above the soft X-ray and Extreme UltraViolet (EUV) flare loop tops (Masuda et al., 2000; Emslie et al., 2003; Liu et al., 2006; Caspi et al., 2015). The loop top emission is the result of electrons colliding with nearby material, interrupting their continued acceleration (Kawabata et al., 1983; Silva et al., 1997; Masuda et al., 2000; Sui et al., 2004). At the foot points, the high energy electrons reach their stopping column in the lower reaches of the atmosphere, typically the transition region or chromosphere (Silva et al., 1997; Emslie et al., 2003; Liu et al., 2006). This contrasts lower energy X-ray and EUV emission that are the result of very hot plasma emitting thermal radiation as either continuum or spectral lines (Silva et al., 1997; Tsuneta et al., 1997; Masuda et al., 2000; Veronig et al., 2006; Caspi et al., 2015). The longer wavelength emissions, typically observed in the hundreds of MHz to GHz, are emission from the electrons as they spiral along field lines (Marsh & Hurford, 1982; Kawabata et al., 1983; Nindos et al., 2000; Melnikov et al., 2002). This emission allows for possible estimation of the plasma parameters from the emission site (Marsh & Hurford, 1982; Nindos et al., 2000). Recent observations and new observatories have allowed for high cadence and higher precision interferometric measurements, allowing for tracking the evolution of this emission during a flare (Gary, 2016; Chen et al., 2019; Karlický et al., 2020).

In the visible wavelengths, the flare is primarily seen by increased continuum emission (Hudson, 1972; McIntosh & Donnelly, 1972; Machado & Rust, 1974). The energy release in a flare transmits energy down to the lower atmosphere, and while this generally is stopped at the chromosphere, this energy can still cause impacts in the visible spectrum at or below this height (Najita & Orrall, 1970; Hudson, 1972; Machado & Rust, 1974; Lin & Hudson, 1976). The emission at the base of the flare can intensify in white light as a result of energization of the plasma directly, or secondary effects from the plasma above (Najita & Orrall, 1970; Hudson, 1972). White light emission is not a consistent attribute of flares and instead possibly depends on energy transmission to the lower atmosphere (Hudson, 1972; Hudson et al., 2006).

In the ultraviolet wavelengths the primary signatures we use are atomic emission lines (Lemen et al., 2012; Milligan, 2015). There are signatures of the energy reaching the lower levels of the atmosphere in the flare ribbons which emit in Hα and ultraviolet (Fletcher et al., 2004). The UV is a treasure trove of emission lines, especially for ionized species (Del Zanna, 2008; Fletcher et al., 2011; Lemen et al., 2012; Milligan, 2015). Coronal and flare plasma contain multiply ionized species due to their hot temperatures, leading to the UV emission (Del Zanna, 2008; Milligan, 2015). We can attempt to extract temperatures, velocities, and other physical parameters from the line emission (Brosius, 2013; Milligan, 2015).

1.2.2 Standard Model of Flares

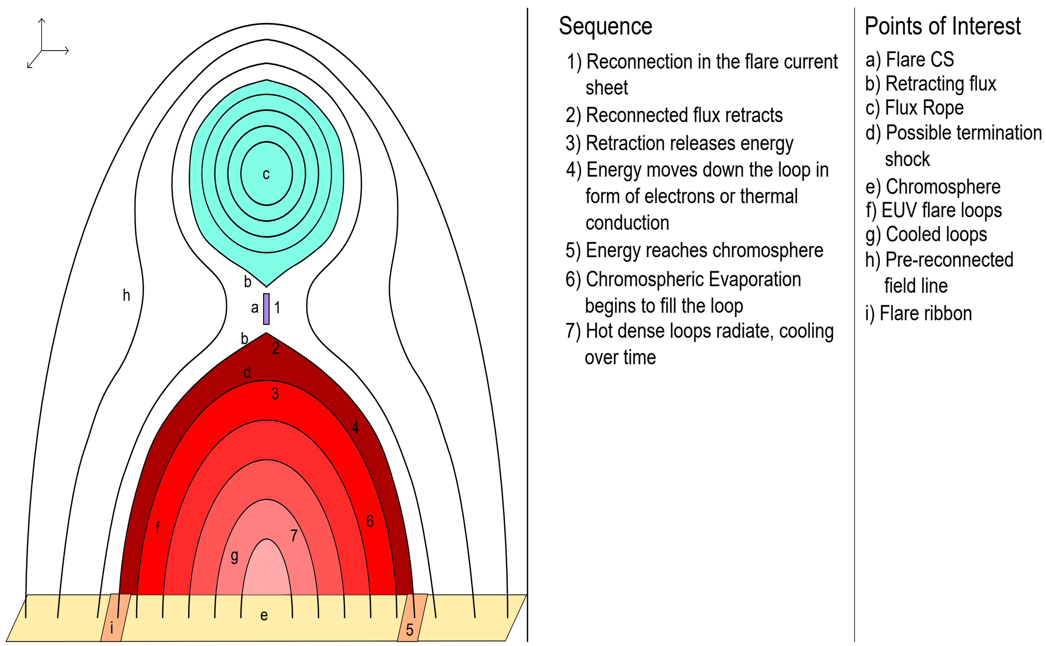

Figure 1.3: Standard model of flares. Left: Cartoon depiction of the CSHKP model (Carmichael, 1964; Sturrock, 1966; Hirayama, 1974; Kopp & Pneuman, 1976). Middle: Sequence of events, shown on the right half of the cartoon. Right: Important features of the configuration, shown on the left half of the cartoon.

Continued observations of flares, alongside significant modeling resulted in the so-called "standard model' of solar flares, or the 'CSHKP' model, named after the authors contributing to its creation (Carmichael, 1964; Sturrock, 1966; Hirayama, 1974; Kopp & Pneuman, 1976). This model is a general idea of a Coronal Mass Ejection (CME) and the flare evolution as a result of the mass ejection leaving. Specifics may vary depending on the focus of the investigation at hand, but the gross features remain the same. The model itself is more a chain of events than a mathematical structure, which lines up with its simplified nature (Carmichael, 1964; Sturrock, 1966; Hirayama, 1974; Kopp & Pneuman, 1976).

The cartoon of the CSHKP model is shown in Figure 1.3, which shows both features of note, and the general evolution of the flare. To create a flare, certain structures and conditions must be present (Forbes, 2010; Priest, 2014). One of the conditions is a magnetic field, full of excess energy, which is supplied by the active region and photospheric motion. The active region may have a twisted bundle of flux running through it, though if one is not present it may form during the CME from the reconnection of sheared field lines (Priest, 2014). The flare needs a trigger to release the built-up energy in the field. In this case, the trigger is an instability that shifts the current sheet into a flaring configuration. (Forbes, 2010; Priest, 2014).

With the proper components in place and in the right configuration, the flare is ready to begin. Beginning at 1) in Figure 1.3, the process starts with flux being moved into the current sheet, and it undergoes magnetic reconnection (Kopp & Pneuman, 1976). Originally this flux tube went from one foot point over the flux rope and down to the other side. It has now been split into two closed components. The top part of the original tube has been added to the flux rope. The bottom part now is a closed loop below the flux rope. Both parts now have excess length and can relax to shorter states. The top will now minimize its length along the flux rope. The bottom will shrink to the shortest length between the foot points allowed by the underlying flux.

Magnetic reconnection has altered the connectivity of this flux tube, and it can now release its stored energy (Magara et al., 1996). At this point the newly closed low-lying loop evolves and with an excess length, the loop begins to retract. This retraction is thought to create a population of accelerated electrons (Benz & Smith, 1987). This electron population is thought to be the emitter for the above-the-loop-top soft X-ray source (Priest, 2014). During retraction, the loop also builds up a high temperature at the apex, potentially from the accelerated electrons heating the plasma, or the shocked compression of the material in the apex (Priest, 2014).

Regardless of the mechanism, there is a pool of energy in the loop apex, and the energy streams down the loop to the chromosphere (Nagai, 1980; Cheng et al., 1983; Fisher et al., 1985). The plasma in the chromosphere is energized. The energy flux at least partially includes electrons because we see hard X-rays from the foot points (Radziszewski et al., 2011). The loop reaches its minimum length when underlying flux provides a pressure to balance against the tension seeking to minimize the tube length (Priest, 2014). The halting of retraction can lead to a source of fast mode MHD waves, or a fast mode 'termination shock' (Shen et al., 2018).

At this point, the energy released and converted in the corona has reached the chromosphere, which now must respond. Having absorbed the downward directed flux of electrons or thermal conduction front, the chromosphere is left very dense and far hotter than it was. This dense hot material naturally has a higher pressure than the material around it, and begins to expand outward to fill the connected flare loop (Antonucci et al., 1982; MacNeice et al., 1984b; Fisher et al., 1985; Antonucci & Dennis, 1983; Forbes, 2010). This expansion manifests as the twin signatures of chromospheric evaporation and condensation, which are the rise and fall of this hot material into its surroundings (Antonucci et al., 1982; Antonucci & Dennis, 1983; Fisher et al., 1985; Doschek et al., 2015). The energization of the chromosphere leaves behind a signature in EUV that exists for the length of the flare, moving outward as the flare continues known as the flare ribbon (Fletcher et al., 2004; Schrijver & Siscoe, 2010).

The flare loop becomes filled with this high pressure dense plasma, and radiates in emission lines in the megakelvin range, which we see in EUV. As evaporation ceases, there is no more energy supplied to the flare loop and radiative emission cools the plasma (Cargill et al., 1995). The pressure of the plasma drops with its temperature, and eventually the dense material cannot be supported and drains back into the chromosphere (Cargill & Bradshaw, 2013). It is difficult to describe the end point of a flare exactly in time, given that each flare loop evolves on its own, and some live longer than others. The energy release, powered by the magnetic reconnection is thought to be short lived, very short for each individual flare loop. The overall flare continues to release energy for a much longer time than any individual loop. The cooling phase can last for hours as the loops slowly cool and eventually return to a more quiescent state like they were prior to the flare (Schrijver & Siscoe, 2010).

1.3 Magnetic Reconnection

Previously we mentioned magnetic reconnection, a process that would allow for a magnetic field line to have its topology altered. Reconnection is the process by which a magnetic field line may break and connect to another field line, altering its connectivity (Parker, 1963; Priest & Forbes, 2000). This change in topology is what allows us to take the stressed field line in the standard model and break it to create two closed field lines (Parker, 1963). This process is complex and the full explanation and prediction of its behavior are not well known. This is in part due to the difficulty of gathering observations of reconnection in a current sheet (Schrijver & Siscoe, 2011). We expect a very small current sheet, or one that is much taller and wider than it is thick. Further complicating this is that modeling reconnection requires a union of very high resolutions and different length scales that are beyond our current computational abilities (Guidoni & Longcope, 2010).

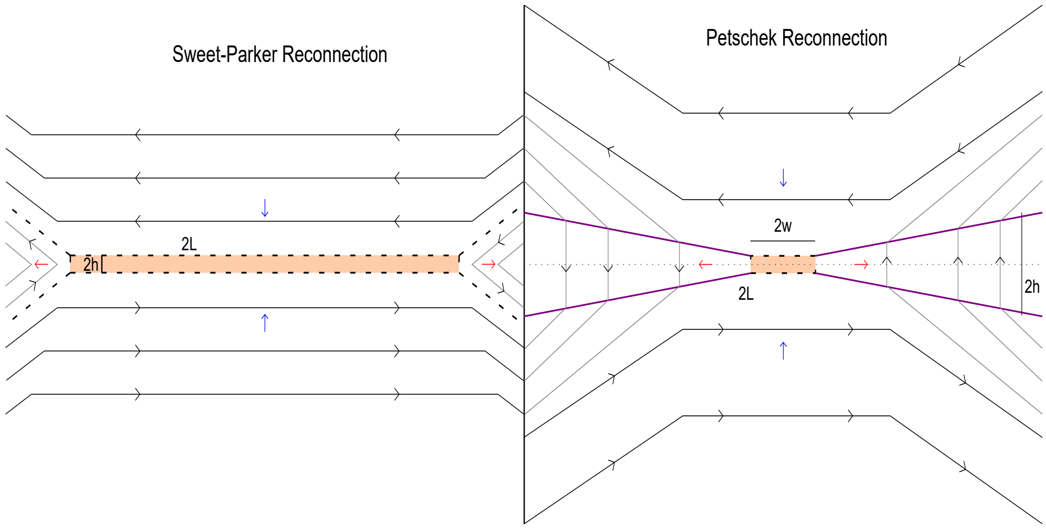

Figure 1.4: Reconnection configurations. Left: Sweet-Parker style reconnection The current sheet is long and wide with scale L, with the thickness is scaling with h, and $h << L$ (Parker, 1957; Sweet, 1958). Magnetic flux flows in from top and bottom, and after reconnection, leaves from left and right. Right: Petschek style reconnection. The current sheet is 2w wide, and the entire outflow region is 2h thick and 2L wide (Petschek, 1964). This is much smaller, and the resulting outflow is mediated by magnetohydrodynamic waves.

1.3.1 Reconnection on the Sun

Magnetic reconnection was first put forth as a mechanism for flares on the Sun by Sweet (1958) and Parker (1957). Previous work by Dungey (1953) and Cowling (1956) laid the foundation, but did not provide a mechanism. For this form of reconnection we require a small region where the field flips 180 degrees. This discontinuity in the magnetic field creates a thin sheet filled with an electric current (Parker, 1957). This current sheet forms here from the magnetic field, pointing rightward on one side and leftward on the other. Inside the current sheet, an electric field is formed, despite the high conductivity of the plasma. This new electric field allows for the plasma to break the field lines and reattach them with new connectivity (Sweet, 1958). Once a field line is reconnected it is swept out from the sheet (Sweet, 1958). Plasma leaving the sheet serves to drag new magnetic field into the sheet which then undergoes reconnection. This is a steady-state process that can be computed from the inflow rate, the length of the sheet, and its thickness (Parker, 1963). The configuration of this current sheet and flows is depicted in the left panel of Figure 1.4.

Sweet and Parker style reconnection has been simulated and works as a steady state reconnection scenario; however, it is too slow to match observations of a flare (Parker, 1973; Forbes et al., 2018). The issue is that this reconnection mechanism works through diffusion, and in the corona that is far too slow (Petschek, 1964). With Sweet-Parker reconnection the time scale for a flare is on the order of 2 to 3 orders of magnitude too large (Petschek, 1964). This type of current sheet is also susceptible to instabilities that may tear it apart too soon for reconnection to even occur at a meaningful level (Landi et al., 2015).

With the realization that Sweet and Parker is too slow, a new model proposed by Petschek (1964) altered the geometry and attained higher reconnection rates. A cartoon of this altered geometry is in the right panel of Figure 1.4. If we consider that waves may play a role in reconnection, we can make a more compact region (Petschek, 1964). With the reconnection region bounded by these standing waves, it is now possible to accommodate reconnection at multiple rates. Replacing the flat elongated current sheet with the more compact sheet accelerates the process. Instead of simply allowing diffusion to transport energy, this process utilizes magnetohydrodynamic (MHD) waves, specifically the Alfvén wave, to move energy out of the region (Petschek & Thorne, 1967). Reconnection still takes place at an X-point in the middle of the sheet, but the region of the sheet is much smaller, 2a instead of 2L as seen in Figure 1.4. Instead of a consistent width current sheet, we have a bounded region that increases with some angle away from the reconnection site (Petschek, 1964).

Petschek reconnection not only introduces a faster mode, it introduces fluid behaviors beyond simple flow (Petschek & Thorne, 1967). With this solution being a steady-state system, and the introduction of waves to the system, it's only natural that we divide regions with standing waves (Petschek, 1964). In this case it's possible for the standing waves to be a combination of a slow magneto-sonic shock and either an intermediate wave or shock (Petschek & Thorne, 1967). These are standing in the frame of the reconnection region; in the frame of the retracting flux they move outward from the apex of the loop.

While Petschek reconnection is able to sustain the rates needed to match observations, it has problems of its own. External driving of the Petschek solution can lead to flux pileup, or a breakdown of the current sheet (Priest & Forbes, 1986; Litvinenko et al., 1996). Another classification of reconnection scenario is like those of Syrovatskiǐ (1971); Green (1965). These do not involve an X point, instead creating an extended current sheet between two bounding Y points (Syrovatskiǐ, 1971; Green, 1965; Longcope & Forbes, 2014).

More recent works than Petschek, Green, and Syrovatskii consider instabilities leading to patchy or pulsed reconnection (Biernat et al., 1987; Linton et al., 2009). These include tearing mode instabilities creating plasmoids, leading to the creation of many small-scale current sheets to facilitate faster reconnection (Priest & Forbes, 2000; Landi et al., 2015). As a result, while we have come a significant way to understanding reconnection as it powers a flare, there is much left to understand. For example, flare loops tend appear in discrete bundles despite neighboring foot points and some invoke patchy or bursty reconnection as the difference in between these loops (Linton & Longcope, 2006).

1.4 The Thin Flux Tube Model

The thin flux tube (TFT) model was originally used to describe motion of a flux bundle in the convection zone by Spruit (1981a,b). This model is not for an arbitrary collection of flux, but instead one that is thin compared to its length. It is a one-dimensional model where everything is parameterized along the length of the tube (Spruit, 1981b). These equations describe the behavior of an isolated tube in a background of plasma. Spruit used this model to consider the propagation of wave energy from below the solar surface into the chromosphere (Spruit, 1981b).

Later this model was converted for use in flare loop modeling by Linton & Longcope (2006). This version of the thin flux tube model considers the flux tube just after reconnection which enables it to use the simpler fluid equations without having the more complex reconnection physics (Longcope et al., 2009). These tubes have been used to model the effects of Petschek type reconnection in a retracting tube allowing for an analysis of these effects without needing a full three-dimensional magnetohydrodynamic simulation (Longcope et al., 2009; Guidoni & Longcope, 2010; Longcope & Klimchuk, 2015). Using the collection of these flux tubes with a magnetic reconnection rate, these tubes can be used to create synthetic flares or individual flare loops (Longcope et al., 2016). This allows for the comparison of various physical scenarios to observations, in an attempt to understand the dynamics of flare loops in a solar flare.

As with any model, the thin flux tube starts with the equations for the system. In each Chapter to follow, an in-depth explanation of the equations used is given, as such the explanation here will be brief. One-dimensional hydrodynamics begins with 3 equations, each based on a conserved quantity: mass, momentum, and energy. Adding in magnetic fields to the fluid equations would require further equations. We are spared from having to do that, given that the thin flux tube model follows a bundle constant flux background that does not change in time, and can not exchange energy with the flux tube (Linton & Longcope, 2006).

The continuity equation is the equation governing the conservation of mass (Guidoni & Longcope, 2011). Without sources and sinks, it relates the density and velocity to ensure that no mass is created or lost. The momentum equation shows how the fluid moves through space given the forces acting on it (Longcope & Klimchuk, 2015). Typically, this includes gas pressure, viscosity, gravity, magnetic tension and pressure. For certain sections of parameter space, and under specific conditions, some terms may be small and not used. The energy equation tracks the flow of the energy in the fluid (Longcope & Klimchuk, 2015). This equation can be cast in terms of internal energy, pressure, or temperature. The primary effects here include heating due to compression or expansion, viscous heating, radiation, thermal conduction, and any ad hoc heating applied to the tube.

The equations are simplified and given extra conditions through assumptions (Spruit, 1981b). The first is that the flux tube under consideration is isolated from the background (Longcope et al., 2009). This means that there is no mass or energy exchange between the ambient conditions and the tube. The background is also static, with no variation in time (Longcope et al., 2009). The tube can move through the background, and as it can vary in space, over time the tube may encounter different conditions. The equations guiding the evolution are all parameterized along the length of the tube, with no azimuthal or radial effects (Longcope et al., 2009). Given the isolation of the flux tube from the background, there is no need for the induction equation, as no change in the magnetic background is allowed and the tube matches that field. Finally, flux is conserved along the tube.

These assumptions lead to this thin flux tube model being an embedded three-dimensional MHD model (Linton & Longcope, 2006; Guidoni & Longcope, 2011). The tube can be modeled in three dimensions given the use of a three-dimensional background. Any motion of the tube can take place in the full three-dimensional space available. At the same time, any motion can be broken down into two components with respect to the tube: motions along the tube and motions perpendicular to it. The benefit of this is that this model produces more realistic results than a similar one-dimensional model, without the complexity and time consumption of a full three-dimensional MHD model (Longcope & Klimchuk, 2015).

1.5 Motivation and Layout

Despite the known portions of the topics mentioned previously, there are still unclear aspects to all the phenomena mentioned. Energy release in the corona is still an open question. The probable answer is magnetic reconnection, but the models being used do not account for all the observed features. If the reconnection takes place along an extended sheet and relaxes the field to a lower energy state, why does the flare not look smooth and more continuous along the extent of the arcade? If the current models of reconnection are what is occurring in a flare current sheet, where is the material leaving the current sheet at the Alfvén speed? There is no current consensus on the structure of the flare current sheet, a factor that is expected to impact the flare evolution.

Chapter 2 addresses the overall structure of a flare. Why is it that some reconnected flux becomes filled with hot emitting plasma, while adjacent flux does not fill with material? The reconnection models indicate that reconnected flux should transmit energy down and into denser cooler material (Neupert, 1968; Antonucci et al., 1982; Fisher et al., 1985). This material undergoes evaporation to fill the loops but appears not to do so evenly. This points to some other factor aside from the reconnection. We know that the flux passes through the magnetic canopy (Gabriel, 1976). The canopy is tied to the flux emergence in the photosphere and varies over the length of the arcade. This work considers the intersection of two models that have not interacted before, leading to a more complete picture of evaporation during a flare. Specifically this project investigated whether the geometry of the magnetic canopy could impede or enhance flows resulting from evaporation.

In Chapters 3 and 4, we employ the thin flux tube model. The thin flux tube model has not seen widespread use, despite its advantages for flare modeling. The model has been shown to reproduce Petschek type results (Linton & Longcope, 2006; Longcope et al., 2009), and has the advantages of providing results more in line with full three-dimensional MHD simulations. It does this at the cost of interactions with the rest of the domain assumed to be static. It shows promise as an intermediate, to explore effects before turning to a full three-dimensional simulation where the size and resolution requires large amounts of resources. The work here also serves to enlarge the body of TFT work and prove its utility in coronal modeling.

Chapter 3 investigates how the current sheet structure impacts the evolution of reconnected flux tubes. The current understanding of solar flares calls for magnetic reconnection as the energy releasing method for a flare. Triggering magnetic reconnection allows the stored magnetic energy to be converted into other forms. Due to the difficulty of robust magnetic field measurements in the corona, the magnetic field structure along flare structures is not well constrained. This leads to a gap in our understanding, with different models taking different approaches. Some use a uniform magnetic field along the current sheet, while others assume that the reconnection occurs at the strongest magnetic field (Levine, 1974; Vasyliunas, 1975; Somov & Kosugi, 1997; Forbes et al., 2018). The result is a variety of approaches that yield no consensus on this issue. The work in chapter 3 takes the TFT model and tests if there are observable consequences from the magnetic field structure along a current sheet.

Chapter 4 explores a potential explanation for the lack of Alfvénic outflow observed in flare current sheets. Reconnection models consistently place the outflow of reconnected flux as moving at the Alfvén velocity (Parker, 1957; Sweet, 1958; Petschek, 1964). This is true for Sweet-Parker to Petschek to more recent bursty or patchy reconnection models. Observations of downward moving features such as SADs and SADLs show them moving at several hundred kilometers per second (McKenzie & Hudson, 1999; Savage & McKenzie, 2011). Some attribute these downward moving features to reconnected flux in the current sheet retracting. For these features to be reconnection outflow, there needs to be a reconciliation with the proposed Alfvénic outflows. In the current sheet there must be some interaction that slows them from Alfvénic speeds to the speeds observed. We expect that the interaction between retracting flux and the current sheet may take the form of some sort of drag, motivating this study. Complicating things is the need to still retain some Alfvénic signatures, such as the fast-moving microwave emission reported by Yu et al. (2020).

CHAPTER TWO

EFFECTS OF THE CANOPY AND FLUX TUBE ANCHORING ON EVAPORATION FLOW OF A SOLAR FLARE

Contribution of Authors and Co-Authors

Manuscript in Chapter 2

Author: John Unverferth

Contributions: Developed study and framework for analysis of the problem. Wrote manuscript save for "The Canopy and Magnetic Chambers."

Co–Author: Dana Longcope

Contributions: Helped to guide study. Wrote "The Canopy and Magnetic Chambers" section of manuscript. Gave feedback of methods, analysis and commented on drafts of the manuscript.

Manuscript Information

John Unverferth and Dana Longcope

The Astrophysical Journal

Status of Manuscript:
____ Prepared for submission to a peer-reviewed journal
____ Officially submitted to a peer-reviewed journal
____ Accepted by a peer-reviewed journal
__X__ Published in a peer-reviewed journal

American Astronomical Society
June, 2018, ApJ 859, 170
10.3847/1538-4357/aac106

ABSTRACT

Spectroscopic observations of flare ribbons typically show chromospheric evaporation flows which are subsonic for their high temperatures. This contrasts with many numerical simulations where evaporation is typically supersonic. These simulations typically assume flow along a flux tube with uniform cross-sectional area. A simple model of the magnetic canopy, however, includes many regions of low magnetic field strength, where flux tubes achieve local maxima in their cross-sectional area. These are analgous to a chamber in a flow tube. We find that one third of all field lines in a model have some form of chamber through which evaporation flow must pass. Using a one dimensional isothermal hydrodynamic code we simulated supersonic flow through an assortment of chambers, and found that a subset of solutions exhibit a stationary standing shock within the chamber. These shocked solutions have slower and denser upflows, than would a flow through a uniform tube. We use our solution to construct synthetic spectral lines and find the shocked solutions show higher emission and lower Doppler shifts. When these synthetic lines are combined into an ensemble representing a single canopy cell, the composite line appears slower, even subsonic, than expected due to the outsized contribution from shocked solutions.

2.1 Introduction

Chromospheric evaporation is the response to a sudden energy deposition in the relatively cold and dense plasma of the chromosphere. As energy is deposited from above, it heats the chromospheric plasma, which then expands upwards along field lines. This fills the post flare loops with dense, multi-megakelvin plasma, which appears brightly in Extreme Ultraviolet (EUV) and soft x-ray (SXR). First proposed in 1968, it was thought to be the cause of the delay between microwave and soft X-ray emission (Neupert, 1968). This was later observed by the Bent Crystal Spectrometer (BCS) aboard the Solar Maximum Mission (SMM) by Doppler shifts in Calcium XIX (Antonucci & Dennis, 1983). Since its initial observation, evaporation has been observed in SXR, EUV, and ultraviolet by subsequent observations.

Early observations consistently found evaporation flows to be subsonic. For example the Ca XIX spectral lines observed by BCS on SMM showed upflow velocities of 310 km/s (Antonucci & Dennis, 1983). Observations from Yohkoh's Bragg Crystal Spectrometer show upflows below 100 km/s (Brosius & Phillips, 2004) in Fe XIX, Ca XIX, and S XV. All have comparable peak formation temperatures ($T \simeq 10^7$K) at which the sound speed in fully ionized coronal plasma, $c_s \simeq 500$ km/s, is significantly above observed upflow speeds. More recently, observations from the Coronal Diagnostic Spectrometer (CDS) aboard the Solar and Heliospheric Observartory (SoHO) have Fe XIX with a similar velocity of 100 km/s (Brosius, 2009). The Extreme-Ultraviolet Imaging Spectrometer (EIS) captures a wide range of the ionization states of iron, and observations of a flare show velocities ranging from 22 km/s (Fe XIV) to 268 km/s (Fe XXIV) (Milligan & Dennis, 2009). Finally, observations from the Interface Region Imaging Spectrograph (IRIS) shows that Fe XXI can have upflow velocities up to 300 km/s during evaporation (Graham & Cauzzi, 2015). All of these flows are subsonic at the temperature of formation for the ionization state observed. Early observations of chromospheric evaporation used whole disk observations, which were analyzed using a two-component fit: a stationary plasma and a blue shoulder (Antonucci & Dennis, 1983).

Chromospheric evaporation observations have been understood using one-dimensional models (Nagai, 1980; Peres et al., 1982; Cheng et al., 1983; MacNeice et al., 1984a; Fisher et al., 1985), however, these often find supersonic evaporation instead of the subsonic flows actually observed. Sudden energy deposition can enhance the chromospheric pressure by a factor well over ten, resulting in the same kind of supersonic expansion one would expect into a vacuum. Fisher *et al.* argued that upflow speeds could reach 2.35 times the local sound speed (Fisher et al., 1984). This was refined the following year to an upper bound of 2.6 on the upflow Mach number (Fisher et al., 1985).

The same work introduced the distinction between gentle and explosive evaporation. In gentle evaporation the energy deposition is balanced locally by enhanced radiative loss so large pressure enhancements do not occur. The result is subsonic evaporative flow and little downflow beneath it. Explosive evaporation, on the other hand, occurs when the local radiative losses are unable to offset the deposition and significant pressure enhancement does occur. This drives supersonic flow, as mentioned above, accompanied by downward recoil known as *chromospheric condensation*. Peres & Reale (1993) later showed that the upflow velocity depends on the downward energy flux and can be either subsonic or supersonic. A recent study by Longcope (2014) considered energy deposition by thermal conduction, which always drives explosive evaporation. That study showed analytically that the resulting supersonic evaporation velocity scaled with the one-third power of the downward flux driving it.

The modeling efforts cited above use flux tubes with uniform cross sectional area, as does the majority of one-dimensional flare modeling done before and after (Nagai, 1980; Peres et al., 1982; Cheng et al., 1983; MacNeice et al., 1984a; Bradshaw et al., 2004). A notable exception is Emslie et al. (1992) who studied the effect that a loop with tapered legs would have on both particle precipitation and chromospheric evaporation. They found that the tapered flux tube produces faster upflows than would a straight tube, because the supersonic upflow was driven through a diverging nozzle. Emslie et al. (1992) conclude that since it leads to larger, rather than smaller, theoretical upflows, loop tapering alone cannot resolve the discrepancy with observation.

Emslie et al. (1992) considered loops whose cross sectional areas increase monotonically, by up to a factor of 100, from footpoint to apex. (To simplify the electron transport calculation they assumed the area to be exponentially related to the electron column.) The overall expansion is necessary to connect the $\sim$ 10 G coronal field to the $\sim$ 1000 G photospheric flux concentrations which anchor it. In many models most of this expansion occurs in a low-lying canopy in which the photospherically concentrated flux expands to form the volume-filling corona (Gabriel, 1976). In such models, however, not all flux tubes expand monotonically. For instance, the oft-reproduced Figure 5 from Gabriel (1976) shows field lines emerging from the center of a concentration weakening monotonically upward, while others emerging from the edges weaken first and then *strengthen* to attain their coronal value. Flux tubes composed of the latter field will present to the supersonic upflow a diverging nozzle followed by a constriction. The flow will thus be driven through a kind of *magnetic chamber*, and may behave differently from the flows studied by

Emslie et al. (1992).

The present work considers the effect on evaporative upflow of flux tubes with this chamber geometry. From a three-dimensional analog of the canopy model used by Gabriel (1976), we find that approximately one third of all flux tubes include a chamber, and in roughly one-sixth of those the cross sectional area reduces by a factor of two or more following its maximum expansion. Supersonic flows driven into such chambers can form stationary shocks within them, behind which the flow will be subsonic and far denser. Owing to its higher density, and thus greater emission, shocked material in even a fraction of the flux will contribute disproportionately to the observed spectral line profile. We show in this work that this effect may help to explain the preponderance of subsonic flows observed in flare evaporation.

The study is presented as follows. In the next section we describe our three-dimensional canopy model and characterize the magnetic chambers found in it. The next section describes the basic properties of steady flow through general chambers. These are analogous to the more familiar case of flow through a nozzle (de Laval's nozzle), but differ in several surprising ways. We conclude that steady flow solutions through a chamber are best found through time-dependent calculation. Section 4 introduces our method of computing time-dependent solutions (i.e. our numerical code), and describes the solutions we obtain. In section 5 these flow solutions are used to synthesize spectral line profiles. We synthesize composite profiles which include chambers of various configurations, along with monotonically expanding tubes, in proportions found from the model canopy of section 2. This demonstrates, as mentioned above, that the subsonic, post-shock material in the fraction of tubes with magnetic chambers, contribute disproportionately to the line profile.

2.2 The Canopy and Magnetic Chambers

The coronal magnetic field whose reconnection is responsible for a flare is typically anchored to the solar surface in a region of plage, which is generally unipolar. While the average magnetic field strength within plage is of order 100–300 G, it is known to consist of numerous smaller flux elements whose field strength is 3–10 times stronger (Stenflo, 1973). These small elements, lying within the intergranular lanes, provide concentrated anchor points for the volume-filling coronal field, as depicted by an idealized model shown in Fig. 2.1. That shows the layer, known as the magnetic canopy, in which the magnetic field expands from its concentrated sources to fill the corona.

Numerous models have been developed to account for the effect of canopy geometry on a variety of solar phenomena. Ours resembles the most well-known of these, that of Gabriel (1976), in that it is a potential field extrapolated from small sources distributed across a photospheric plane. Unlike that two-dimensional model, our sources are distributed in a hexagonal lattice across the plane (see left panel of Fig. 2.1). As a result, each source connects to a triangular cell of coronal flux above it. The edges between cells are formed by the fan surfaces (dashed blue curves) from prone positive null points (circles) on the photospheric surface [see *eg.* Longcope (2005) for a description of these topological features]. These edges join to one another along vertices formed by vertical spine lines originating from upright negative null points (green triangles). One example of such a line is shown in the elevation view (lower right) as a solid blue line connecting to the green triangle.

The canopy's cellular structure is manifest in the variation it creates in magnetic field strength, evident in the magenta contours on the left of Fig. 2.1. The field strength at a given height, $|B(x, y, z_s)|$, is locally maximum above a source (yellow

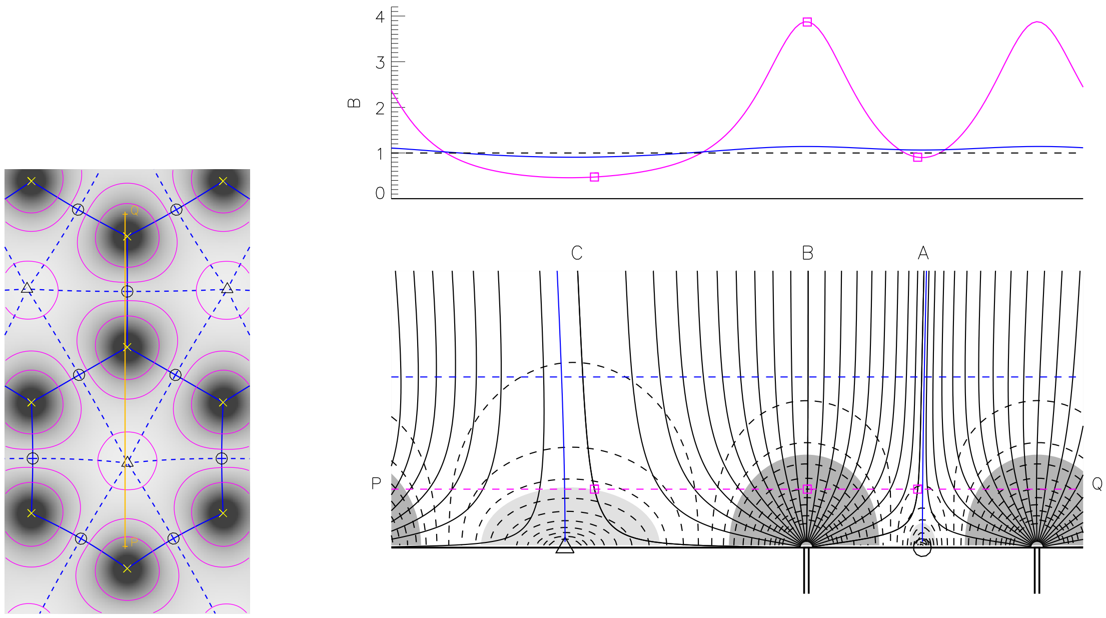

Figure 2.1: An idealized model of a three-dimensional magnetic canopy. The left is a top view showing the flux elements, marked with yellow $\times$s arranged in a hexagonal lattice. Magnetic field strength at height z_s is indicated both as inverse gray-scale and with magenta contours. Blue solid and dashed lines show magnetic spines and fan-traces originating from photospheric prone and upright null points, denoted by black circles and triangles respectively. An orange vertical line, terminating at points P and Q, shows the location at which the field is sliced to produce the elevation view shown in the lower right. In that view the horizontal magenta line shows the sampling height z_s. Black dashed contours show the magnetic field strength in this slice, with dark gray and light gray emphasizing regions of high and low strength respectively. Black solid curves are magnetic field lines, and three particular lines are called out in bold and labeled A, B and C. Two null points lying along the slice are shown by the triangle and circle, and blue lines originating at them are the spine (left) and fan (right) from them. The field strength along the horizontal magenta line, and the higher blue line, are plotted in the top right, normalized to the asymptotic coronal strength (black dashed line). Magenta boxes show the locations that field lines A, B and C cross the sampling height $z = z_s$.

$\times$), lying at the cell's center. It has a local minimum above each upright null point (triangles), which form the cell vertices. There is a saddle above each prone null (circles), which lie at the mid-point of each cell edge. This field-strength variation is strongest at low altitudes, as seen by comparing the magenta and blue curves in the upper right panel of Fig. 2.1. At heights significantly greater than the source spacing (i.e. a granule) the field strength is roughly uniform, assuming the average value for that plage region (dashed black curve).

This magnetic field variation will have significant effects on the upward flow of plasma driven as chromospheric evaporation by the flare. In quiescent conditions the transition region (TR) will probably form a corrugated surface through the canopy (Gabriel, 1976). The strong downward energy flux of the flare will, however, drive the TR down into the vicinity of the magnetic source (Fisher et al., 1985). The evaporation will therefore originate in strong field and flow upward along its field line into the weaker region above. Models of chromospheric evaporation predict supersonic flows with iso-thermal Mach numbers in the range $M = 2$–3 (Fisher et al., 1984; Longcope, 2014). Flow through a tube of magnetic flux Φ will have a cross sectional area $A = \Phi/B$, which expands as the field weakens going upward. Flow through a flux tube near the center of a magnetic cell, such as B in Fig. 2.1, will follow a tube with monotonically increasing cross sectional area. The lower left panel of Fig. 2.2 shows, in green, the area of that flux tube as a function of arc length, $A(\ell)$, scaled to the asymptotic area. That green curve shows area increasing monotonically, approaching the asymptote ($A = 1$) from below. Encountering such an expanding area, the supersonic flow will naturally accelerate.

The situation is more interesting for those field lines away from the cell center, such as A or C in Figs. 2.1 and 2.2. As such a field line approaches the cell's periphery, its field strength first decreases, as it approaches a null point, but then increases again

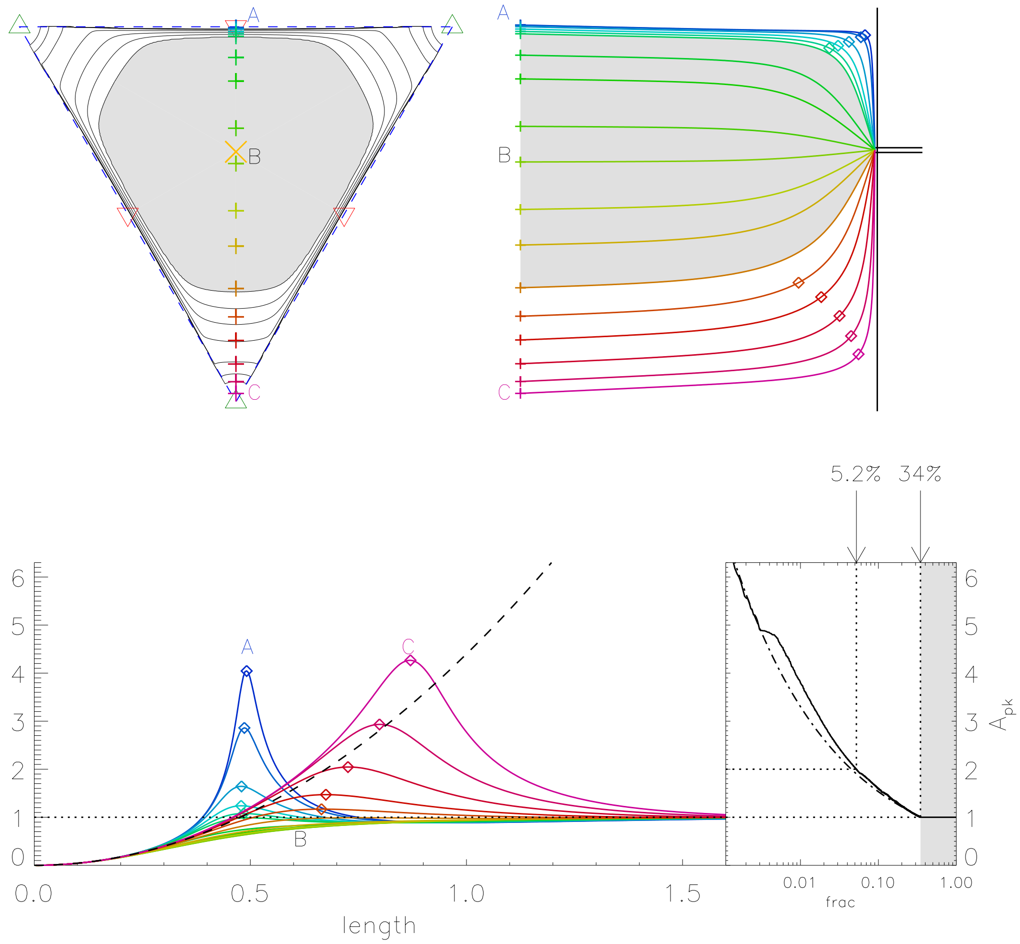

Figure 2.2: The flux tube areas and chamber expansion factors. The upper right panel shows field lines from a single cell in side view, as in Fig. 2.1 except on its side and with color-coded field lines. The local maximum in a flux tube's area (minimum field strength) is indicated by a diamond. Field lines which expand monotonically are found inside the shaded region. The upper left panel shows a top view of the triangular cell, matching the view from Fig. 2.1. The tops of the color-coded field lines are shown with +s. Photospheric null points are shown with red and green triangles as in Fig. 2.1. The central shaded region includes all monotonically expanding field lines. Contours outside this are regions where peak expansion is $A_{\rm pk} = 1.1$, 1.25, 1.5, 2, and 3 (moving outward). The lower left panel shows $A(\ell)$ for each colored field line, with the source at $\ell = 0$. Points of maximum area are once again indicated with diamonds. The dashed curve shows monopolar expansion, $A(\ell) \sim \ell^2$, for reference. The lower right panel shows the fraction of the cell's flux in which $A_{\rm pk}$ exceeds a given value (solid curve). The grey shaded region is the fraction of monotonically expanding flux tubes (66%). The dash-dot curve is the analytical result for the upright null alone: $0.36\,A^{-3}$.

as it moves upward away from the null. This is evident in the lower left of Fig. 2.2 as a local maximum (marked with a diamond) in $A(\ell)$ in curves shown in blue (like A) and red (like C). These cross the asymptotic value and then approach the asymptote from above. The cell edge thus create a kind of "chamber" through which the evaporation flow must pass. Given that the size of these cells is approximately that of a granule, the chambers can be expected to be some small fraction of a granule. Supersonic flow though this kind of flux tube will encounter an expansion followed by a constriction. Encountering this constriction can cause the flow to shock, resulting in subsonic evaporation flow, consistent with observation but rarely predicted in models.

Magnetic chambers are not rare: they account for roughly one-third of the flux tubes in our model. The upper left panel of Fig. 2.2 shows the spatial distribution of expansion factors. It shows a top view of the triangular cell, the nulls (triangles) at its vertices, and separatrices (fan surfaces, blue dashed lines) at its edges. The central grey shaded region encompasses all monotonically expanding field lines – flux tubes with no magnetic chamber. Contours outside it show those field lines whose peak expansion is $A_{\rm pk} = 1.1$, 1.25, 1.5, 2, and 3 (moving outward). Larger expansion factors are confined more closely to the cell's periphery. Those close to the corners, like line C, reach maximum expansion around $\ell \simeq 1$, while those at the edge, like A, reach it at $\ell \simeq 0.5$. Finally, the cumulative distribution function (lower right of Fig. 2.2) shows the fraction of area outside of any contour. It shows that one-third of the flux tubes (i.e. 34% of the flux) have some chamber, and about one-sixth of those (i.e. 5.2% of all flux) expand to more than twice their asymptotic area, before constricting on the way out.

The reconnection powering a solar flare is believed to occur high enough in the corona that it will probably not be affected by the canopy or its cellular structure. We therefore expect it to drive evaporation in field lines of all kind, regardless of their geometry. About a third of the evaporation flow will therefore be driven through a magnetic chamber. It is therefore important to understand what effect this geometry will have on supersonic evaporation flow. If it creates a standing shock, then we will expect subsonic flow in that tube. The slower flow will have higher mass density and thus higher emission measure, given the same mass flux. In this case we would expect the subsonic flow to have a disproportionate effect on observations of evaporation.

2.3 One-Dimensional Flows

Flare energy is transported from high in the corona to the chromosphere where it drives evaporative upflows. We assume the flow emerges from the region of highest density, initially the chromosphere, at a supersonic velocity. We also assume the properties of this driven flow vary slowly compared to the sound transit time across the canopy layer. The flow through the canopy will therefore be approximately steady. It will be a steady flow though a tube of spatially-varying cross-sectional area, $A(x)$.

2.3.1 Bernoulli's Equation and Streamlines in Flows of Changing Areas

Unsteady flow through a fixed tube will satisfy the one-dimensional momentum equation

$$\frac{\partial u}{\partial t} = -u\frac{\partial u}{\partial x} - \frac{1}{\rho}\frac{\partial P}{\partial x} + \frac{4}{3}\frac{\mu}{\rho A}\frac{\partial}{\partial x}\left(A\frac{\partial u}{\partial x}\right), \tag{2.1}$$

where $u(x)$ is the flow velocity (taken to be positive) P is pressure, ρ is mass density, and μ is the dynamic viscosity, here taken as a constant.

Evaporative flow occurs at very high temperature in which thermal conductivity is extremely effective. Accordingly we take the flow within the canopy layer to be isothermal $P = c_s^2\rho$, where c_s is the isothermal sound speed. Mass continuity in steady state demands that $\rho u A = \dot{m}$ be constant. Introducing this into the momentum equation, Equation (2.1), and taking $\partial u/\partial t = 0$ yields

$$\frac{\partial}{\partial x}\left[\frac{1}{2}u^2 + c_s^2\ln(\rho) - \frac{4}{3}\frac{\mu}{\rho A}\frac{\partial u}{\partial x}\right] = -\frac{4}{3}\frac{A\mu}{\rho u}\left(\frac{\partial u}{\partial x}\right)^2 \quad . \tag{2.2}$$

The left hand side of this equation is the derivative of a quantity, in square brackets, which would be conserved if the flow were inviscid. In the presence of viscosity the right hand, strictly negative, causes this otherwise conserved quantity to decrease moving downstream.

In the inviscid case, $\mu = 0$, Eq (2.2) demands that

$$\frac{1}{2}u(x)^2 + c_s^2\ln\Big[\,\rho(x)\,\Big] = \frac{1}{2}u(x)^2 - c_s^2\ln\Big[\,u(x)\,\Big] - c_s^2\ln\Big[\,A(x)\,\Big] + c_s^2\ln(\dot{m}) = \mathcal{C} \tag{2.3}$$

be a constant, denoted $\mathcal{C}$. This is the standard form of Bernoulli's equation for an isothermal fluid. Dividing this by the constant c_s^2 gives a dimensionless equation

$$\frac{1}{2}M(x)^2 - \ln\Big[\,M(x)\,\Big] - \ln\Big[\,A(x)\,\Big] = \mathcal{C}_3. \tag{2.4}$$

where $M = u/c_s$ is the Mach number, and $\mathcal{C}_3$ is a different constant, related to $\mathcal{C}$.

Contour plots in (x, M) phase space, of the left hand expression in Equation (2.4), show how variation in cross-sectional area creates a variation in flow. Two such contour plots are shown in Figure 2.3. The left panel shows the familiar case of de Laval's nozzle (Landau & Lifshitz, 1959, for example). The function has a saddle point at the nozzle's throat, where $A(x)$ is minimum ($x = 5$ Mm). This creates a critical contour at $\mathcal{C}_3 = 1/2 - \ln(A_{\min})$, with an X-point, separating the phase space into three regions. In the first region (1), shaded dark gray, the flow remains always subsonic, speeding up to pass through the throat. In the second region (2), shown in light gray, the flow remains supersonic, slowing down at the throat. In the third region, the contours double over themselves and thus provide no valid steady state solution; it is physically forbidden. Separating the first two regions from the third are two critical contours which represent the only smooth transitions from subsonic to supersonic flow right at the throat of the nozzle.

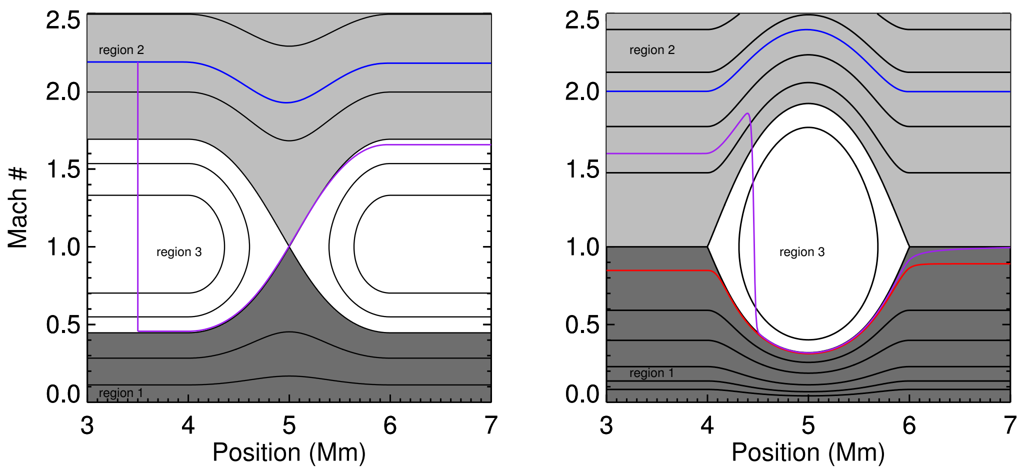

Figure 2.3: Steady flows through a nozzle(left) and chamber (right). Left: The contours for de Laval's nozzle, the gray contours are the critical solution where the flow transitions from subsonic to supersonic, or vice versa. Right: The contours for a chamber. The blue and purple lines over-plotted onto the nozzle contours represent two solutions with the same boundary conditions.

The right panel of Figure 2.3 shows how a steady flow passes through a chamber whose area expands to maximum at $x = 5$ and then narrows back down. As with the nozzle there are three regions separated by a critical contour. There are still the smooth subsonic (1) and supersonic (2) sections of phase space. In the chamber however, the subsonic and supersonic sections behave opposite to their counterparts in the nozzle. The subsonic flow slows when it enters the chamber and speeds up upon leaving. The supersonic region has the flow increase speed as it enters the chamber and then must slow to exit. The forbidden section (3) lies in the chamber itself and is closed on either end by the critical contour. In both the nozzle and the chamber, the forbidden contours have a lower value of $\mathcal{C}_3$ than the contours that represent smooth steady state solutions.

The two cases in Figure 2.3 show different responses to upstream boundary conditions. Defining flow parameters far upstream has the effect of choosing a contour at the left boundary of the plot. The full contour then yields the flow through the entire domain. Had one chosen a contour from within the forbidden region of the nozzle (left panel), say $M(0) = 1.5$, there could be no global solution. Instead the flow develops a shock somewhere to the left of the throat, and jumps onto a contour in the subsonic region, or possibly exactly onto the critical contour. The shock then propagates to the left, as explained below, until it reaches the left boundary where it effectively resets the upstream boundary condition to some value with a physical solution. Which solution is chosen will depend on the time-dependent behavior of the shock which develops.

In the case of the chamber (right panel) this kind of crisis, and boundary condition resetting, need not occur. All contours in the forbidden region are closed and thus cannot be accessed from the left boundary. A smooth global solution is therefore always possible, at least for the inviscid case we have heretofore considered.

The situation becomes very different once viscosity is included. Viscosity is an essential element in the consideration of shocks, and therefore cannot be completely neglected. Including a non-zero viscosity in Equation (2.2) introduces two new terms. The last term inside the square brackets, $(3\mu/4\rho A)(\partial u/\partial x)$, effectively changes the value of $\mathcal{C}_3$ that the flow will follow. Had the entire term continued to be a constant, then $\mathcal{C}_3$ would increase where the flow sped up ($\partial u/\partial x > 0$) and decrease where it slowed down. Far to the left and right of any chamber the flow speed would presumably become uniform and $\mathcal{C}_3$ would assume its previous role as a conserved quantity.

The term on the right hand side of Equation (2.2) will systematically decrease the value of the quantity in brackets. The effect of this dissipation is to force the flow onto a contour with a lower value of $\mathcal{C}_3$ wherever the flow speed changes. Any shock will produce a very large deceleration ($\partial u/\partial x < 0$) and therefore a significant drop in the value of $\mathcal{C}_3$ in a single jump. With this in mind it is notable that for both cases shown on Figure 2.3 the critical contour has the lowest value of $\mathcal{C}_3$ among allowed flows; all forbidden flows have values lower than this.

2.3.2 Shocks and the Rankine-Hugoniot Conditions

The traditional analysis of shock flows are performed in a reference frame moving with the shock, making the shock itself appear stationary. The solution upstream and downstream of the shock will be uniform, and characterized by values with subscript 1 (upstream) or 2 (downstream). The traditional analysis also assumes the cross-sectional area to be uniform throughout the shock. The conservation of mass flux and momentum flux across the shock region yields the two Rankine-Hugoniot (RH) conditions for an iso-thermal fluid

$$\rho_1 u_1' = \rho_2 u_2' \tag{2.5}$$

$$\rho_1 u_1'^2 + P_1 = \rho_2 u_2'^2 + P_2, \tag{2.6}$$

where primes here indicate a flow velocity in the co-moving (shock) frame.

Equations (2.5) and (2.6) can be combined, and non-dimensionalized, into the form

$$M_1' + \frac{1}{M_1'} = M_2' + \frac{1}{M_2'}. \tag{2.7}$$

There are two possible values of M_2' corresponding to a fixed upstream Mach number M_1'. The first is trivial, $M_1' = M_2'$, and is not a shock. The non-trivial solution,

$M_2' = 1/M_1'$, shows that both flows are in the same direction, and that a super-sonic upstream flow ($M_1' > 1$) must shock to a sub-sonic downstream flow ($M_2' < 1$) or vice versa.

Returning from the reference frame moving with the shock's speed, M_s, to the lab frame, expressed without primes, the RH condition becomes

$$M_1' M_2' = (M_1 - M_s)(M_2 - M_s) = 1. \tag{2.8}$$

This can be solved to obtain the speed of the shock in terms of the upstream and downstream flows

$$M_s = \frac{M_1 + M_2}{2} - \sqrt{\left(\frac{M_1 + M_2}{2}\right)^2 - (M_1 M_2 - 1)}\ . \tag{2.9}$$

The quadratic root selected is that which returns a stationary shock ($M_s = 0$) when the flows satisfy the conditions for a stationary shock ($M_1 M_2 = 1$). Solutions like this are shown by purple curves on each panel of Figure 2.3. The jump satisfies both the RH conditions and the requirement that $\mathcal{C}_3$ decrease due to viscosity. As a result of these combined conditions the jump must take super-sonic upstream flow to subsonic downstream flow – the opposite transition is not possible. Cases where $M_2 \neq 1/M_1$ will produce a propagating shock. When, for example, $M_2 < 1/M_1$ the shock speed $M_s < 0$ and the shock propagates leftward offering the possibility of resetting the left boundary condition.

The colored curves in Figure 2.3 show various steady solutions. The blue lines in each panel are solutions entering with supersonic velocity, varying slowly and always remaining supersonic. The purple line on the left enters with the same boundary conditions as the blue line, but experiences a shock that drops it to the critical contour. This shock satisfies $M_2 = 1/M_1$, leaving the shock to remain stationary where it reached that equilibrium. This particular case shows that the steady flow solution is not necessarily uniquely specified by the left boundary condition. Only by solving the time dependent equations can we find the particular steady solution which a given initial condition will give rise to.

2.3.3 Time Dependence

In order to resolve the ambiguity described above, and find the steady solution corresponding to a particular initial condition, we solve the time-dependent equations until they settle to a steady state. We assure a transient time dependence by using initial conditions that cross forbidden contours, such as those shown in the blue dashed lines in Figure 2.4. We then follow the flow's evolution in time. A shock first occurs at a region of area decrease, causing a supersonic flow to compress. For the nozzle, this shock would occur before the throat of the nozzle where compression slows the flow. These initial shocks are the long dashed purple lines in Figure 2.4. When a shock does form, then Equation (2.9) predicts the direction of motion from the values of M_1 and M_2. The shock will move either to a place where $M_1 M_2 = 1$ or until it reaches the boundary of the computational domain. If it propagates to the left edge of the domain it has effectively over-ridden the boundary condition, as in the lower red curve of the left panel in Figure 2.4. This suggests a case with no valid steady state solution for the boundary condition, as was the case for the horizontal blue line used in that case. If the shock moves to the right boundary, then the shock is completely transient and a flow with no shocks satisfies the conditions imposed, such as as the upper red curve in the right panel of Figure 2.4. However, if the shock finds a place that allows for $M_s = 0$, then this set of boundary and initial conditions allows for a non-smooth steady solution this is seen in the red curve of the left panel in Figure 2.4.

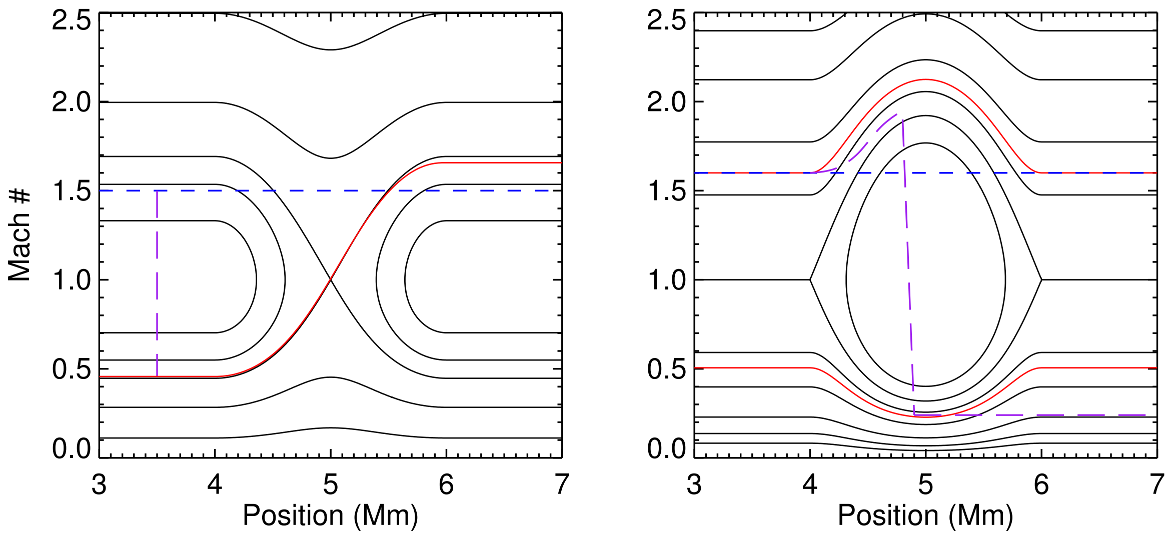

Figure 2.4: Left: The contours for Laval's nozzle. Right: The contours for our chamber. Overplotted onto both are the initial flow in the short dashed blue line, the final solutions in red, and the intermediate solutions in long dashed purple.

The chamber behaves differently. When the shock forms, it still appears first within the forbidden region. The forbidden region in the chamber is also where the area is changing, and as a result we can no longer expect that the shock is stationary when $M_1 M_2 = 1$. If a shock forms and leaves the chamber, then we can use Equation (2.9) to predict its motion. We expect that there still exist boundary conditions that will have multiple steady solutions depending on the initial conditions applied to the flow. Given the lack of an analytic tool that could solve shock motion for the chamber like we have the nozzle, we resort to numerical solution.

2.4 The Numerical Code: HST1D

To investigate the temporal evolution of flows through a chamber, we developed a code that advances one dimensional hydrodynamics called Hydrodynamic Shock Tube 1 Dimension (HST1D). The code assumes an isothermal ideal gas and time-advances the governing equations

$$\frac{\partial \rho}{\partial t} + \frac{\partial}{\partial x}(\rho u) = 0, \tag{2.10}$$

$$\frac{\partial u}{\partial t} = -u\frac{\partial u}{\partial x} - c_s^2\frac{\partial \ln(\rho)}{\partial x} + \frac{4}{3}\frac{\mu}{\rho A}\frac{\partial}{\partial x}(A\frac{\partial u}{\partial x}) \quad , \tag{2.11}$$

where x is position along the flux tube, with positive to the right and the left edge as the origin.

HST1D is a finite difference code that advances Equations (2.10) and (2.11), with the goal of reaching a steady solution. It uses a staggered Eulerian grid, with velocity and density defined on cell edges and center centers respectively. The continuity equation is treated with an upwind differencing, for stability. The momentum equation is solved semi-implicitly with the viscosity calculated via the Backwards Euler (BE) method. The remainder of the momentum equation is calculated explicitly using centered differencing.

The code is evolved using fourth order Runge-Kutta (RK4) stepper that chooses step sizes based on the Courant-Friedrichs-Lewy (CFL) conditions for Equations (2.10) and (2.11). The code steps through its RK4 step and then a single BE step was taken afterward. This allows us to bypass the CFL condition for the viscosity.

The simulation's left boundary specifies an incoming density and velocity, which remain constant on the left edge of the domain. The right boundary has a Neumann condition on density and velocity, simulating an open boundary. We also specify an area profile for each run. The area is scaled to the incoming area, A_{inc},. The profile expands to a peak area $A_{\mathrm{pk}} > 1$. We choose a particular shape for this expansion, and subsequent constriction

$$A(x) = (A_{\mathrm{pk}} - A_{\mathrm{inc}})\sin^2\left(\frac{x - x_o}{2\pi w}\right) + A_{\mathrm{inc}} \tag{2.12}$$

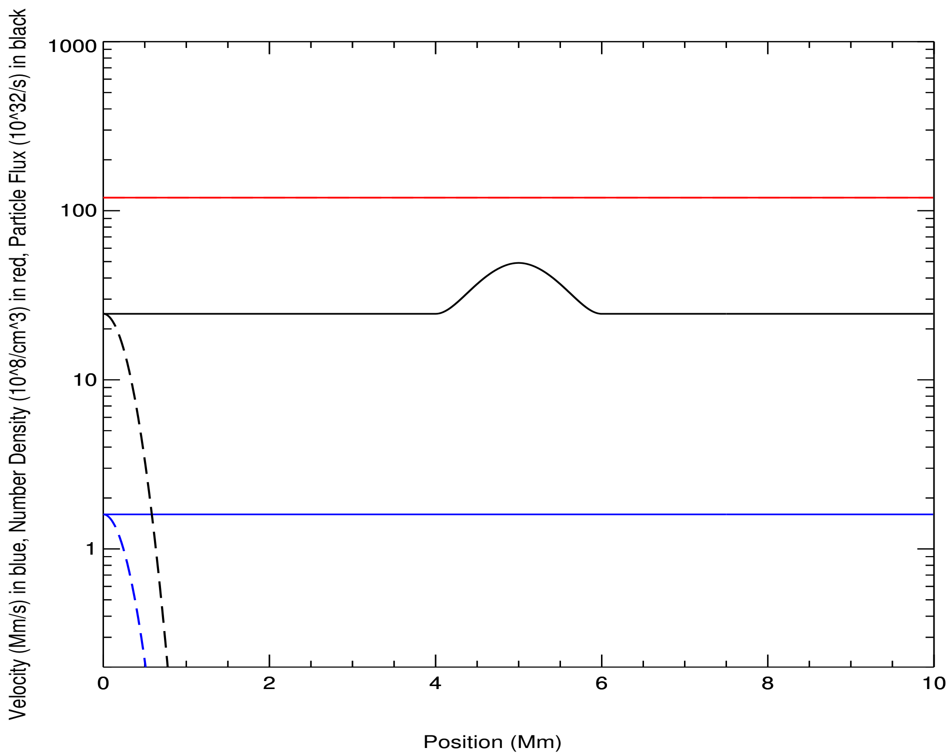

Figure 2.5: Initial Configuration of a HST1D run. Density is in red, the mass flux is in black and velocity is in blue. The flat initialization is shown in solid lines , while the gaussian initialization is dashed. Note that the density remains the same so that the mass flux drops off like a gaussian.

where, w and x_o are the width and starting position of the chamber. This form is used to set $A(x)$ and $\partial A(x)/\partial x$ match to the flat regions outside the chamber. Each chamber starts at $x = 4$ and uses a width of $w = 2$.

The simulation is initialized in one of two different ways, in an attempt to find the region where the initial conditions determine the solution. Both initial conditions are shown in Figure 2.5. The first is named "flat", as both the velocity and density take the value of the left boundary and replicate it across the domain. The second is named "gaussian" as we set the mass flow $\dot{m}(x) = \rho u A$ to a gaussian centered at the left boundary. The density is constant as in the flat case, in order to begin the run with fluid throughout the tube. The gaussian profile of mass flow is therefore produced by a velocity field with that profile. We also give a value for the dynamic viscosity, which is uniform in space. With these initial values and the boundaries we advance the code for 1000 seconds or approximately 13 sound transit times of the whole domain.

2.4.1 Example Run

To illustrate the evolution of the flow, we present an example case. The simulation is initialized with a Mach number of 1.6, $A_{\rm pk} = 2.0$, a dynamic viscosity of 0.1, a resolution of 0.01 megameters, and a number density of $n_e = 1.19 \times 10^{10}\,\mathrm{cm}^{-3}$, assuming a completely ionized hydrogen plasma. The initial conditions are set to the flat profile, leaving the density and velocity constant through the domain. Figure 2.6 shows the evolution of the simulation, left to right, top to bottom.

The initial profile is in panel (a), on the top left. As the flow enters the chamber, the supersonic flow speeds up in the widening area, and the density begins to drop. The right hand side of the chamber thus becomes over-dense as the excess material is pushed into it, this can be seen in panel (b). At the middle of the chamber the fluid begins to slow and become more dense. These two effects create a plug of material and the slope between the two halves of the chamber begins to steepen, as seen in panel (c). Some of the excess material exits the chamber as a pulse of higher density, but there is too much in the chamber to stop a further steepening of the slope. The slope has now steepened to near vertical and physically a shock has formed inside the chamber, on the right hand side this is visible in panel (d). This shock has $M_1M_2 < 1$ so the shock begins to move leftward. This is shown in panel (e). Finally, the shock comes to rest near the left edge of the chamber despite the product M_1M_2 being less than unity. Once the shock has come to rest as it has in panel (f) then it remains in that location for the duration of the simulation. We take this to be the steady solution.

2.5 Results and Analysis

Using HST1D we explored a section of parameter space show in Figure 2.7 and found that there exists a region where standing shocks exist as a steady state feature inside the chamber. This region is embedded in between a region of smooth subsonic solutions and one of smooth supersonic solutions. The existence of a shock depends on the three variables we varied: incoming flow velocity, peak chamber area, and viscosity. During the evolution, the shock forms on the right side of the chamber as a result of the over-density there caused by the narrowing area. In the majority of cases with a steady shock, it then moves left to near the upstream end of the chamber where it settles. If the shock forms but does not remain in the chamber it will propagate to either boundary where it either leaves the simulation (RHS) or it effectively resets the left boundary condition. In the case of the shock exiting the left side of the chamber, this suggests that there is no steady solution for that set of initial and boundary conditions. From the end of each simulation we gather the following information: the existence of a standing shock, location of said shock, and outflow velocity. In addition we have the steady solution itself, giving the density and velocity profiles as a function of position.

Some general trends in this space for the shocked solutions are evident in Figure 2.7. Shocks form in the range of Mach 1 to Mach 1.9. The presence of the shock pushes the flow to near the critical contour. As a result of this the flow exits the chamber near the sonic velocity. This attraction to the sonic outflow is a result of processes discussed previously, whereby the viscosity acts to lower the value of $\mathcal{C}_3$, which is representative of a loss of energy to viscosity. Larger values of A_{pk} can sustain shocks of a higher inflow velocity. The larger the value of A_{pk} the slower the flow that lies on the critical contour, while the flow is inside the chamber. The combination of those two effects result in a larger increase in density and drop in velocity.

The position of the shock is also sensitive to the flow speed and chamber area, while the viscosity controls the steepness of the shock. As the inflow velocity is increased the shock's position moves rightward from the left edge. This movement shows that increasing the ram pressure of the flow pushes the stable position further into the chamber. Increasing the peak area moves the shock towards the edge from the center, showing dependence upon the slope of the area as a function of position. Together these dependencies give us the sense that that the expected steady state for the shock, $M_1 M_2 = 1$, is being altered. We expected the changing cross-section of the chamber to affect the stationary solution.

2.5.1 Synthetic Lines

A single canopy cell includes flux tubes of all configurations, including chambers with various values of A_{pk}. A spectrograph with modest spatial resolution will include an ensemble of different shocks within a single pixel. EIS has a resolution of 1" and, given the size of these features, is unlikely to be able to isolate one. IRIS has a resolution of 0.33" and as such may be able to resolve a single chamber in a pixel. However, given that pixels are frequently rebinned to improve statistics, it may require a strong line to observe. To simulate this composite observation we generate spectral lines from each steady solution, and then combine them. The first step in this process is to combine elemental gaussian line profiles from each cell in a single steady-state flow solution. Each cell is small enough that properties can be taken as uniform and it will contribute to the spectrum a gaussian centered at the velocity of the cell with a thermal line width. This gaussian should have an integrated intensity proportional to the emission measure of the cell,

$$EM = \int \rho^2 A \, dx = \dot{m} \int \frac{\rho}{u} \, dx = \rho \dot{m} \frac{\Delta x}{u}. \tag{2.13}$$

where Δx is the length of the cell.

The emission from an entire chamber is a sum of its component cells. To build this we first construct a Gaussian for each cell. For clarity and generality, we scale the wavelength λ using the rest wavelength, λ_0, and the hydrogen thermal speed, which is also the isothermal sound speed. Our spectral shape is therefore a function of the dimensionless velocity-like variable

$$v = \frac{\lambda_0 - \lambda}{\lambda_0} . \tag{2.14}$$

A given cell contributes a Gaussian in v centered at $v = u/c_s$, with width $\sigma_T = 1/\sqrt{m_a}$, where m_a is the atomic mass of the ion species under consideration,

$$f(v) = \frac{EM}{\sigma_T \sqrt{2\pi}} \exp\left[\frac{-(v - M)^2}{2\sigma_T^2}\right] . \tag{2.15}$$

Since our staggered grid assigns velocities to a cell's edges, we average those edges to obtain the single Mach number M used in Equation (2.15).

To illustrate this point, we begin by creating a series of spectral lines for each cell in some example chambers, using oxygen as our emitting species (i.e. $m_a = 16$). In the left panel of Figure 2.8, we see a subset of curves for a chamber that does not contain a shock. These are all roughly the same amplitude and shape, with only slight variation due to the decrease in velocity and increase in density as the flow passes the chamber's center. The right panel, on other other hand, shows a selection of spectra from a chamber which does contain a shock. The collection of small lines are from cells upstream of the shock as seen in the upper right panel. The remaining curves in the right panel are from cells past the shock. The larger amplitudes come from the cells near the center of the chamber, where the density is near its peak and the velocity near its minimum. The cells near the shock exhibit emission measure enhanced by about an order of magnitude enhancement, and subsonic peak velocities. As the flow moves through the chamber, the velocity nears Mach 1 and the amplitude drops off accordingly. The cells near the exit of the chamber show intensity enhancements of a factor of 3 and a peak velocity that is sonic.

The next step is to assemble all a solution's cells into a single spectral line profile for the entire chamber. This is a sum of the spectral lines from the individual cells shown in Figure 2.9. The red curve is the sum from the chamber shown in the left panel of Figure 2.8. Its mean velocity is slightly blue shifted from the inflow velocity, but overall it is very close to a simple gaussian. The black curve is the result of the chamber in the right panel of Figure 2.8, which did contain a shock. These two cases have the same inflow speed, but the end result is strikingly different. First the amplitude of the shocked chamber is nearly an order of magnitude larger than the unshocked chamber. Second is that the peak is now substantially subsonic, as a result of the emission measure enhancement downstream of the shock. Finally, this curve shows a significant blue tail, resulting from the emission from upstream of the shock. The green curve shows a case with even greater expansion, $A_{\rm pk} = 3.0$, showing emission peak at a slower speed, and still greater amplitude.

An observed spectral line, even from a single pixel along a slit, is likely to include contributions from several field lines with different chamber geometries. Slit pixels are often combined to reduce noise, this will combine even more field lines into a single spectrum. To account for this observational reality, we combine the synthesized spectra from many different simulations, with different values of $A_{\rm pk}$ but the same inflow Mach number. We form this superposition based on the relative frequency of each value of $A_{\rm pk}$ as shown in Figure 2.2.

To build the composite spectrum, we start with a selection of chambers, spanning the range of areas for a single inflow velocity. In this case there are two general populations of curves. The smaller faster curves are from chambers without a shock. The larger slower population is then from the chambers that contain shocks. This collection of composite spectra is shown in the lower left panel of Figure 2.10.

The lower right panel of Figure 2.2 shows, as a cumulative distribution function (cdf), the relative frequency with which each value of $A_{\rm pk}$ occurs in the model canopy. The corresponding probability distribution function (pdf) is plotted as a histogram in the top panel of Figure 2.10. We use the histogram frequencies as weights in the construction of the composite spectral line shown in the lower right panel. In the upper panel, the overall histogram is shown, the inset highlights the 30% of flux tubes with actual chambers; the remaining 70% have monotonically increasing area profiles. We multiply each spectrum by its frequency from that histogram, and sum the weighted spectra to form a single composite spectral line. The result as shown in the right panel of figure 2.10. Each curve in this panel corresponds to the spectrum of the same color from the lower left panel scaled by its frequency. While chambers compose a relatively small fraction of the total, their disproportionately higher emission measures gives a significant role in the composite spectral line.

This composite spectrum is intended to represent an observation which has been integrated over time and space. It shows how the best-resolved line profile appears for a given inflow Mach number. The example case assembled in Figure 2.10 shows emission from a line of oxygen ($m_a = 16$) for inflow Mach number $M = 1.6$. Different ions with different inflow speeds are explored in Figure 2.11.

The colors show emission from different atoms, iron (black), hydrogen (red), magnesium (orange), and oxygen (green). The dashed lines are composite spectra with an inflow velocity of $M = 1.2$, and the solid is $M = 1.6$, both of which have shocks in some fraction of their tubes. As atomic mass increases, the overall profile narrows. This results in a clearer separation between the shocked and un-shocked components of the lines. This is especially clear in the solid lines, as we progress from hydrogen, which is broadened enough that it is hard to distinguish any shocked component, up through oxygen, magnesium and to iron where this is very clearly a two component function. For lower inflow speed (dashed) there is smaller separation between the shocked and un-shocked components.

The two peaks of the composite spectral lines may not be resolvable depending on the line observed, for example the broad Fe XXI line at 1354 $\AA$. Looking at the general properties of the curves can be helpful. The curves of the same inflow Mach number share the mean, for $M = 1.6$ the mean is $M = 1.14$, and the Mach 1.2 inflow has a mean of Mach 0.83. The variances change with species and generally decreases as the ion mass increases, this results in the clearer separation of the fast and slow components of the flow through the chambers.

2.6 Discussion

We have presented a possible explanation for the discrepancy between the observed subsonic evaporation velocities and the supersonic flows found in earlier simulations. In our proposal, the discrepancy is resolved by variation in cross sectional area through which the evaporation flow is driven. When evaporative flows are driven through chambers in the magnetic canopy, it can shock to produce high-density subsonic flows. Chambers should exist in some fraction of the flux in a canopy; in our simple model they occur in approximately one-third of all flux tubes. Even though they are a minority of flux tubes, the enhanced post-shock emission permits these features to account for a significant fraction of the observed spectral line.

We have adopted a very simple model in order to fully explore this heretofore unexplored effect. Among the effects we have neglected in our simplified model, two are worth noting in particular. The first is a result of the simulation and partial distribution function. Our time-dependent simulation was unable to handle peak expansion areas $A_{\rm pk} > 3$ reliably. Greater expansions are expected to produce even larger post-shock densities, and thus contribute disproportionately to the composite spectral line. On the other hand, they compose a very small fraction of the flux; they are 2% of the flux in our model canopy. We therefore decided to use the single run with $A_{\rm pk} = 3$ to stand for all chambers with greater expansions. This has the effect of under-representing the effects of larger shocked chambers, this then reduces the slow peak in the composite spectra.

The second effect worth noting is our use of an isothermal model. Our neglect of temperature variation manifests itself in two ways. When we report the mean velocities from the synthetic lines, these have the same sound speed as the upstream velocity. A shock occurring in the corona would in fact increase the temperature and therefore the sound speed. Without the isothermal assumption the density enhancement of the shock would be reduced. So it is likely that in the corona the enhancement in emission would be smaller, but also that the mean outflow velocity would be entirely subsonic. The other issue stemming from the temperature is that we cannot examine the actual lines emitted by this plasma. For example it is possible that a hot line would only be visible after it is heated by the shock. This would result in a much simpler line profile than those shown in Figure 2.11, but would be centered around a subsonic velocity.

This work shows the importance of considering flux tube geometry in models of chromospheric evaporation. For example, Peres & Reale (1993) simulated chromospheric evaporation through a flux tube of constant cross section. During the evolution of their simulations, the evaporation goes through a phase that produces similar spectra to our results. There is a double peaked spectrum, with one peak near the rest wavelength and one significantly blue-shifted. This can be attributed, in their case, to a transient shock leading the evaporation. In our case, we see a similar effect but for a longer duration, due to a standing shock. This is encouraging as the simulations undertaken in that work did not use the isothermal approximation, leading to more realistic results.

In future work we will explore these effects in more realistic simulations. The PREFT code, for example, Longcope & Klimchuk (2015), includes a realistic energy equation, and can reproduce a fairly reasonable chromospheric evaporation. When a variation in magnetic field strength is included we expect to see standing shocks in the chromosphere under appropriate geometries.

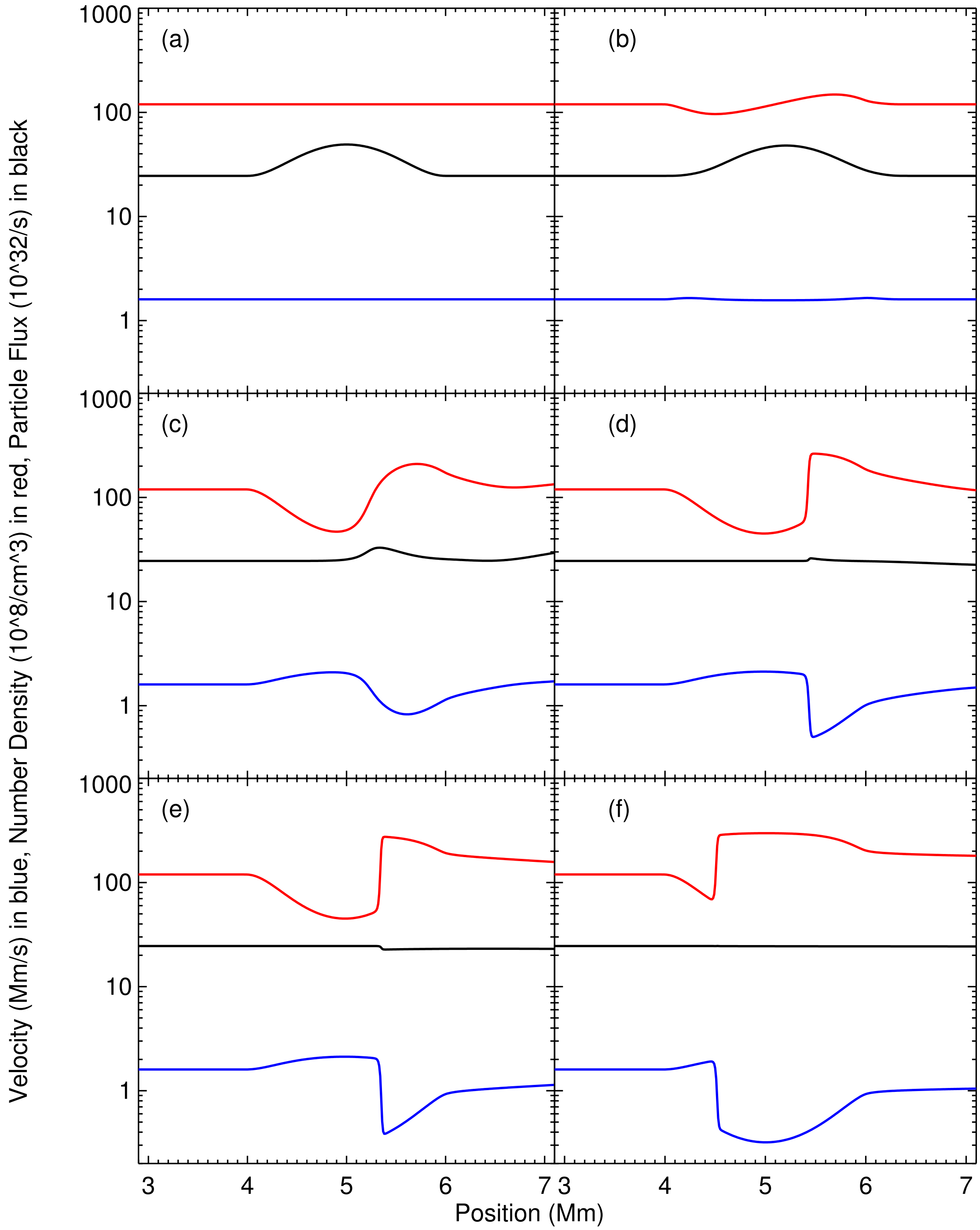

Figure 2.6: Time sequence of an example HST1D run, initial conditions: Mach 1.6, expansion ratio of 2, dynamic viscosity 0.1. Panel (a) the initial configuration,(b) at one second in you can see the over-density forming in the chamber,(c) the over-density steepens as some excess material leaves the chamber,(d) The over-density has now steepened into a shock,(e) the shock proceeds leftward,and (f)the shock has settled into a stable position.

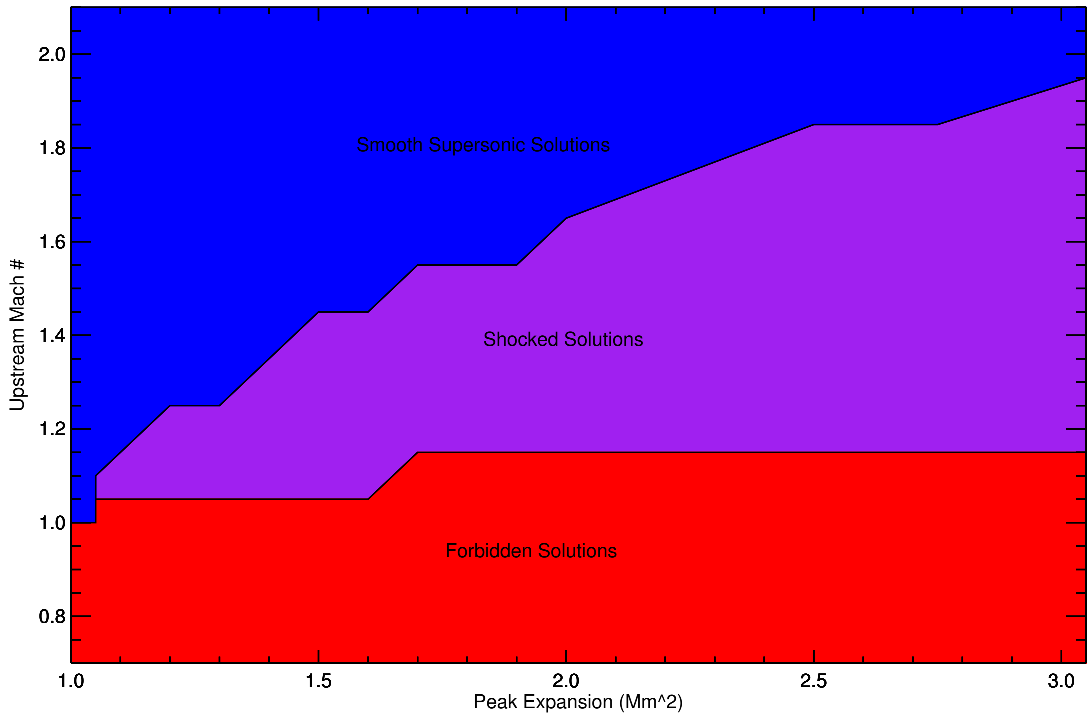

Figure 2.7: Parameter space spanned by this work as functions of upstream velocity and peak expansion of the chamber and initialized with the flat condition. The blue region is the set of parameters that result in a solution that smoothly follows supersonic contours. The purple region is where the evolution of the flow results in a standing shock in the chamber. The bright red region is where the simulation shows no solution for the initial conditions chosen.

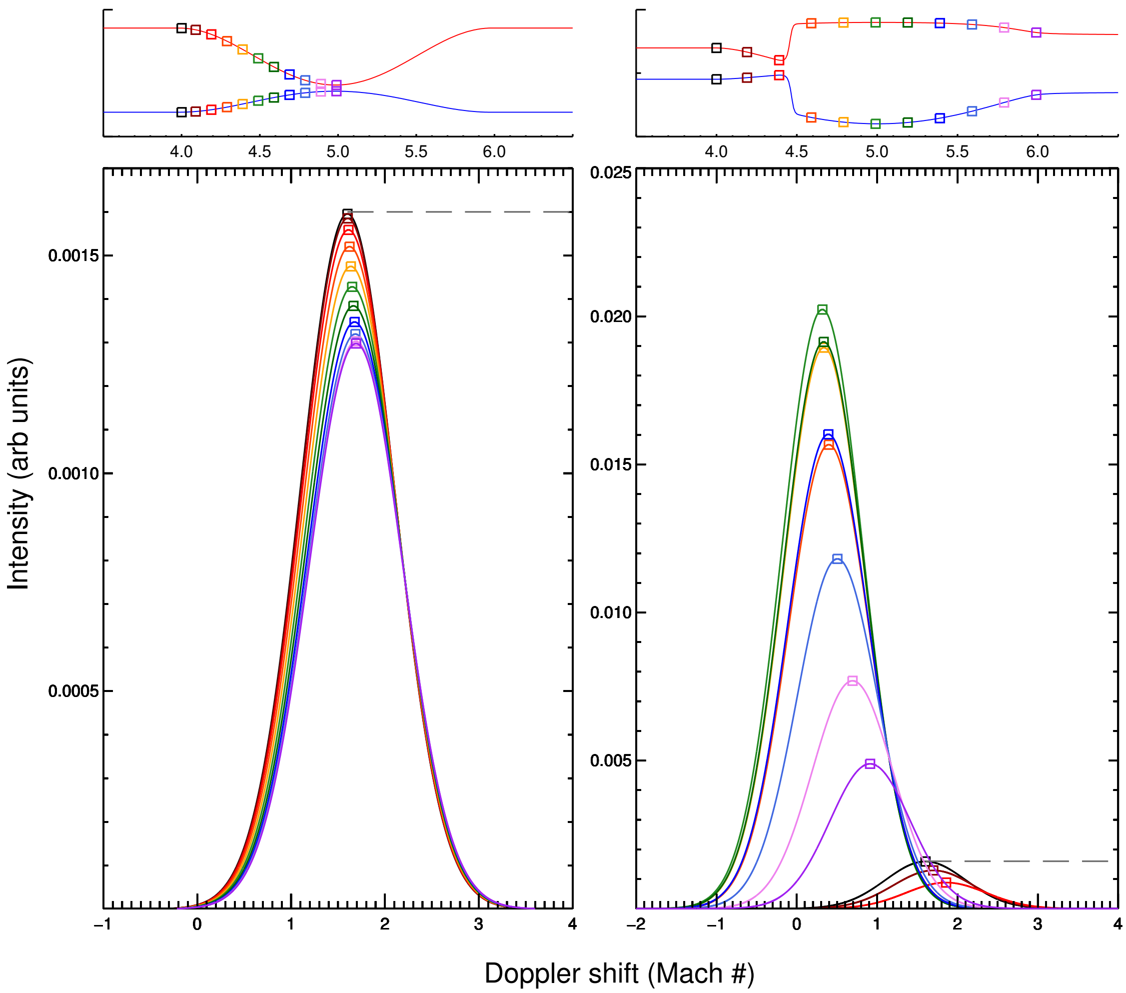

Figure 2.8: The synthesis of a spectral line for a single chamber. Left and right columns show, respectively, cases without and with a shock, both with inflow Mach number $M = 1.6$. The upper panels show scaled version of the density (red) and velocity (blue) for each case. Colored boxes show positions at which spectra are shown in the lower panels in curves of the same color. The vertical scale of the right panel is expanded to accommodate the higher post-shock emission. For comparison, the gray dashed line designates the line from the left edge of the chamber, which has the same for both chambers.

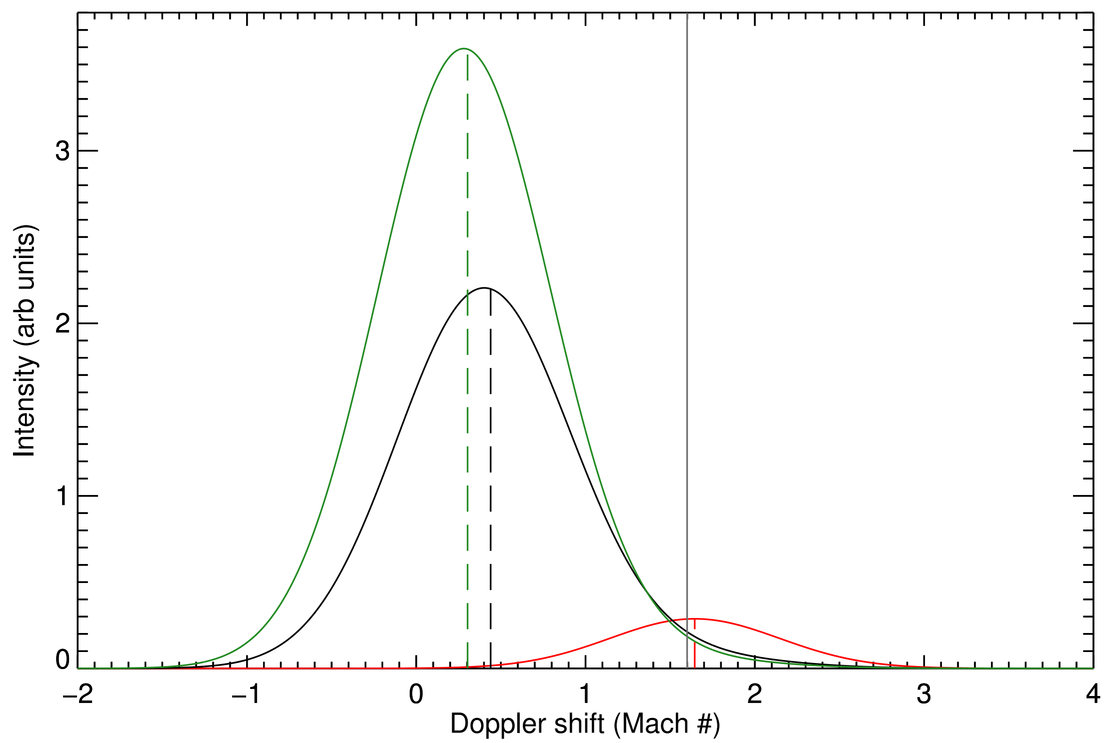

Figure 2.9: Three composite spectra for solutions with inflow Mach number $M = 1.6$. The red curve is the combined spectrum from a chamber with peak area of $A_{\text{pk}} = 1.1$, which had no shock. The black and green curves are from a chambers of $A_{\text{pk}} = 2.0$ and $A_{\text{pk}} = 3.0$, which did include shocks. The vertical dashed lines mark the mean velocity of each curve, while the solid vertical line shows the inflow velocity for all three chambers.

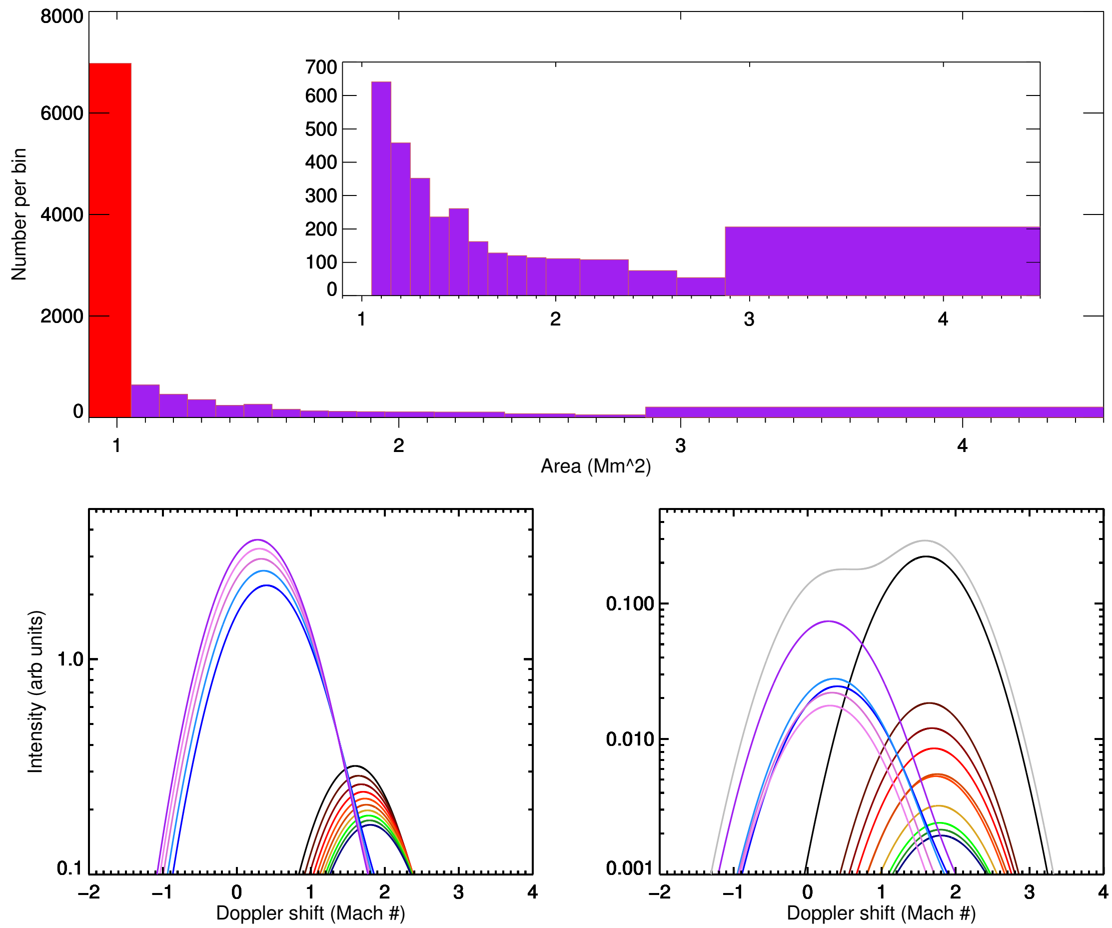

Figure 2.10: Bottom left panel: A collection of composite spectral lines for chambers with with inflow Mach number $M = 1.6$, and peak areas ranging from $A_{\rm pk} = 1.0$ to 3.0. Top panel: shows the pdf obtained from the cumulative distribution function shown in Section 2, re-binned to the rage of areas for which we have solutions. Chambers with $A_{\rm pk} > 3.0$ are all collected into the bin with $A_{\rm pk} = 3.0$. Bottom right panel: This panel takes the curves from the bottom left panel and multiplies each by the appropriate bin of the histograms and then scales each by the total number of chambers (10000). The light gray curve overlying the others is the total of the other curves in the panel, representing the complete combined spectra.

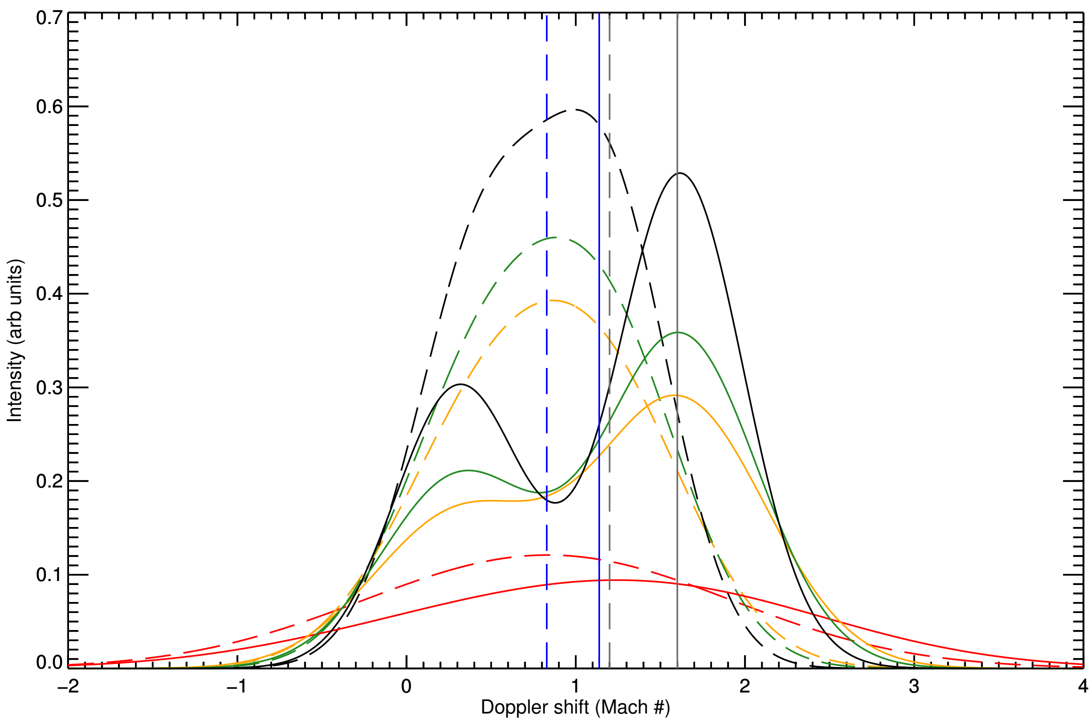

Figure 2.11: The composite spectra assembles as in Figure 2.10, for a variety of different atomic species and inflow Mach numbers. Solid and dashed curves show cases with inflow Mach number $M = 1.6$, and $M = 1.2$ respectively. The colors distinguish different atomic species: hydrogen (red), oxygen (orange), magnesium (green), and iron (black). The vertical dashed and solid lines in grey show the inflow velocity for each set of curves. The mean velocity is shown by the vertical lines in blue, dashed showing the slower intake velocity and solid the faster. The flows have a mean of $M \simeq 0.828$ and the fast of $M \simeq 1.125$.

CHAPTER THREE

MODELING OBSERVABLE DIFFERENCES IN FLARE LOOP EVOLUTION DUE TO RECONNECTION LOCATION AND CURRENT SHEET STRUCTURE

Contribution of Authors and Co-Authors

Manuscript in Chapter 3

Author: John Unverferth

Contributions: Modified framework and ran analysis for the study. Wrote manuscript save for introduction.

Co–Author: Dana Longcope

Contributions: Developed magnetic field and helped guide study. Wrote introduction and commented on drafts of the manuscript.

Manuscript Information

John Unverferth and Dana Longcope

The Astrophysical Journal

Status of Manuscript:
____ Prepared for submission to a peer-reviewed journal
____ Officially submitted to a peer-reviewed journal
____ Accepted by a peer-reviewed journal
__X__ Published in a peer-reviewed journal

American Astronomical Society
May, 2020, ApJ 894, 148
10.3847/1538-4357/ab88cf

ABSTRACT

Flare reconnection is expected to occur at some point within a large scale coronal current sheet. The structure of the magnetic field outside this sheet is almost certain to affect the flare, especially its energy release. Different models for reconnection have invoked different structures for the current sheet's magnetic field, and different locations for the reconnection electric field within it. Models invoking Petschek-type reconnection often use a uniform field. Others invoke a field bounded by two Y-points with a field strength maximum between them, and propose this maximum as the site of the reconnection electric field. Still other models, such as the collapsing trap model, require that the field strength peak at or near the edge of the current sheet, and propose that reconnection occurs above this peak. At present there is no agreement as to where reconnection might occur within a global current sheet. We study the post-reconnection dynamics under all these scenarios seeking potentially observable differences between them. We find that reconnection occurring above the point of strongest field leads to the highest density and the highest emission measure of the hottest material. This scenario offers a possible explanation of super-hot coronal sources seen in some flares.

3.1 Introduction

Fast magnetic reconnection is believed to occur within a small diffusion region localized inside a large-scale current sheet (Yokoyama & Shibata, 1994; Erkaev et al., 2000; Biskamp & Schwarz, 2001; Baty et al., 2006; Forbes et al., 2013). In spite of many theoretical investigations, there is not yet a consensus on the nature of the localized reconnection electric field nor on the site within the sheet it will occur. Small-scale modeling is often done within a current sheet separating uniform layers of magnetic field of equal magnitudes but different direction (Hesse et al., 1999; Birn et al., 2001; Karimabadi et al., 2004; Pritchett & Coroniti, 2004; Shay et al., 2007; Drake et al., 2009; Landi et al., 2015). The external field strength is uniform along such a sheet so the location of the reconnection site is irrelevant: all locations are equivalent. Such a uniform current sheet is the setting of standard Petschek models (Vasyliunas, 1975; Soward, 1982; Forbes & Priest, 1987; Biernat et al., 1987).

A class of more realistic current sheets occur as tangential discontinuities in force-free magnetic fields (Priest & Raadu, 1975; Aly & Amari, 1989; Longcope & Forbes, 2014). In two-dimensional versions, the current sheet terminates at a Y-type magnetic null point. The two-and-a-half dimensional relatives of these fields have a uniform magnetic field component in the ignorable direction, and only the other components vanish at the Y-point. In one well-known variety of this field, the Green-Syrovatskii field, the current sheet is terminated by Y-points at both ends, and has a point of maximum field strength midway between them (Green, 1965; Syrovatskiĭ, 1971). In other cases, such as the illustration in Figure 3.1, the sheet may extend upward indefinitely, but with a peak field strength some finite distance above the

Y-point.

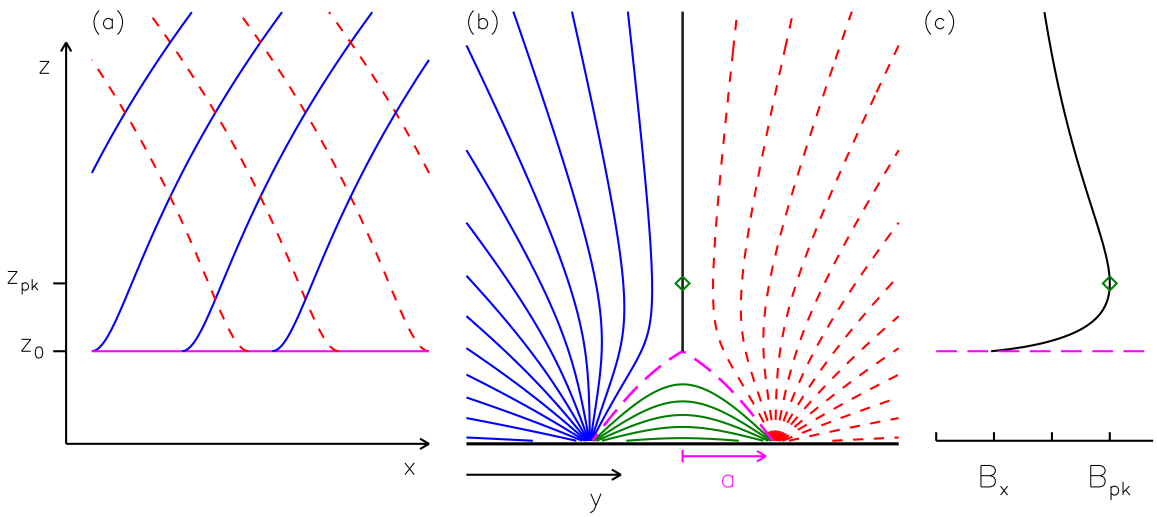

Figure 3.1: Illustration of the model field with a vertical current sheet above a single Y-point. (a) Field lines on the two sides of the current sheet, viewed face-on, in the x–z plane. Blue solid lines are upward field lines on the near side ($y < 0$) while red dashed lines are downward field lines on the far side ($y > 0$); due to the ignorable component $B_x > 0$, both field lines are directed rightward in this view. (b) The surrounding field lines in blue solid(upward), red dashes(downward) and green solid(closed). The black vertical line is the current sheet, and the magenta dashed curves are the separatrices below the Y-point. (c) The field strength, horizontally, versus height. A green diamond marks the peak, at $z = z_{\rm pk}$, which matches the diamond in panel (b).

In the more realistic geometries reconnection must be localized to some point, or small region, within the current sheet. As mentioned above, microscopic modeling has not yet reached a conclusion on where that point might be. There are, broadly speaking, three possibilities for its location wrt. the Y-point and field-strength maximum. Reconnection may occur precisely at the maximum, or it may occur on the side nearer to (below), or farther from (above) the Y-point. In every case, the newly reconnected field will be swept along the current sheet, away from the site of reconnection by reconnection outflows, driven by magnetic field line retraction. In the first two cases this retraction will move the flux into regions of the current sheet with weaker field. In the third case, reconnection above the peak, the retraction will move the flux toward the peak, and therefore into *stronger* field.

Different models of reconnection-powered solar flares have assumed reconnection in each of the possible locations. Modeling by Forbes et al. (2018) posited reconnection at the point of peak magnetic field strength. The surface current density of the sheet is maximum there, so in models where the reconnection electric field is directly related to current density, such as resistive MHD, the reconnection would occur there. Alternatively, models which invoke a collapsing trap assume that reconnection occurs above the point of peak field strength (Levine, 1974; Somov & Kosugi, 1997; Karlický & Kosugi, 2004). The retracting field is then drawn into regions of increasing magnetic field strength, leading to particle acceleration by some variant of the betatron mechanism. Such a scenario implies a reconnection point above the field-strength maximum. In models with more complicated version of Ohm's law (i.e. generalized Ohm's law) the peak electric field need not coincide with the peak current density (Bhattacharjee et al., 2009; Biskamp & Schwarz, 2001; Forbes et al., 2013). An example of this geometry is found in the model of the flare on 10 Sept. 2017 by Longcope et al. (2018) which used EUV data to infer that reconnection-driven downflows were moving into increasing field strength.

Theoretical modeling and direct observation have not yet provided definitive evidence of where the reconnection occurs within the current sheet. It is expected, however, that differing locations will lead to differing dynamics, and thereby differing observable consequences. For example, the temperature and density of the outflowing plasma will depend on the variation in confining magnetic field through which it moves. Retraction into field of increasing strength will compress the flux, driving up its density. The present work will characterize these differences and their observable consequences by simulating retraction from different reconnection sites in a current sheet.

3.1.1 A Current Sheet Model

The full range of behaviors can be investigated using a single model equilibrium current sheet inspired by Longcope & Forbes (2014). The effects of different locations of the reconnection electric field are investigated by specifying different locations within the common model current sheet. We begin with a two-dimensional magnetic field, $(\boldsymbol{y}, \boldsymbol{z})$, due to two photospheric sources, $(y, z) = (\pm a, 0)$, which is current-free except within a single, vertical current sheet along $y = 0$, $z > z_0$. The model field, taken from a modification of that in Longcope & Forbes (2014), is shown in Figure 3.1b and includes open upward and downward field lines, shown as blue and red respectively, separated by a vertical current sheet (black line) extending indefinitely upward from a Y-point at $z = z_0$. The closed field lines below the Y-point, shown in green, form the magnetic arcade. It is surrounded by a separatrix linked to the Y-point, shown in magenta.

Just outside the current sheet (i.e. at $y = 0$) the vertical component of the magnetic field

$$B_z(z) \;=\; \pm\,\frac{2B_0\,\sqrt{(z_0^2+a^2)\,(z^2-z_0^2)}}{z^2+a^2} \qquad , \qquad z \;\geq\; z_0 \;\; , \tag{3.1}$$

changes sign from upward (upper sign) on the $y < 0$ side, to downward (lower sign) on the $y > 0$ side. In this expression B_0 is the peak of $|B_z|$, and a and z_0 are the locations of the sources and Y-point as described above. The dynamics of the retraction will be governed by the field strength just outside the sheet. Including an ignorable component, B_x, the field strength along the model current sheet is

$$B(z) \;=\; \sqrt{B_x^2 + B_z^2(z)} \;=\; \sqrt{B_x^2 \;+\; 4B_0^2\,\frac{(z_0^2+a^2)\,(z^2-z_0^2)}{(z^2+a^2)^2}} \quad , \qquad z \;\geq\; z_0 \;\; , \tag{3.2}$$

plotted in Figure 3.1c. The field assumes its minimum value at the Y-point, $B(z_0) = B_x$, that of the ignorable component alone. It achieves its maximum value, $B(z_{\rm pk}) = \sqrt{B_x^2 + B_0^2}$, at $z_{\rm pk} = \sqrt{a^2 + 2z_0^2}$, indicated by diamonds on Figs. 3.1b and c. It is evident from the edge-on view (Figure 3.1b) that field lines outside the current sheet (red and blue) curve inward toward the current sheet. These field lines most closely approach the current sheet at the field-strength maximum, leading to it sometimes being called the *pinch point* (Forbes et al., 2018). This point serves as a marker for the strongest external field outside the current sheet.

We will consider scenarios where reconnection occurs at the pinch point as well as scenarios where it occurs elsewhere. As mentioned above, many models place the point of magnetic reconnection at the pinch point (Forbes et al., 2018). That location has the largest current surface density so if the sheet thickness were uniform it would have the highest current density. Under classical Ohm's law with uniform resistivity the electric field would be greatest there making it the most likely point for reconnection. There are, however, many reconnection models in which the electric field is maintained by collisionless processes (Bhattacharjee et al., 2009; Biskamp & Schwarz, 2001; Forbes et al., 2013), and reconnection may occur away from the point of peak surface current. For this reason we consider reconnection sites away from the pinch point.

We investigate the dynamics of magnetic energy release triggered by magnetic reconnection localized to some point within the model current sheet described above. We do this by specifying a point of magnetic reconnection, $z_{\rm rx} > z_0$. Fixing this to be the pinch-point, $z_{\rm rx} = z_{\rm pk}$, provides the first scenario whereby a reconnected flux tube will move into ever weaker field, and will therefore *expand* as it retracts; we hereafter call this the *expanding case*. Locating the reconnection site below the peak, $z_{\rm rx} < z_{\rm pk}$, would likewise lead to monotonic expansion following reconnecting. We therefore choose not to separately investigate this case. On the other hand, we expect a reconnection site *above* the peak, $z_{\rm rx} > z_{\rm pk}$, to yield qualitatively different behavior. In this case the tube will retract into increasing magnetic field, which will lead to a compression of the flux, so we hereafter call this the *contracting case*. Once the retracting tube passes the peak it will begin expanding.

In addition to the reconnected flux retracting downward, there will be flux which retracts upward, perhaps forming an ejected flux rope. This is an equally important part of the reconnection scenario. In this work, however, we focus on that flux which constitutes the solar flare: the downward retracting flux. Hereafter we consider only that flux, and use the terms "expanding" and "contracting" in reference to the evolution of the downward retracting flux.

To pursue this strategy we choose values of a, z_0, and $z_{\rm rx}$ for the two distinct cases. We choose $z_{\rm rx} - z_0 = 30$ Mm in both cases, to give each the same distance to retract following reconnection. For the expanding case, we take $z_0 = 64$ Mm, $a = 27$ Mm and $z_{\rm rx} = z_{\rm pk} = \sqrt{a^2 + 2z_0^2} = 94.45$ Mm, as shown in Figure 3.2a. For the contracting case we choose, $z_0 = 10.0$ Mm, $a = 9.0$ Mm, and $z_{\rm rx} = 40.0$ Mm, as shown in Figure 3.2b. The fields strength peaks at $z_{\rm pk} - z_0 = 6.76$ Mm above the Y-point, so the first 77% of the retraction will be through increasing field. The two panels of Figure 3.2 are specific examples of the general field shown in Figure 3.1b. Figure 3.2 is an edge on view of the two current sheets used in this investigation. These are specific realizations of the general current sheet show in Figure 3.1. (The edge-on views shown in Figs. 3.1 and 3.2 are for context. Our model is entirely confined to

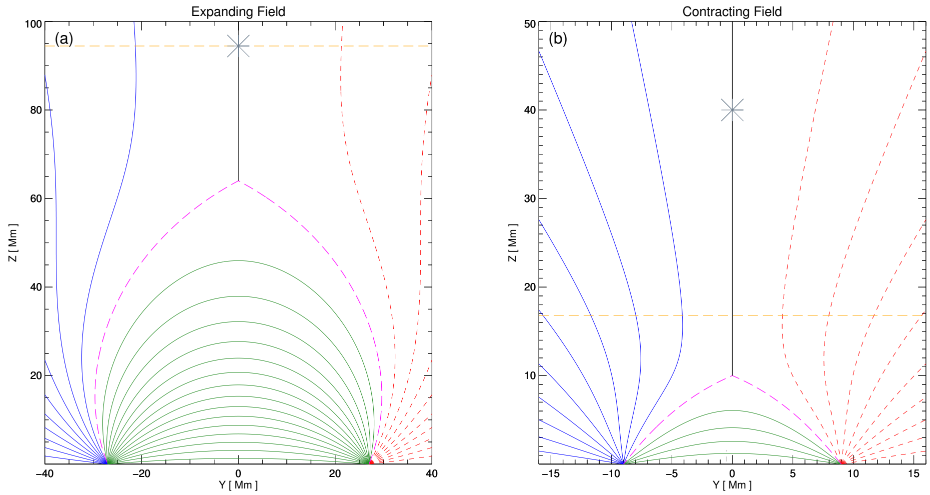

Figure 3.2: The current sheets used for the two case studies. In both panels, the magenta dashed line is a separatrix, splitting the field lines into three domains, and the solid black line marks the current sheet. The red dashed and blue solid lines are field lines that continue upward outside the upper bound of the simulation. The green solid lines are flux that has already reconnected, and is closed off underneath the current sheet. The horizontal orange dashed line marks the peak magnetic field strength. The gray asterisk indicates the specified site of reconnection. (a): the expanding case, using $a = 27$ Mm and $z_0 = 64$ Mm. (b): the contracting case, using $a = 9.0$ Mm and $z_0 = 10.0$ Mm. $z_{\rm rx} - z_0 = 30$ Mm in both panels.

the vertical current sheet – the x–z plane – so the y coordinate does not appear in it.)

We model the dynamics of flux following reconnection using the thin flux tube (TFT) approximation of MHD. First laid out for use in the convection zone and chromosphere by Spruit (1981b), and later adapted for use in the corona in Linton & Longcope (2006) and Longcope et al. (2009), this model follows the retraction of a single tube of reconnected flux as it passes through the equilibrium current sheet. The model does not consider the process of reconnection, but begins with the flux tube *just following* its reconnection at some location within the current sheet. The post-reconnection flux tube crosses from one side of the current sheet to the other, as shown in Figure 3.3. It follows an equilibrium field up one side, crosses the sheet at the specified reconnection point, $z_{\rm rx}$, and then down the other side. The otherwise force-balanced segments are thus joined together at $z_{\rm rx}$, with an angle

$$\Delta\theta \;=\; 2\,\mathrm{atan}\left[\frac{B(z_{\rm rx})}{B_x}\right] \quad , \tag{3.3}$$

between the two flux tubes — $B(z)$ is the function in Equation (3.2). Letting $\Delta\theta = 180°$ would result in anti-parallel reconnection without any guide field, and letting the angle approach $0°$ would result in no reconnection as the field lines would be parallel.

The TFT assumes that the current sheet supplies the external pressure confining the retracting tube, but that the current sheet is not affected by the tube's motion. The confining field has a fixed spatial variation, $B(z)$, given by Equation (3.2). As retraction carries it through this varying field the tube will experience a time-varying confinement pressure. A tube beginning where where $B(z)$ is maximum, namely $z_{\rm rx} = z_{\rm pk}$, will experience $dB/dt < 0$, leading to the designation of expanding. In the other case, beginning at $z_{\rm rx} > z_{\rm pk}$, the field strength will increase, $dB/dt > 0$,

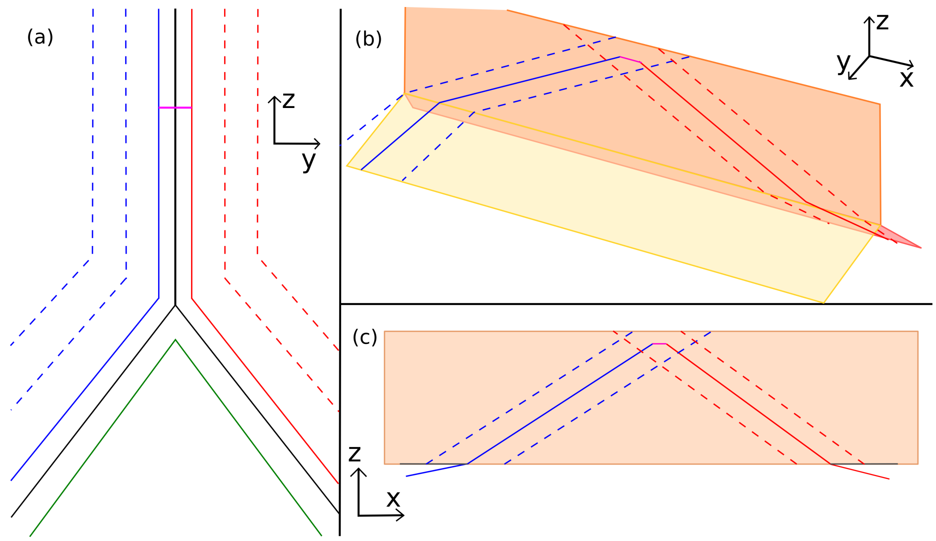

Figure 3.3: A schematic illustrating the field in three dimensions. (a) Shows a simplified edge-on view of the magnetic fields seen before reconnection, with open flux shown in red and blue, and closed in green separated by the solid black line. The solid red and blue are field lines that we force to reconnect with the magenta solid line. (b) Shows a perspective view of the same sheet, rotated to show the extent of the field line. (c) Shows the same field rotated solely into the x-z plane for a *face-on view*. The gray lines on the edge of the current sheet are the legs shown in blue and red after being moved to follow the current sheet edge.

resulting in the tube's lateral contraction. To these two cases we add a third in which B is invariant along the sheet: $dB/dt = 0$. This represents the case of a uniform current sheet, $(\partial B/\partial z = 0)$ which has been most often used in past TFT simulations (Longcope et al., 2010; Longcope et al., 2016; Longcope & Klimchuk, 2015); we hereafter refer to this as the *uniform* case.

The present work uses the TFT model to explore how the different evolution resulting from different reconnection sites manifests in flares with observably different properties. To do this we initialize the TFT with a flux tube of a given description, and follow its evolution through a current sheet of the appropriate kind: *uniform*, *expanding*, or *contracting*. The evolution of each kind is characterized in terms of observable aspects such as peak temperature, peak density as well as the full differential emission measure (DEM). Our analysis reveals that the expanding case reaches the greatest peak density and reaches this earlier than the other two cases. The other two cases, however, exhibit a high-temperature peak in their DEMs, absent from the expanding case.

The analysis is presented as follows. Section 2 introduces the thin flux tube framework and uses it to investigate the three cases in depth. Section 3 follows the evolution of each case, and comparison of common evolutionary stages. Section 4 uses synthetic observables to compare the cases against one another.

3.2 The Thin Flux Tube Model

The thin flux tube (TFT) model incorporates reconnection-driven magnetic field evolution, more typically found in full MHD simulations, with the more efficient computation and ease of 1D flare loop models. The combination is achieved by representing the flux tube as a parameterized curve, moving through a static current sheet. Because only a single curve is represented, simulations can achieve the very high spatial resolution needed to accurately capture evolution of the transition region during a flare (MacNeice et al., 1984a). While it considers transient evolution of only a single flux tube, the TFT model has been shown to match results of steady models in 2.5 dimensions (Longcope et al., 2010; Longcope & Klimchuk, 2015) under comparable conditions. The TFT model does, however, ignore possible interactions between multiple flux tubes, or interactions of the tube with the surrounding field. Nevertheless, the model serves as an important preliminary step for investigating post-reconnection dynamics.

The present investigation solves the TFT equations using the Post-Reconnection Evolution of a Flux Tube (PREFT) code. First introduced in Longcope & Klimchuk (2015) and updated in Longcope et al. (2018), PREFT advances the TFT equations on a Lagrangian grid. The tube's axis, $\mathbf{r}(\ell, t)$, is represented by a chain of Lagrangian grid points whose length coordinates, ℓ, are continually recomputed. The evolution of the axis is specified by setting the Lagrangian derivative to the fluid velocity of that fluid element: $D\mathbf{r}/Dt = \boldsymbol{v}(\ell, t)$. The fluid velocity of each element (grid point) is advanced according to the momentum equation (Longcope & Klimchuk, 2015; Longcope et al., 2018)

$$\frac{D\boldsymbol{v}}{Dt} = \frac{1}{\rho}\left(\frac{B^2}{4\pi} - p\right)\frac{\partial \hat{\boldsymbol{b}}}{\partial \ell} - \frac{1}{\rho}\frac{\partial p}{\partial \ell}\hat{\boldsymbol{b}} + \frac{B}{\rho}\frac{\partial}{\partial \ell}\left(\frac{\tilde{\eta}}{B}\hat{\boldsymbol{b}}\hat{\boldsymbol{b}} \cdot \frac{\partial \boldsymbol{v}}{\partial \ell}\right) + \frac{1}{\rho}\left(1 + \frac{4\pi p}{B^2}\right)\nabla_\perp\left(\frac{B^2}{8\pi}\right) \quad (3.4)$$

where p is the gas pressure, ρ is the mass density, and $\tilde{\eta}$ is the parallel component of the dynamic viscosity. The direction along the axis is given by the unit tangent vector $\hat{\mathbf{b}} = \partial\mathbf{r}/\partial\ell$.

The TFT model assumes the tube's plasma β is sufficiently small that the field strength within the tube matches that of the static surrounding field, $B(z)$. The tube's axis is restricted to the vertical current sheet (i.e. the x-z plane) so the surrounding field strength is given by the function in Equation (3.2). A gradient in the external field strength exerts a force perpendicular to the tube's axis through the term in Equation (3.4) featuring $\nabla_\perp$. The mass density ρ is continually recomputed along with cell lengths, $\delta\ell$, in order to conserve the mass per unit flux in each cell: $\delta\ell\,\rho/B(z)$.

The right hand of the momentum equation, Equation (3.4), includes all the forces acting on an element of the flux tube. These contributions are magnetic tension partially offset by the internal gas pressure (first term), gas pressure gradient parallel to the tube (second term), and the divergence of the parallel component of the viscous stress tensor (third term). The dynamic viscosity, $\tilde{\eta}$, is computed using the classical, temperature-dependent Braginksii form (Braginskii, 1965; Longcope & Klimchuk, 2015), although we also require a minimum viscosity to ensure resolution. The final term, first introduced by Guidoni & Longcope (2011) and incorporated into PREFT by Longcope et al. (2018), accounts for the pressure exerted by a gradient in the confining field. Prior to that modification PREFT had considered only uniform current sheets in which this term would vanish.

The current sheet abuts closed magnetic field at its lowest edge, the Y-point. Downward retraction will be halted at this point by the upward magnetic pressure from closed flux below. We model this effect simply but crudely with an *ad hoc* force term resembling a damped spring; a similar approach was adopted by Guidoni & Longcope (2011). The *ad hoc* force

$$\boldsymbol{F} = \hat{\mathbf{n}}\Big[\,k(z - z_0) - d\,(\hat{\mathbf{n}}\cdot\boldsymbol{v})\,\Big], \tag{3.5}$$

is added to the right hand side of Equation (3.4) for any tube element whose vertical position, $z < z_0$, the bottom of the current sheet. This expression uses the unit vector $\hat{\mathbf{n}} = \hat{\mathbf{y}}\times\hat{\mathbf{b}}$ which is orthogonal to the tangent vector and has a negative z component

($\hat{n}_z < 0$ since $\hat{b}_x > 0$ over the entire tube). When the tube is below the bottom of the current sheet, $z < z_0$, and the force becomes active, the first term in square brackets will be negative and will thus produce a force with an upward component — i.e. a restoring force. The second term, a Stokes-like drag, will always oppose the motion in a direction perpendicular to the axis. The two *ad hoc* constants, the spring constant k and the damping coefficient, d, are set through preliminary experimentation to minimize the bounce-back of the tube and stop its retraction in approximately one oscillation.

The temperature of the tube is advanced according to the energy equation

$$\tilde{c}_v \frac{DT}{Dt} = -T(\nabla \cdot \boldsymbol{v}) + \frac{\bar{m}}{k_B} \frac{\tilde{\eta}}{\rho} \left(\hat{\boldsymbol{b}} \cdot \frac{\partial \boldsymbol{v}}{\partial \ell} \right)^2 + \frac{\bar{m}}{k_B} \frac{B}{\rho} \frac{\partial}{\partial \ell} \left(\frac{\kappa}{B} \frac{\partial T}{\partial \ell} \right) + n_e^2 \Lambda(T) + Q(\ell) \quad , \tag{3.6}$$

where $\tilde{c}_v$ is the volumetric specific heat, T is the temperature, $\bar{m}$ is the mean particle mass, κ is the thermal conductivity, $\Lambda(T)$ is the radiative loss function, n_e is the electron number density, and Q is some heating applied to the tube. The first term on the right hand side is the adiabatic change in temperature due to the expansion or contraction of the plasma. The second term is the viscous heating, and the third term is thermal conduction. PREFT uses a classical Spitzer conductivity subject to a limiter to satisfy the free streaming limit (Longcope & Klimchuk, 2015). Using a non-uniform magnetic field requires account be taken of the varying cross sectional area, inversely proportional to field strength B, in all divergences. The fourth term in Equation (3.6) is the radiative loss function for optically thin losses, and the final term is equilibrium heating applied to the flux tube.

PREFT advances these equations through a second order time scheme, whose time steps are governed by the Courant–Friedrichs–Lewy (CFL) conditions to ensure stability. Thermal conduction alone is advanced implicitly, so this extremely stringent time-step constraint can be neglected. The endpoints of the tube are fixed in both position and temperature, resulting in closed boundaries for both equations.

3.2.1 Initial Conditions

Eqs. (3.4) and (3.6) are solved beginning with an initial condition representing the loop just following its creation by reconnection across the current sheet. The post-reconnection form is an axis like that shown in Figure 3.3, which we create in two steps. In the first step a flux tube of the desired initial length is placed in a uniform magnetic field. Temperature is initialized by assuming constant pressure, and solving for an equilibrium balancing classical thermal conduction and radiative losses against uniform volumetric heating Q (a so-called RTV equilibrium, Rosner et al., 1978). The pressure and heating rate are fixed to achieve a specified apex temperature for the prescribed half-length. After assuming uniform pressure, the solution is independent of axis geometry. This first step uses uniform cross section (i.e. uniform B) in the conduction term; the next step adjusts the heat flux $Q(\ell)$ to accommodate the actual cross section variation.

In the second step, we compute the axis of the initial flux tube. Starting at the point of reconnection, $z_{\rm rx}$, we integrate a field line by solving $dz/dx = B_z(z)/B_x$ with $B_z(z)$ taken from the lower sign of Equation (3.2). The integration ends when the field line reaches the bottom edge of the current sheet, $z = z_0$. This will occur *before* reaching the half-length specified in the first step. The extra length represents the lower leg of the tube, which would follow the separatrix above the arcade, as shown in Figure 3.3. To simplify our modeling we replace this complicated, non-planar shape with a horizontal straight leg extending along $z = z_0$, to the half length specified in the first step. This modification is illustrated in Figure 3.3c. The field strength along this straight segment is therefore uniform, $B = B_x$.

Finally, the foot of this leg is given a 3 Mm stratified chromosphere. This highly simplified layer is meant to provide a source for evaporated material. This region alone is subject to a gravitational force, which is directed parallel to the leg. By taking it to be isothermal, $T = 30,000$ K and free of heating or radiative losses, the layer will have exponential density and pressure profiles. In spite of its low temperature, it is assumed to be fully ionized at all times, and subject only to optically thin radiative losses (Longcope, 2014) when heated.

Having completed the right side of the post-reconnection field line, we reflect it to form the left side, resulting in a symmetric flux tube. Finally, to ensure that the apex of the flux tube is adequately resolved, we round off the corner where the left and right halves join. This bend represents the result of localized reconnection which made the connection through the current sheet. Once the tube is set in place we recalculate the magnetic field along the tube based on its new position in the current sheet in Equation (3.2). It is at this point that the volumetric heating, Q, is recomputed to yield a static solution to the energy equation (3.6).

The above procedure is followed for each of the three different flux tubes, using the appropriate version of Equation (3.2) in each case. Since each flux tube has the same length and the same peak temperature, our procedure gives each case the same initial density profile. The cases are therefore well suited for comparison. One small difference comes from the larger magnetic field strength we choose for the uniform case. This means its flux tube has less volume and therefore less mass per flux than the expanding or contracting cases.

The field line shape found in the second step by solving $dz/dx = B_z(z)/B_x$ is only an equilibrium solution of the momentum equation, Equation (3.4), in the limit $\beta = 0$. While a finite β could be accommodated using a different integration method, the values of β in the corona are low enough that we use the simpler method described above. In addition these flux tubes are unlikely to be in an exact equilibrium as they have just undergone reconnection.

The initial conditions for the three cases are shown in Figure 3.4. Panel (a) shows spatial configuration within the current sheet (the $x - z$ plane) from a face-on view. Each shape is a result of the relative strengths of the guide field to the current sheet field. Since these components do not vary in the uniform case its legs are straight. In contrast, the expanding case flares out toward the bottom where the guide field begins to dominate. The contracting case bows inward and then flares out. In each of these cases, the overall starting length is the same to within 700km. The apparent discrepancy in length between the uniform and non-uniform cases arises from the different angles at which they leave the base of current sheet. The uniform case also reaches higher up into the current sheet. The current sheet in the uniform case is a constant strength, and this additional height was used to keep the internal properties of the tube, along with the initial and final lengths consistent with the other cases.

Panel (b) of Figure 3.4 shows the magnetic field strength as a function of z. With this perspective it is clear that the expanding case will encounter ever weakening magnetic field during it retraction. In contrast, the contracting case will move first through increasing field before reaching the weakening field down to the edge of the current sheet. Panel (c) shows the magnetic field as a function of x. The extent of the weak magnetic field in the middle of the flux tube is clear. This is the amount of the flux tube that must undergo contraction before expansion.

The plasma properties in each case are chosen to be as similar as possible in order to focus our study on the effects of differing magnetic environments. Figure 3.5 shows the initial state of the uniform case using a format with which evolution will be plotted in the upcoming section. Panel (a) repeats the configuration from 3.4a for the uniform case alone. Panels (b) and (c) show the electron number density and

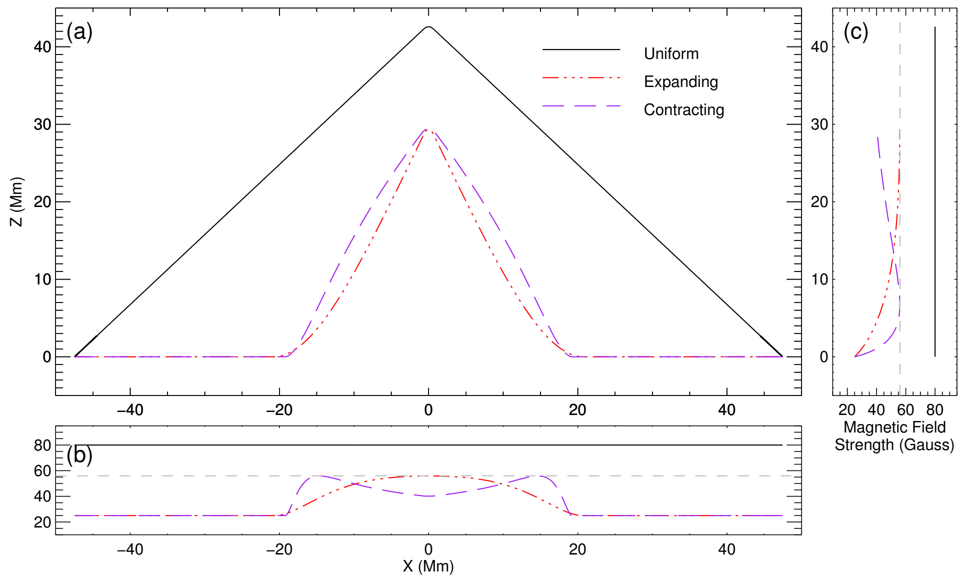

Figure 3.4: The initial configuration of the flux tube. (a) Shows the spatial configuration in the face-on view. (b) Shows the magnetic field as a function of x matching the horizontal coordinate from (a). (c) Plots the field strength horizontally *vs.* the vertical z coordinate matching panel (a). In each panel there are three cases: uniform, expanding, and contracting indicated by the solid black, dash-dot red, and dashed purple lines respectively.

pressure, respectively, from the left chromospheric footpoint to the corona, just past the midpoint. The coronal part of the flux tube has uniform pressure, as described above. The footpoint regions are isothermal, gravitationally stratified. Panel (e) shows the temperature. With a fixed minimum value in the chromosphere, the temperature then quickly rises to peak at the specified value of 3 MK at the apex.

3.3 Time Evolution of the Three Cases

The post-reconnection evolution is obtained by solving the TFT equations, (3.4) and (3.6) beginning at $t = 0$ with each of initial conditions in turn. The evolution of the three cases share many common features, and differ in several important respects. Their initial conditions and subsequent evolution are compared in Table 3.1. The cases have been designed to be similar in key respects evident from the table. These include their total lengths before and after retraction (128 Mm and 95 Mm respectively) and the total magnetic energy released: roughly 2×10^{10} ergs/Mx in every case. Differences between the runs result from the differing current sheets through which they retract. The differences are most readily understood by comparing common evolutionary moments. These moments are best illustrated using the run with uniform field, which serves as a kind of base case.

3.3.1 Evolution in a Uniform Field

The time evolution of the uniform case is shown at key evolutionary moments in Figure 3.6 using a format matching the equilibrium plots of Figure 3.5 (an animation is also available). The first event of note is the formation of retraction powered jets evident at 1 second, shown as blue solid lines in each panel. These jets are powered by the rotational discontinuities (RDs) at either of the bends moving down the legs (Longcope et al., 2009), evident in panel (a). They begin to form immediately and

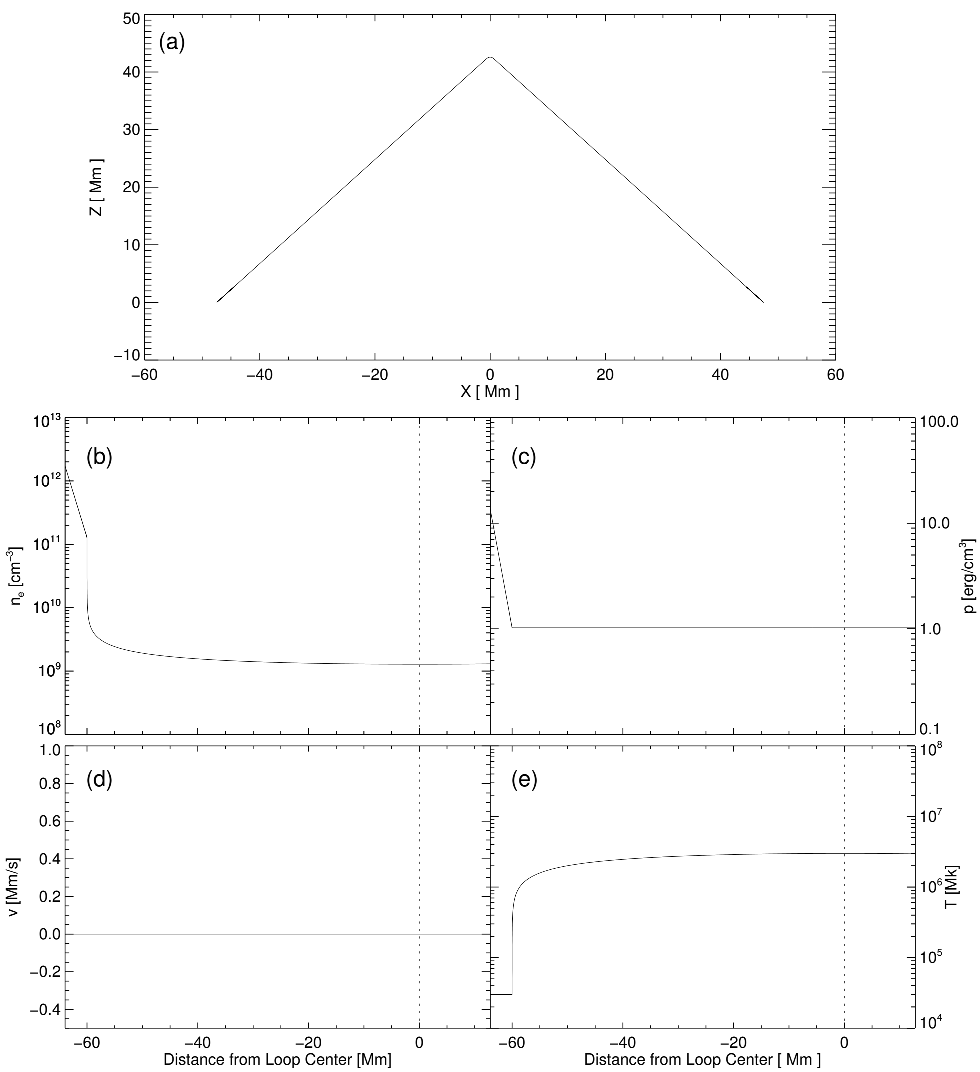

Figure 3.5: The initial conditions for the uniform case. (a): the flux tube's position in space. (b): the electron density as a function of tube length, zeroed at the center. (c): pressure. (d): shows the velocity along the tube. (e): temperature.

are well developed by 1 second. The flow is accelerated by the magnetic tension at the two bends. As the simulation advances, the jets reach a steady velocity in excess of 1 Mm/s. The mass that they move into the center of the tube creates a large increase of density there, as the material shocks when it collides with the counterpart jet from the other side. This shock is responsible for compression and bulk heating of the plasma. In this TFT model, the viscosity is responsible for converting the bulk kinetic energy to thermal energy.

Thermal conduction carries heat from the center of the tube outward, until it reaches the chromosphere. Thermal conduction is close to the free-streaming limit, bringing the flux limiter into play and producing the very steep fronts evident in the blue solid line (1 s) of Figure 3.6e. The conduction front reaches the chromosphere at $t = 14.3$ shown by green dash dot lines. Since the plot uses a length coordinate with zero at the mid-point, the left boundary appears to move inward as the length decreases during retraction. As the flux tube continues to retract the plasma jets continue to turn bulk motion into heat. Thermal conduction moves this heat down to the footpoints of the loop swiftly. As time advances from t=1.0 to 14.3, the front moves outward, it retains this sharp form until reaching the chromosphere. When the conduction front reaches the cooler dense material in the chromosphere, it heats the plasma there driving a sharp increase in the pressure. This pressure spike drives the material to expand marking the beginning of evaporation.

At the same time, $t = 14.3$ s, the flux tube reaches the edge of the current sheet, activating the restoring force placed at $z = z_0$. The center of the tube reaches the edge first as a result of being launched downward with the local Alfvén speed from the tube's apex. The initial condition of the tube is such that the apex has the lowest density and thus has the highest Alfvén velocity. This means the center will move down faster than any portion of the tube, and will reach the edge first. In this run the center reaches the current sheet edge at virtually the same time the conduction front reaches the chromosphere. As the flux tube encounters the edge of the current sheet it is then slowed by the underlying spring force. While this force attempts to remove the perpendicular velocity with minimal impact on the tube's internal dynamics, it does create some secondary viscous heating effects.

After being heated, the chromospheric plasma begins to evaporate and condense. Figure 3.6 shows the flux tube at 20 seconds in yellow solid lines and then at 30 seconds in red dashed lines. The increase in pressure in the chromosphere that was mentioned above forces the plasma outward both to the center and the foot. In this run, the initial evaporation is a slight pulse that occurs shortly after the conduction front arrives. This pulse can be seen in Figure 3.6 in panel (b) for density. This pulse clears out the flux tube, leaving a relative rarefaction behind it as it moves to the center. As more plasma becomes heated in the dense regions, conditions become favorable again for steady evaporation to begin. At 30 seconds, steady evaporation can be seen in the red lines in Figure 3.6. The pulse can also be seen having damped out somewhat, and followed by the steady state closer to the foot of the flux tube.

3.3.2 Evolution of the Expanding Case

The non-uniform magnetic field of the expanding case leads to evolution, shown at key times in Figure 3.7, differing in several respects from the uniform case. The blue solid lines show the flux tube at 1 second when the jets powered by the RDs work to pile material into the center of the flux tube. As before, the compression and shocks there heat the central material. The peak temperature depends on the parallel flow from the jets which in turn depends on the local Alfvén speed, $v_{\rm A}$, and the angle between the reconnecting field, $\Delta\theta_{\rm rx}$, as $v_{\|} = 2v_{\rm A}\sin^2(\Delta\theta_{\rm rx}/4)$ (Longcope et al., 2009). The expanding case has smaller field strength at the reconnection

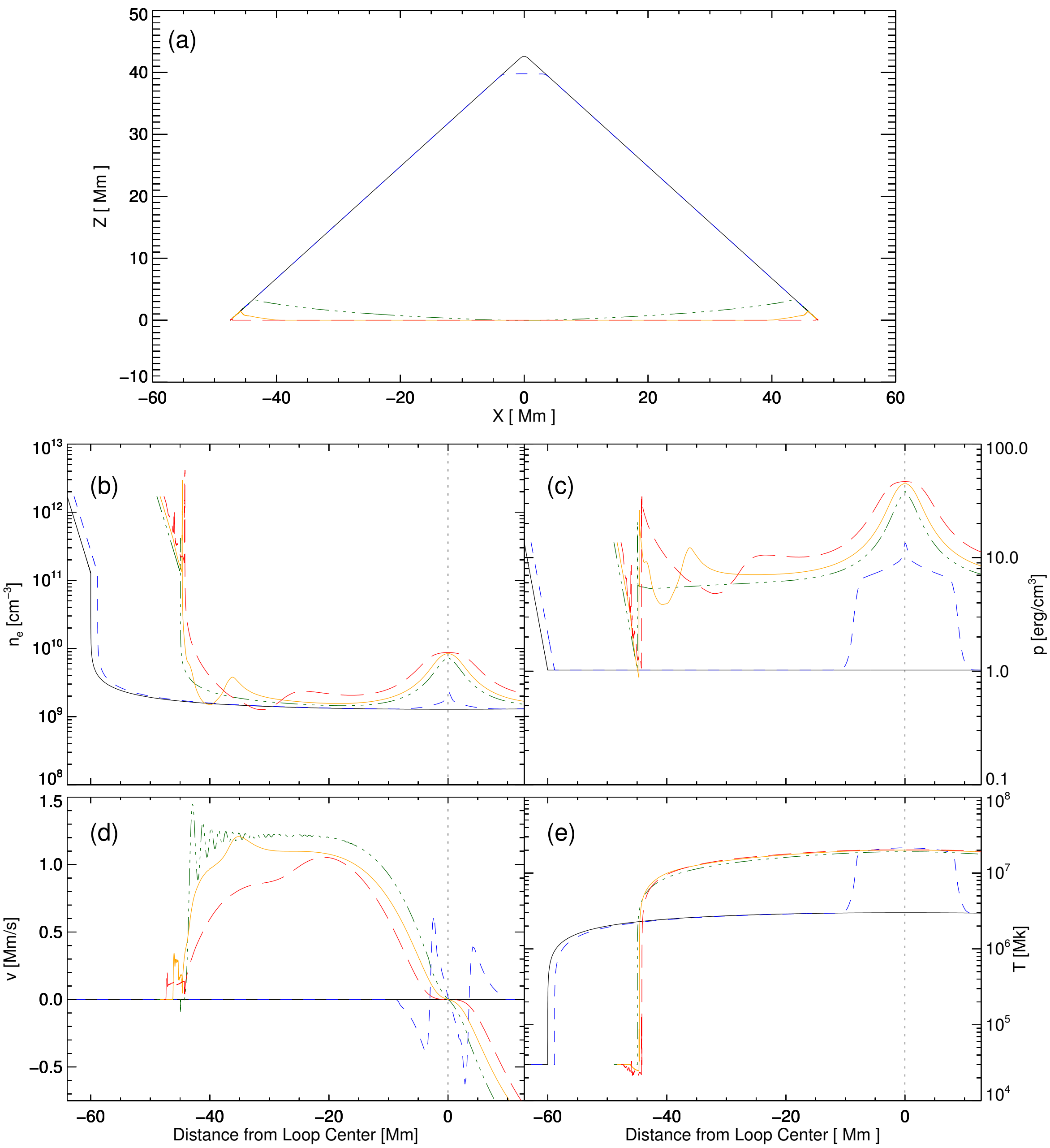

Figure 3.6: Evolution of the uniform case. (a): the flux tube's position in space. (b): the electron density as a function of tube length, zeroed at the center. (c): pressure. (d): velocity along the tube. (e): temperature. In each panel the color corresponds with the time, black solid is 0 seconds, blue dashed is 1.0 seconds, green dash-dot is 14.3 seconds, yellow solid is 20.0 seconds, and red dashed is 30.0 seconds. An animation is available. The video shows the entire 30 second sequence.

point ($B_0 = 56$ *vs.* 80 G), and thus a lower Alfvén speed there. The magnetic field angle at the reconnection point is, however, much greater in the expanding case, $\Delta\theta_{\rm rx} = 127°$ *vs.* 84°, leading to faster jets (see Figure 3.7d) and consequently higher peak temperature (34 MK *vs.* 25 MK) as shown in 3.7e. This higher temperature drives the conduction fronts faster so by 8.1 seconds, shown green dash-dot, they have reached the chromosphere while the tube is still retracting. The slower fronts of the uniform case reached the chromosphere at roughly the same time the tube reached the end of the current sheet.

The tube's encounter with the current sheet bottom, shown at 10.4 seconds in solid yellow, is similar to the encounter observed in the uniform case. The tube's mid-point was accelerated to the local vertical component of the Alfvén speed which, as in the uniform case, is the largest at the mid-point. The initial downward velocity, $v_z = -v_{\rm A}\sin(\Delta\theta_{\rm rx}/2)$ (Longcope et al., 2009), is comparable in the two cases as their differing values of $v_{\rm A}$ and $\Delta\theta_{\rm rx}$ tend to offset one another. Reconnection occurs lower in the expanding case (see Figure 3.4a), so the mid-point reaches the bottom slightly earlier than in the uniform case (10.4 s *vs.* 14.3 s). From the initial contact at the mid-point, the tube's encounter with the bottom spreads outward as it did in the uniform case.

3.3.3 Evolution of the Contracting Case

The non-uniform field of the contracting case leads to evolution different from both the uniform and the contracting cases, evident in the key times shown in Figure 3.8. The jets have once again begun by 1 second (blue dashed lines) but are much weaker than in the other cases. This is a result of reconnection at a point of low field strength and thus low Alfvén speed. The weaker jets produce a lower central temperature, at least initially. The thermal conduction from this cooler center does

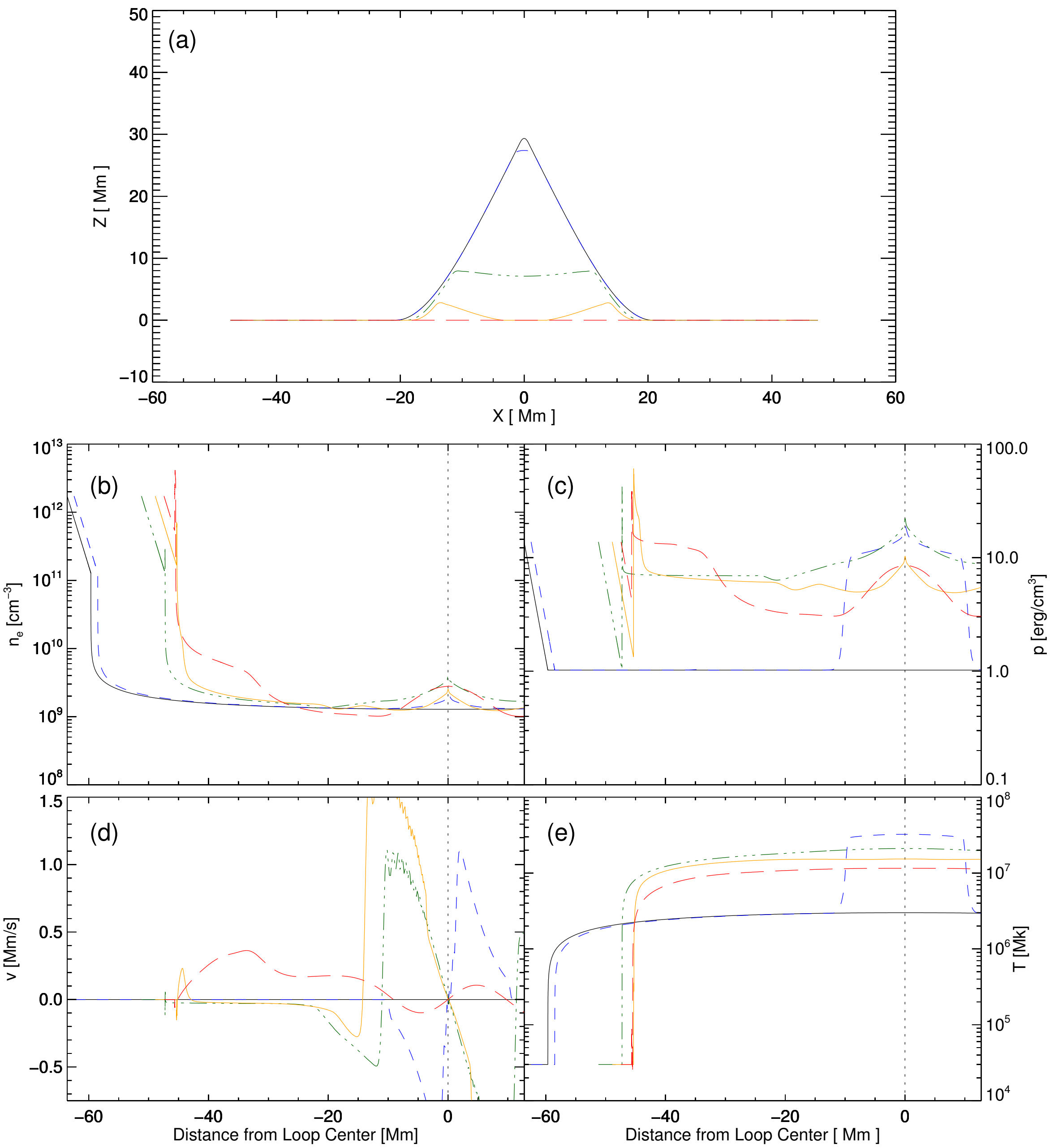

Figure 3.7: Evolution of the expanding case. (a): the flux tube's position in space. (b): the electron density as a function of tube length, zeroed at the center. (c): pressure. (d): velocity along the tube. (e): temperature. In each panel the color corresponds to the time, black solid is 0 seconds, blue dashed is 1.0 seconds, green dash-dot is 8.1 seconds, yellow solid is 10.4 seconds, and red dashed is 30.0 seconds An animation is available. The video shows the entire 30 second sequence.

not approach the free-streaming limit, so the heat fronts are shallower than in the other two cases. The conduction front also moves more slowly so it has not yet reached the chromosphere when the retraction reaches the current sheet edge at 13 seconds (green dash-dot lines).

The retracting tube of the contracting case encounters the bottom of the current sheet in a manner entirely different from the encounter of the other two cases. The RDs move at the local Alfvén speed, which increases downward in the contracting case. The outer corners therefore move downward faster than the middle, making the the retracting segment concave downward, as clear from the green curve in Figure 3.8a. The corners (i.e. the RDs) therefore reach the base of the current sheet ahead of the mid-point. The mid-point hits the bottom last, and the thermal conduction front reaches the chromosphere shortly afterward, at 16.3 seconds and shown in solid yellow. The last event shown is at 30 seconds and in red dashed lines, and like the previous cases, highlights the development of steady evaporation. As a result of starting in the weakest field, this case seems to be the weakest in these time steps.

3.4 Run Results and Analysis

3.4.1 Energy Evolution

Global properties of the runs, such as their energy evolution shown in Figure 3.9, have common elements but also differ in key respects. To more clearly show gains and losses the plot shows the energies less their initial value. Different colors show different forms of energy, namely total energy (black), magnetic energy (violet), thermal energy (red), total kinetic energy (dark green), and that portion of that kinetic energy directed along the flux tube (light green). All energies are calculated per unit flux (i.e. ergs/Mx), but can be multiplied by the flux of a single tube, or an entire flare, to obtain a more familiar value in ergs.

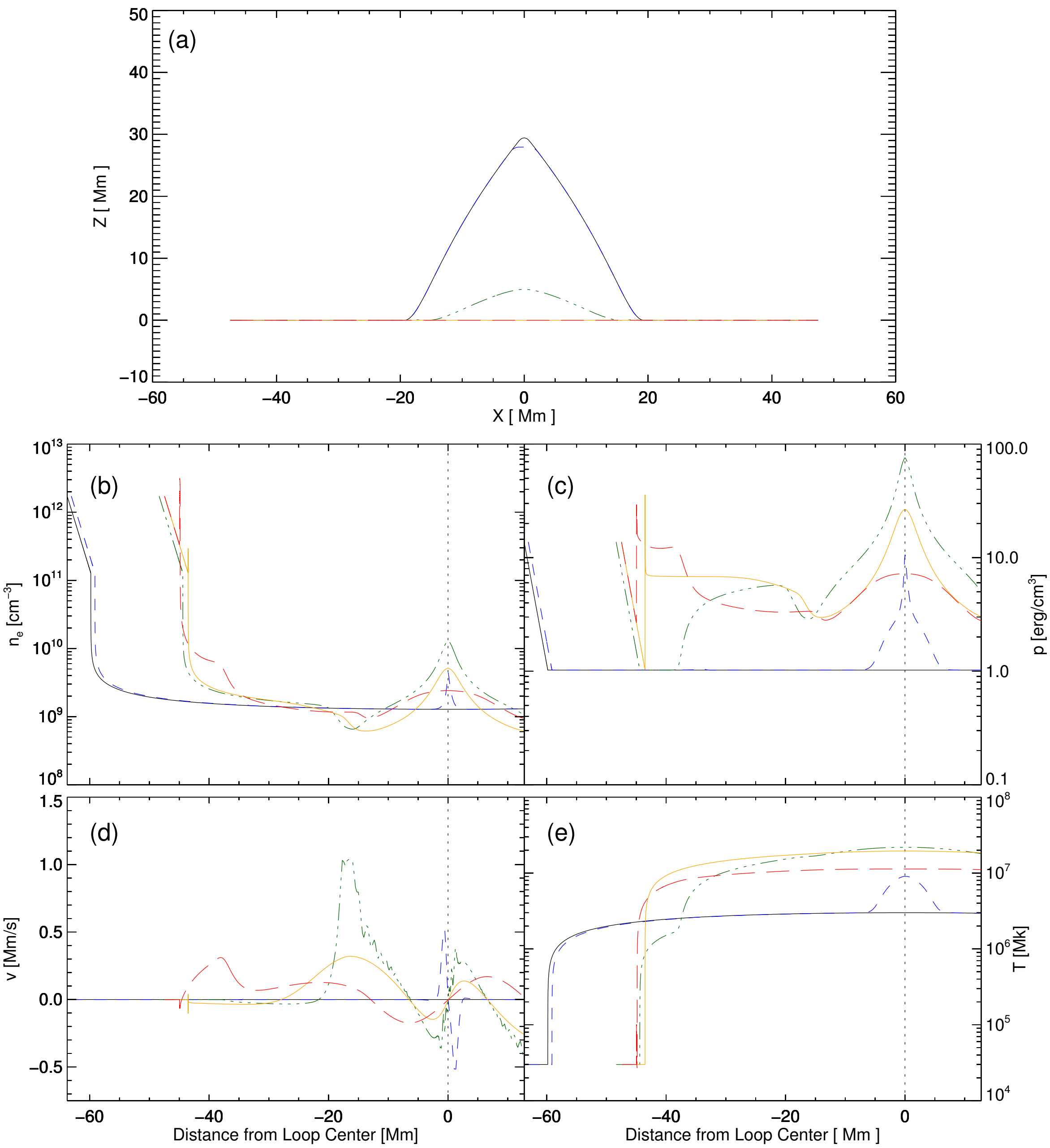

Figure 3.8: Evolution of the contracting case. (a): the flux tube's position in space. (b): the electron density as a function of tube length, zeroed at the center. (c): pressure. (d): velocity along the tube. (e): temperature. In each panel the color corresponds to the time, black solid is 0.0 seconds, blue dashed is 1.0 seconds, green dash-dot is 13.0 seconds, yellow solid is 16.3 seconds and red dashed is 30.0 seconds. An animation is available. The video shows the entire 30 second sequence.

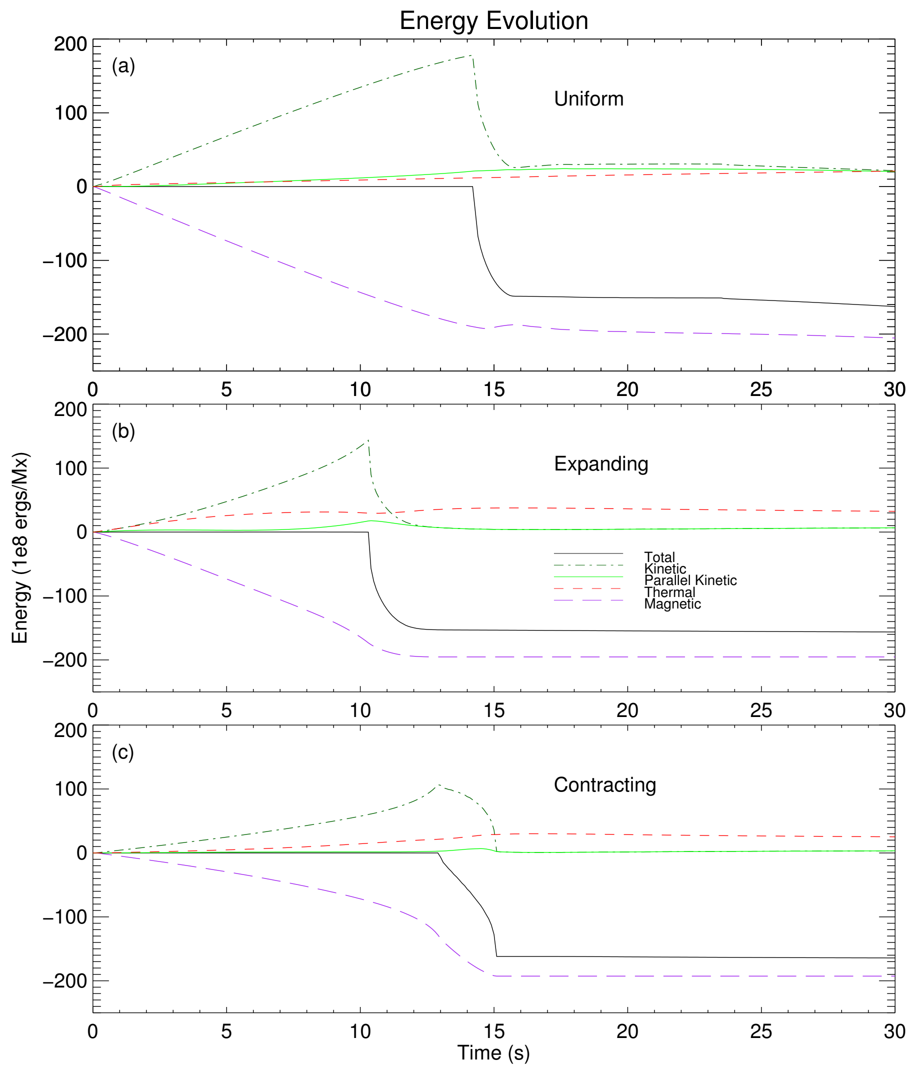

Figure 3.9: Time history of various energies in units of 10^8 erg/Mx, for (a) the uniform case, (b) the expanding case, and (c) the contracting case. In each panel the energies have been offset by their initial values to clearly show gain and loss. Solid black is the total energy, red dashed the thermal, dark green dash-dot the total kinetic, solid light green the parallel kinetic and violet dashed is the magnetic energy.

Each case shows an immediate drop in magnetic energy accompanied by a matching gain in total kinetic energy. Magnetic tension works to pull a flux tube down to the bottom of the current sheet. In the uniform case that is the only force acting on the flux tube. For the expanding case, the tube is also being squeezed out of the region of high field by the magnetic pressure term – the final term in Equation (3.4). For the contracting case, this pressure works against the retraction as it moves into higher field regions. The result of this is that in the expanding case, the magnetic pressure and tension work in the same direction, speeding up the retraction process, while in the contracting case the pressure partly offsets the tension, slowing the retraction.

While most of the kinetic energy in each simulation is in motion perpendicular to the axis, a smaller fraction is in flows directed along the tube. This latter portion is the energy of the parallel jets responsible for the majority of the heating, ultimately leading to the increase in overall thermal energy.

The instant the flux tube reaches the edge of the current sheet appears as the sharp drop in both total energy and the total kinetic energy. At this instant the *ad hoc* force comes into play, doing negative external work on the tube and decreasing its energy. Since this force takes the place of upward force from the underlying arcade, the energy would in reality go into its compression, possibly radiating as fast magnetosonic waves. In any event, the energy does not remain on the flux tube. The parallel motions will, however, remain on the tube and are unlikely to couple strongly to the compressive, perpendicular motions. In the uniform case, in particular, the parallel kinetic energy (light green) shows little effect from the damped spring at the end of retraction.

Each run shows similar features though the magnitude and timing of these features differs between the cases. While the uniform case reaches higher temperatures than the contracting case, it has less mass (per unit flux) to heat, so its thermal energy (per flux) remains lower. The same effect results in the other two runs losing their thermal energy near the end of the simulation as the extra mass leads to more effective radiation, allowing them to cool more rapidly. Finally, the uniform and expanding cases have a steep initial drop in the total and kinetic energies followed by a slower loss. In contrast, the contracting case initially loses both slowly and then experiences a steep loss at the end. The difference is a result of the flux tube hitting the edge of the current sheet with the middle first in the first two and the corners first for the contracting case. The results of Figure 3.9 further confirms the similar characteristics of the runs notes before in Table 3.1.

3.4.2 Comparison of Observables

Several key differences between the cases are evident when temperature is plotted versus both space and time as a stack, shown in Figure 3.10. These were created by taking the temperature as a function of length along each loop, using the mid-point as zero. Each successive time step is appended to create a 2-d map of the temperature, using color, versus both space (vertically) and time (horizontally). In each of the three panels the thermal conduction front appears as a red wedge with a vertex at the time and place of reconnection: $(t, \ell) = (0, 0)$. The green region below this wedge is the 3 MK coronal plasma of the initial loop. Below this is a black wedge along the lower axis and whose upper edge is the left boundary of the simulation. The boundary point is fixed in space but appears to move in the stack plot as an artifact of our using integrated length as the spatial coordinate. The tube's retraction decreases the length separating the mid-point, $\ell = 0$, from the fixed boundary point. This has the effect of changing the length coordinate at which this stationary boundary appears.

There are notable differences in the temperature evolutions of the three cases.

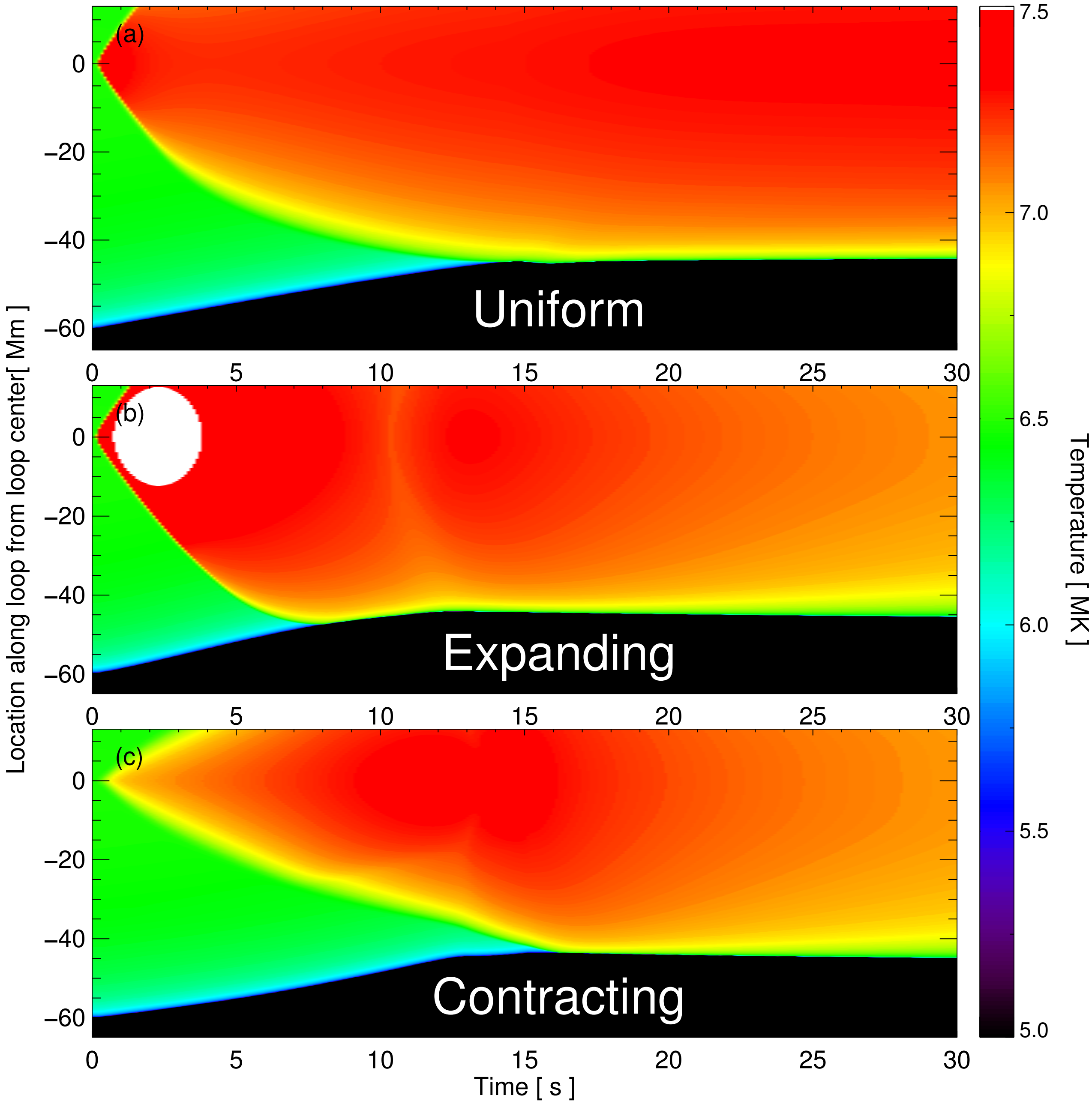

Figure 3.10: Temperature stack plots for each of the three runs: (a) the uniform case, (b) the expanding case, and (c) the contracting case. Each panel shows the time evolution of the loop temperature from $10^{5.0}$ K to $10^{7.5}$ K, as shown by the color bar on the right. Temperatures above $10^{7.5}$ K appear white, and regions outside the flux tube appear black.

In the uniform case, the highest temperature is created very quickly, 0.3 seconds into the simulation, as shown by the change from green to red along the upper horizontal $\ell = 0$ line in Figure 3.10a; this represents temperature increasing from the starting 3 MK to just over 25 MK. This case has the most uniform rate of magnetic energy release, and as such the most uniform conversion of that released energy into kinetic and thermal forms. For that relatively constant rate, the most effective temperature increase is the beginning, when the plasma in the middle of the flux tube is still rarefied. Thereafter the peak temperature drops steadily. This contrasts with the expanding case that reaches its maximum temperature 1.8 seconds after it begins retracting. The color table saturates at $T = 10^{7.5} = 32$ MK, so the peak appears here as a white region in panel (b). The expanding case retracts from the strongest field at the beginning of the simulation. This allows for a high rate of conversion from magnetic to kinetic energy compared with later times. With more mass in the tube, the overall partition of kinetic energy is smaller. More of that kinetic energy was directed along the tube in the early time of the run allowing for stronger interactions between the jets resulting in a higher temperature.

Both of these differ radically from the temperature evolution of the contracting case shown in Figure 3.10c. With the retraction starting in a low field strength, the contacting case can not build strong jets to start with. This results in a relatively cool loop top, and a slow conduction front evident from the shallower slope of that front in Figure 3.10c. When the retraction does reach strong field regions, and can begin to generate more heat, the central region of the flux tube has been insulated from cooler coronal plasma by the initial smaller heat generation. While the peak temperature in this case is lower, there is, due to this insulating effect, still a high temperature central component that would otherwise have been diminished by spreading throughout the full loop length. As a result we can clearly say that the temperature evolution in each case has been clearly influenced by the current sheet profile.

Retracting through different field profiles results in a dramatically different evolution of the central density. Density stack plots for the three runs displayed in Figure 3.11 are constructed in the same manner as the temperature stack plots of Figure 3.10. These show the same black wedge along the left boundary, but no signature of the conduction fronts since those primarily affect temperature. The central plug of high density, compressed by the RD-powered jets, appears as a lighter-blue horizontal band near the top at $\ell = 0$. This material is dense and hot and so is accompanied by a rise in central pressure which seeks to expand the plug. At the same time more material is constantly being added to the central plug by the jets. The result is that while the plug does expand (the horizontal bands are slightly triangular), the central high pressure is preserved even past the end of retraction. Only at later times does the central pressure begin to drive the plug into the surrounding plasma. Confirmation of this can be seen in panel (c) of Figs. 3.6-3.8 displaying the pressure.

Central plug compression occurs in the expanding case, panel (b), but with a slight complication not found in the uniform case. In the expanding case, the flux tube retracts into weaker field which increases its cross sectional area. This means the inward jets are adding mass to a central region of increasing volume, greatly offsetting any possible density increase. Were the jets absent, the increasing area would drive down the tube's density. This does occur in the legs surrounding the central region, resulting in relative voids which appear as darker blue regions in Figure 3.11b.

The contracting case exhibits behavior opposite to this. The jets add material to a central region whose cross section is diminishing as retraction moves the tube into increasing field, i.e. decreasing volume. The central plug is therefore squeezed from all sides, producing a relatively high density, evident as a horizontal band of lighter shade than either other case. This omnidirectional compression lasts only until the central

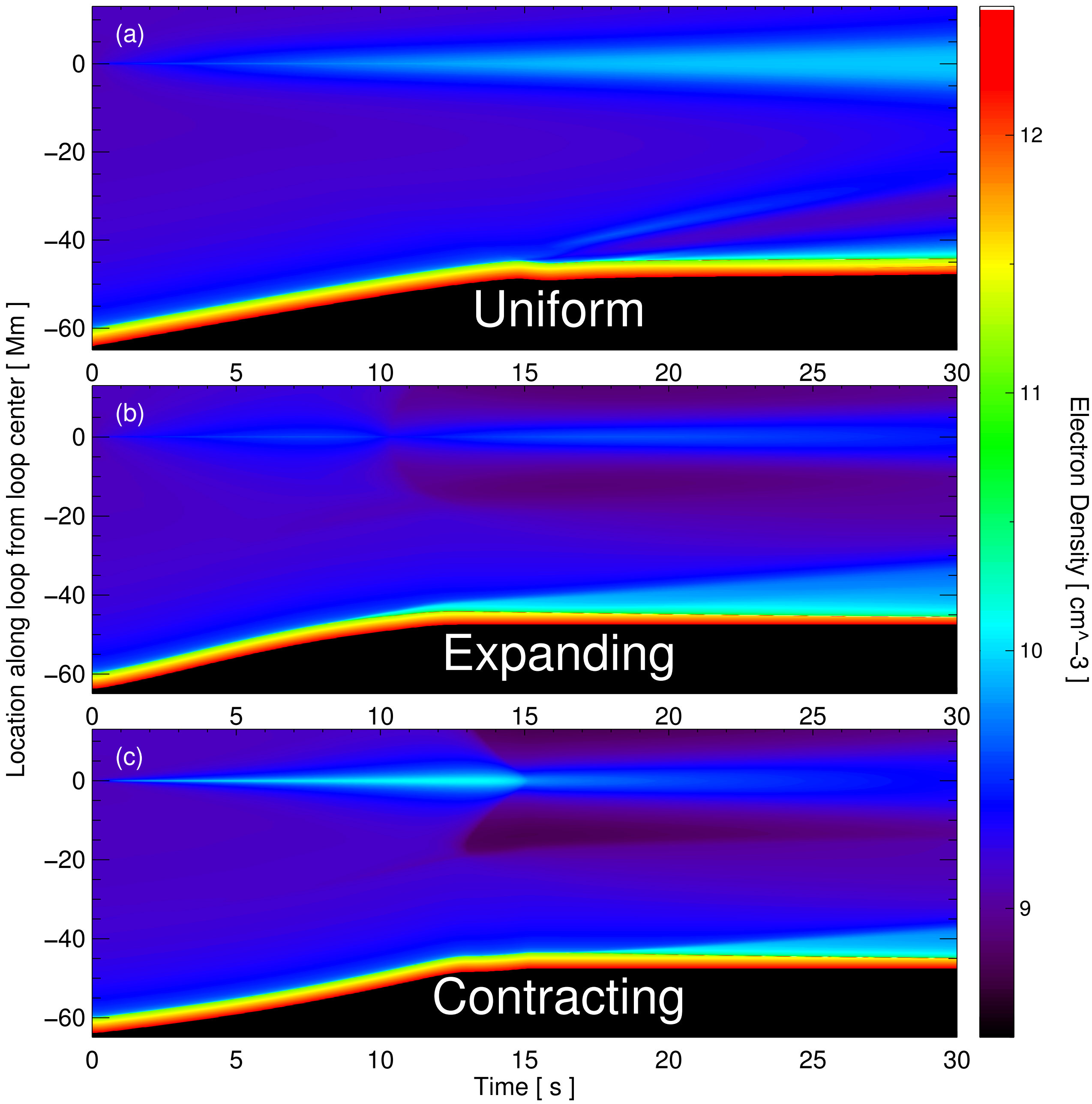

Figure 3.11: Electron Density stack plots for each for (a) the uniform case, (b) the expanding case, and (c) the contracting case. Each panel shows the time evolution of half the loop from $10^{8.5}\,\mathrm{cm}^{-3}$ to $10^{12.0}\,\mathrm{cm}^{-3}$ in electron density, as shown by the color bar on the right.

region has pulled through the maximum field, after which it encounters weakening field. At this point the, we see the appearance of relative voids in the areas adjacent to the central region.

Differences in both temperature and density evolution combine to produce differing evolutions of differential emission measure (DEM). Spatially integrated, time-resolved DEMs of each run are plotted in Figure 3.12. The vertical axis of each plot is the logarithm of temperature, the horizontal axis is time, and color represents $\log(DEM)$ from blue to red. Four notable features are present in each of the three cases. First is the darkening, or dimming (i.e. blue region), beginning $t = 0$ at roughly $T = 10^{6.5} = 3$ MK and sweeping down to $T = 10^{4.5} = 30,000$ K. This shows coronal plasma heated from its initial temperatures to tens of MK, leaving a dearth of emission measure in the ranges at and below 3 MK. The dimming sweeps down over time as the thermal conduction front moves to decreasing temperatures in the loop's legs. The progression of this sweep differs slightly between runs according to the rate of heating and speed of the conduction front moving down the legs.

The next important feature is the enhanced emission measure (red and saturated white) in the cooler bands, below $T = 10^{6.0} = 1$ MK, after the conduction front has reached the chromosphere. This feature comes about from the increased pressure in the chromosphere leading to compression at the leading edge of the downward moving condensation front. This enhancement in DEM at lower temperatures is paired with the third important feature, the enhanced emission in the megakelvin range at roughly the same time. This appears as an upward green and orange regions sloping upward and then persisting in time. It reflects the material heated to coronal temperatures by the conduction front – material evaporated into the corona. It is noteworthy that conduction cannot create temperatures exceeding the loop-top source's peak temperature.

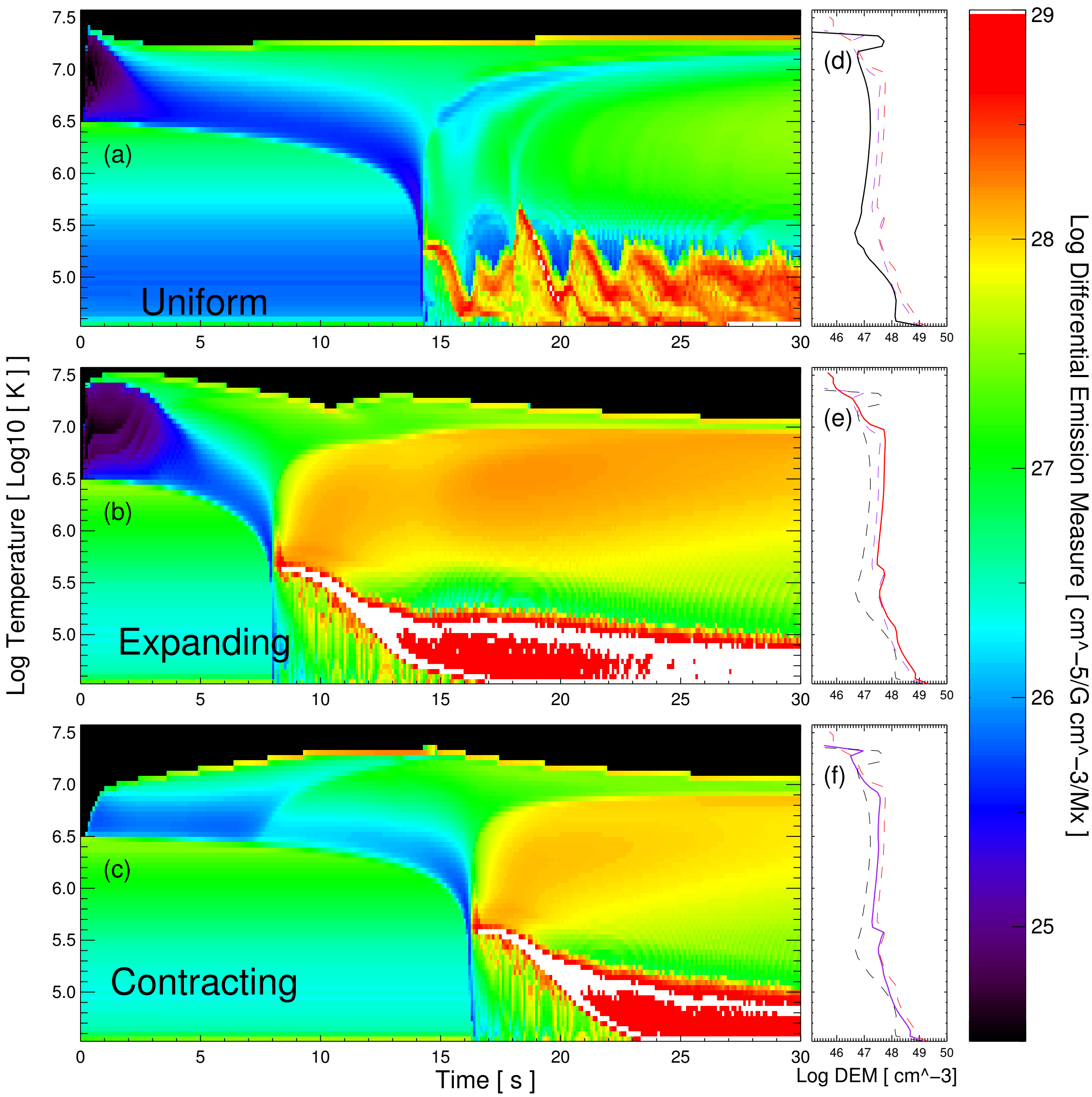

Figure 3.12: Differential Emission Measures (DEMs) per Log kelvin for (a,d) the uniform case, (b,e) the expanding case, and (c,f) the contracting case. The left column (a–c) shows time-resolved DEMs using a color scale from $10^{24}\,\mathrm{cm}^{-5}/\mathrm{G}$ (violet) to $10^{29}\,\mathrm{cm}^{-5}/\mathrm{G}$ (red) against time on the horizontal axis and $\log(T)$ on the vertical axis. The right column (d–f) plots as a solid line the time-integrated version of the DEM to its left using the same vertical temperature axis . The other two curves are plotted dashed for reference. The time-integral is multiplied by 10^{18} Mx/s to obtain a full-flare DEM with units of cm^{-3}.

The final feature of note is the behavior of the hottest emission. Both the uniform and expanding case show a "finger" of green at $T \simeq 10^{7.3} = 20$ MK from the beginning ($t = 0$). In the expanding case the upper green edge slopes more gradually upward, but persists longer than the other cases. In the uniform case the temperature peaks quickly but in such a rarefied region that the emission measure of the source is relatively low, and dies off rapidly as conduction moves the heat throughout the rest of the tube. The continuing action of the jets however piles up material and continues to heat it, and as a result there is a bounce back with slightly cooler material, but appearing much brighter. The expanding case shows a similar type of behavior. At first the jets produce the peak temperature, and in this case it is bright emission. The thermal energy is quickly spread through the flux tube and this emission is lost. The continuing action of the jets work to heat the central region and slightly cooler material brightens in the central plug again. It cools more quickly than in the uniform case. The behavior in the contracting case is, once again, opposite to this. Owing to its more slowly building heat, we see a gradual rise to the peak emission. It then cools like the expanding case and experiences no bounce back to a slightly cooler bright source.

The differences described above lead to clear and potentially observable differences in time-integrated DEM, plotted along the right column of Figure 3.12 (d–f). The curves show the integral of the time-resolved DEM immediately to the left, along the same vertical temperature axis. For simpler comparison each DEM is multiplied by a typical reconnection rate of 10^{18} Mx/s to get a volumetric DEM of the run as a whole (Jing et al., 2005; Longcope et al., 2010; Kazachenko et al., 2017). Since a flare consists of numerous independently contracting loops, a time-integrated observation will resemble this plot more than a slice of the time-resolved DEM (Longcope et al., 2018). For ready comparison, each panel over-plots the integrated DEM from all three cases using the same colors as Figure 3.4: black for the uniform, red for the expanding and violet for the contracting case. The curve matching the panel to its left is plotted solid, and the other two dashed. It is immediately clear that the uniform case carries significantly less emission in the megakelvin range for reasons previously discussed. The expanding case has more megakelvin emission than the other two, as a result of the strong conduction front and the aggressive evaporation.

Significantly, the contracting and uniform runs both show DEM peaks in the hottest range, while the expanding case does not. While that run does experience temperatures that high, even higher, it is brief enough and lacks the density necessary produce DEM comparable to the other two cases. It is notable that the contracting case produces high temperature later than the contracting case, but also that it persists longer thereby producing the observed high temperature peak.

3.5 Discussion

The foregoing analysis has shown observable differences arising from reconnection at different locations within different kinds of global current sheets. We investigated three distinct cases: reconnection in a uniform sheet, reconnection above the pinch point, and reconnection at the pinch point. To do so we created a simple 2.5d current sheet from which we then created the two non-uniform reconnection scenarios. Each flux tube was initialized in a similar way, with the current sheet field being the principal difference between cases. The TFT was used to find the post-reconnection time evolution in each case. The most notable difference between the cases was that reconnection above the pinch point, called the contracting case, exhibited a relatively long-lasting, high-density plug of super-hot material (i.e. $T \sim 20$ MK). This was evident in both the density plot, and as a peak in the time-integrated DEM.

Some observations have found evidence of super-hot hard X-ray sources at or above the flare loop top (Kosugi et al., 1994; Veronig et al., 2006; Caspi & Lin, 2010). The chief challenge posed by these observations is to enhance the density in a high-temperature plasma. It has been proposed that this can be achieved through the confining parallel jets supplied by the RDs (Longcope et al., 2010; Longcope et al., 2016). Here we have found that this parallel compression is augmented by lateral compression in cases where reconnection occurs above the point of peak field strength in the current sheet. In this sense, observations of super-hot loop-top sources appear to support that particular site for localized flare reconnection.

Other explanations have been proposed to explain above-the-loops hard X-rays sources. Some observers have invoked a population of non-thermal electrons (Sui et al., 2004) which could not be described using a fluid model like ours. Other models create super-hot coronal sources in different ways, such as through successive reconnection as in Karlický & Bárta (2011), fast-mode termination shocks (Aurass et al., 2002; Shen et al., 2018), or instabilities driving complex interactions (Fang et al., 2016). These effects stand beyond the scope our strictly fluid model to explore.

Reconnection under the contracting scenario has been proposed in some previous flare investigations. Longcope et al. (2018) found evidence for it in EUV images of the plasma sheet above the limb flare on 10 Sep 2017. They used a similar TFT simulation, *via* PREFT, to show that the inflow jets combined with lateral flux tube compression could enhance the density almost 20-fold — just enough to match the observations. Retraction into strengthening field is also invoked as a mechanism for accelerating non-thermal particles in the so-called collapsing trap model (Levine, 1974; Somov & Kosugi, 1997; Karlický & Kosugi, 2004). Particles experience an energy gain scaling with the field-strength increase. In the contracting case we modeled the field strength increase was less than 1.5 (from $\sim 40 \rightarrow 56$ G), so we would expect rather modest energy gains at best. But our model neglects non-thermal populations since it is focused exclusively on the bulk plasma dynamics. On the other hand, collapsing trap models often neglect the thermal plasma, and almost never include the kinds of self-consistent density and temperature increases that we find will occur within the collapsing trap. A study combining these two elements remains a task for future investigation.

The TFT model provided us an expedient means to explore the differences in reconnection geometry, albeit with some loss of fidelity due to its approximations. Because it treats the post-reconnection evolution in an ideal current sheet, the TFT model includes no electrical resistivity. While some diffusive process is an essential part of the reconnection process, this is thought to play little role in the global exterior region where energy release occurs. It is this non-diffusive, post-reconnection energy release that TFT seeks to model. The TFT tacitly neglects any possible interaction with other reconnected flux or with the plasma around itself. One consequence of this neglect is that reconnected flux retracts at speeds approaching the local Alfvén speed. This is, however, common to many theoretical reconnection models: they generally predict reconnection outflow at Alfvénic speeds (Petschek, 1964; Soward, 1982). Unfortunately, our theoretical model falls into this same category.

The different cases were affected differently by the profile of the current sheet magnetic field. The timing of each flux tube's retraction differed, with the expanding case being the fastest as it was pushed downward by magnetic pressure. As the retraction converted magnetic energy into heat through jets and viscous interactions, the expanding case experienced the highest temperature, while the contracting case had the lowest, due to its low conversion rate. The difference in temperature led to the difference in the thermal conduction front, with the expanding case having the fastest moving front. The magnetic field also changed the density of each run by compressing or expanding each tube. The contracting case experienced the highest density as the field squeezed the tube while the jets piled in material.

To illustrate the observable consequences we constructed time-resolved, and time-integrated differential emission measures for each tube over the duration of the simulation. Each run showed similar features, but with different emphasis as a result of the different dynamics. While the expanding run showed the highest temperatures, it did so in relatively rarefied material which produced low emission. The contracting run, on the other hand, reached its peak temperature when it had accumulated a plug of dense material, leading to higher emission measure. Overall the expanding run did not show sustained emission in tens of megakelvin ranges, where we consistently see emission in the extreme ultraviolet. The other two cases, despite lower temperatures, did produce an peak in emission in the same range.

An expanding flux tube type scenario generates peak heat up front when it does not have a large density results in emission dropping off in the higher temperatures. This contrasts with the contracting and uniform cases that both show an excess of emission at the higher temperatures instead of decreasing smoothly. While increasing the field strength or increasing the energy release may shift the peak around, or shift the decay in emissions higher, it is unlikely to change the result of the DEM. In the future, we would like to expand on this work by considering a more varied parameter space to verify that this relationship holds for more varied current sheets.

This work was supported partly by grant NNX16AH04G from NASA's Heliophysics Supporting Research (HSR) program.

	Uniform	Expanding	Contracting
T_{min} (MK)	0.03	0.03	0.03
T_{max} (MK)	3.0	3.0	3.0
Min n_e (Log10(cm^{-3}))	9.1	9.1	9.1
Peak Magnetic Field Strength (gauss)	80	55.9	55.9
$\Delta\theta_{\mathrm{rx}}$ - The Field angle at reconnection site	84.2°	126.8°	103.6°
Maximum Initial Plasma β	0.002	0.021	0.021
Maximum Plasma β	0.621	3.38	1.07
Initial Length (Mm)	127.9	127.2	127.5
Final Length (Mm)	94.9	94.9	94.9
Total Energy Loss (10^8erg/Mx)	164.64	158.28	164.22
Magnetic Energy Loss (10^8erg/Mx)	205.26	195.33	192.72
Peak temp (MK)	25.17	33.61	22.77
Time of peak temp (seconds)	0.3	1.8	14.7
Time to hit bottom (seconds)	14.3 (center)	10.4 (center)	13.0 (sides)
Time to finish retraction (seconds)	27.4 (1% of final length)	12.5 (sides)	15.1 (center)

Table 3.1: Collection of initial conditions and summarized results for each case.

CHAPTER FOUR

FLUX TUBE INTERACTIONS AS A CAUSE FOR SUB-ALFVÉNIC RECONNECTION OUTFLOW

Contribution of Authors and Co-Authors

Manuscript in Chapter 4

Author: John Unverferth

Contributions: Modified framework and ran the study. Wrote manuscript.

Co–Author: Dana Longcope

Contributions: Helped to guide study. Commented on analysis and drafts of manuscript.

Manuscript Information

John Unverferth and Dana Longcope

The Astrophysical Journal

Status of Manuscript:
_X_ Prepared for submission to a peer-reviewed journal
____ Officially submitted to a peer-reviewed journal
____ Accepted by a peer-reviewed journal
____ Published in a peer-reviewed journal

ABSTRACT

Observations of reconnection outflows of the September 10th 2017 X 8.2 (SOL2017-09-10T15:35:00) flare place them at 300 km/s to 700 km/s. They occur at speeds that are below the expected Alfvén speed in the current sheet they move through. This contrasts with reconnection models that predict Alfvénic outflows. In this work, we attempt to reconcile this by using a thin flux tube model with drag. This is modeled as aerodynamic drag proportional to the square of velocity. We use a simulation of a retracting flux tube to create a synthetic current sheet. In this sheet we see that slower retractions increase the brightness of emission from the synthetic current sheet, and lower temperatures. Increasing the field strength raises the temperature of the current sheet, at the expense of emission measure, leading to a dimmer current sheet.

4.1 Introduction

Retraction of flux from the reconnection site in flares is observed to occur at speeds much slower than most theory predicts. Models of fast reconnection, like that expected in flares, predict outflow from the reconnection site moving at the Alfvén speed (Vasyliunas, 1975; Baty et al., 2006; Forbes et al., 2013). This is generally not seen in observations, where potential signatures of downflows happen at hundreds of km/s (Warren et al., 2011) while the Alfvén speed is certainly in the thousands of km/s.

The X8.2 class flare on September 10, 2017 (SOL2017-09-10T15:35:00) has been studied in depth by many authors and groups (Warren et al., 2018; Longcope et al., 2018; Karlický et al., 2020; Gary et al., 2018). This is partly due to its large scale and to the positioning and geometry of the flare, providing an excellent view of an extended plasma sheet above the flare arcade. Observations by Longcope et al. (2018) among others show downflowing features with median speeds at several hundreds of km/s, believed to be outflow from a higher reconnection point.

Observations of Supra-Arcade Downflows (SADs) and Supra-Arcade Downflowing Loops SADLs provide evidence for this discrepancy (McKenzie & Savage, 2009; Savage et al., 2010). SADs in flares retract at less than Alfvénic speeds and are thought by some to be retracting flux (McKenzie & Hudson, 1999) or the wake of the retracting flux (Savage et al., 2012). The speed of SADs is consistent with the downflow speeds seen by Longcope et al. (2018) and reinforces the connection between SAD and reconnected flux. The passage of flux through the sheet disturbs material behind it leaving a wake.

Observations of the September 10th event made with the Expanded Owens Valley Solar Array (EOVSA) (Gary, 2016) and The Reuven Ramaty High-Energy Solar Spectroscopic Imager (RHESSI) (Lin et al., 2002) show signatures of a reconnection site near the loop top and of two signals leaving this source, one fast and one slow (Yu et al., 2020). Of particular note is the 10-second lag time between the emission at loop top and the emission in the loop leg. This represents a potentially fast, perhaps Alfvénic, transit of some emitting source from the loop top down the loop leg. The slower signature observed in the same event is consistent with SADs moving at several 100 km/s (Longcope et al., 2018; Yu et al., 2020).

A model of both Alfvénic and much slower signatures of retraction may provide an explanation of the low-speed outflows as consistent with magnetic reconnection. The Thin Flux Tube (TFT) model attempts to model flare dynamics on a flare loop scale. Previous works with the TFT in solar flares have shown the presence of rotational discontinuities and the evolution of the flux tube as it retracts from the reconnection site (Longcope & Klimchuk, 2015; Longcope et al., 2018; Unverferth & Longcope, 2020). These works had the retraction and the rotational discontinuities both moving at significant fractions of the Alfvén speed.

Observations of the September 10th flare current sheet (Longcope et al., 2018; Gary et al., 2018) show a magnetic field that decreased in magnitude with height. This serves to further boost the emission measure in previous TFT models of this event, but still fell short of the observed emission measure. The temperatures and magnetic fields are inferred from observations while the emission measure is more directly linked, providing a stronger constraint to models.

This work will introduce, for the first time, a drag force to model flux tube retraction. This is an attempt to reconcile the Petschek style reconnection Alfvénic outflows, with the slower motions typically observed. Section two explains the Thin

Flux Tube model that we use to evolve our flux tubes and the drag force we use. We also explore the evolution of the single flux tube here. Section three uses this flux tube to construct a synthetic plasma sheet that contains the flare current sheet and finds trends based on this. Section four summarizes our findings and discusses potential implications.

4.2 The Thin Flux Tube Model

To investigate how interaction with the surrounding current sheet might influence the observations of a flare loop, we turn to the thin flux tube (TFT) model, first used by Spruit (1981b). This method involves treating the flux tube as an isolated bundle of flux, that can move and evolve against a static background. The background does not change in time, but can freely vary in space. This model has been used as a bridge between more complex fully 3-Dimensional models, and simple 1 and 2-Dimensional models (Longcope et al., 2010; Longcope & Klimchuk, 2015). It provides more self consistent dynamics than gas in a rigid tube, while not requiring such large computations as a fully 3-D volume over the domain. This simplicity over a single element in the 3-Dimensional space allows for higher resolution along the single element, an incredibly important feature for flare modeling (Longcope & Klimchuk, 2015).

In this work, we solve the TFT model with the Post Reconnection Evolution of a Flux Tube (PREFT) code. This code works to advance the TFT version of the MHD equations through time. PREFT is a Lagrangian code keeping the fluid in cells, which move according to the momentum equation,

$$\frac{D\boldsymbol{v}}{Dt} = \frac{1}{\rho}\left(\frac{B^2}{4\pi} - p\right)\frac{\partial\hat{\boldsymbol{b}}}{\partial\ell} - \frac{1}{\rho}\frac{\partial p}{\partial\ell}\hat{\boldsymbol{b}} + \frac{B}{\rho}\frac{\partial}{\partial\ell}\left(\frac{\tilde{\eta}}{B}\hat{\boldsymbol{b}}\hat{\boldsymbol{b}}\cdot\frac{\partial\boldsymbol{v}}{\partial\ell}\right)$$

$$+\frac{1}{\rho}\left(1+\frac{4\pi p}{B^2}\right)\nabla_\perp\left(\frac{B^2}{8\pi}\right)+\boldsymbol{F}(\boldsymbol{v})\ , \tag{4.1}$$

where $D\boldsymbol{v}/Dt$ is the advective derivative of the fluid velocity, ρ is fluid density, B is magnetic field strength, p is gas pressure in the flux tube, ℓ is the parameterized length of the tube, $\hat{\boldsymbol{b}}$ is the direction along the tube axis defined as $\partial\mathbf{r}/\partial\ell$, $\mathbf{r}$ is the axis of the flux tube in space, $\tilde{\eta}$ is the parallel component of dynamic viscosity of the fluid, $\nabla_\perp$ is the gradient perpendicular to the flux tube axis, and $\boldsymbol{F}$ is the *ad hoc* drag force acting on the tube.

The right hand side of Equation (4.1) contains all the forces on a fluid element. The first term is the total magnetic tension, partly offset by internal gas pressure. The gas pressure moving fluid along the tube is the second term. The third term is the viscous interactions between fluid elements inside the tube. The fourth term is the magnetic pressure exerting a force perpendicular to the tube from the changing magnetic field of the background. The final term is the *ad hoc* drag force exerted on the tube by the ambient plasma, or other retracting flux tubes in the current sheet.

All prior work with PREFT has assumed the flux tube retracted through an ideal current sheet without disturbing it. Previous simulations and observations by Scott et al. (2016) and Savage et al. (2012) respectively have investigated the potential for a flux tube to leave behind a wake as it moves through a plasma sheet. In previous PREFT work, the tacit assumption was that no energy is transferred from the moving tube to the plasma surrounding it. The present work considers, for the first time, the effects of such previously neglected energy transfer on the dynamics of the retracting tube. To include this effect we assume that motion of the tube, perpendicular to its axis, adds energy to a region of surrounding plasma; energy that is removed from the tube itself. Assuming it becomes directed or turbulent kinetic energy in a wake behind the tube leads to classic aerodynamic drag with a force per unit mass (Fan et al., 1994)

$$\boldsymbol{F} = -D\,|\mathbf{v}_\perp|\,\mathbf{v}_\perp \quad , \tag{4.2}$$

where $\mathbf{v}_\perp$ is the component of the fluid velocity perpendicular to the axis. The constant D characterizes the strength of coupling to the external medium, and is proportional to the width of the energized wake divided by the cross-sectional area of the flux tube. For a rigid cylinder moving through unmagnetized fluid this width would be proportional to the cylinder's diameter making $D \propto d^{-1}$. It is far less clear what value D should take in the present case, where the retracting tube disturbs a magnetized plasma sheet composed in part of other retracting flux tubes. SADs are potentially the disturbed wake of a retracting flux tube through the current sheet (Savage et al., 2012), and the interactions of a flux tube moving through plasma have been studied before Scott et al. (2016). In this preliminary investigation of energy transfer in the TFT we will set D to a range of values with the aim of determining if any might lead to better agreement between the model and observations.

PREFT advances the flux tube through a temperature-based energy equation. This form of the energy equation is the most advantageous here as it allows for direct evolution of the most observable quantity, instead of internal energy or pressure. PREFT advances the temperature according to

$$\tilde{c}_v \frac{DT}{Dt} = -T(\nabla \cdot \boldsymbol{v}) + \frac{\bar{m}}{k_B}\frac{\tilde{\eta}}{\rho}\left(\hat{\boldsymbol{b}} \cdot \frac{\partial \boldsymbol{v}}{\partial \ell}\right)^2 + \frac{\bar{m}}{k_B}\frac{B}{\rho}\frac{\partial}{\partial \ell}\left(\frac{\kappa}{B}\frac{\partial T}{\partial \ell}\right) + n_e^2\Lambda(T) + Q(\ell) \ , \tag{4.3}$$

where DT/Dt is the advective derivative of the temperature and $\tilde{c}_v$ is the constant volume specific heat. In addition, $\bar{m}$ is the mean molecular mass, k_b is Boltzmann's constant, κ is the thermal conductivity, n_e is the electron density, $\Lambda(T)$ is the radiative loss function, and Q is the initial equilibrium heating applied to the tube.

In Equation (4.3) each term allows for energy to change forms or to leave the system. The first term is the change in temperature from the compression or expansion of a cell. The second is heating due to viscous effects, balancing out the loss of kinetic energy due to the viscosity from Equation (4.1). The third term is thermal conductivity. PREFT uses classical Spitzer conductivity, with a free streaming limit on the higher end, and a smooth transition in between. The fourth term is a tabulated radiative loss function created from CHIANTI 7.1 (Landi et al., 2013). The final term is the heating required to sustain the initial configuration of the loop.

The TFT model also provides additional constraints on top of the equations used. While the formal derivation of eqs. (4.1) and (4.3) assume $\beta \ll 1$, they can actually be solved as long as $\beta < 2$, beyond which the tension term changes sign leading to a kind of fire-hose instability. The dynamics of the flux tube are fast enough that the background does not change with time. The standard TFT model also assumes that this flux tube is isolated from the background, such that moving it does not disturb or alter the background. This is modified in this case, where we consider the drag as being sourced by the background. This leaves the tube partially isolated, in that the drag interacts with the flux tube, but there is no feedback loop from the interaction. The energy being removed from the system by the drag does not change the background, leaving it static.

With the above equations and constraints, PREFT is set to an initial condition and allowed to evolve. The system chooses the time steps to advance based on the Courant-Friedrichs-Lewy conditions for the system. This allows the system to advance in the most advantageous way without leaving the system unstable.

4.2.1 Initial Conditions

The first step in initializing PREFT is to construct the flux tube. The flux tube is made by starting with a tube in a state of equilibrium along the tube from Rosner et al. (1978). We specify the length, temperatures at the end and middle of the flux tube. The pressure in the tube is set to a constant value, and the density and temperature profiles along the tube are set by the RTV equilibrium according to the minimum and maximum temperature that we have set.

Longcope et al. (2018) applied a pressure-balance argument to SDO/AIA observations of the Sept. 10, 2017 flare and reached the conclusion that the plasma sheet was surrounded by a magnetic field whose strength decreased approximately exponentially, $B(z) = B_0 e^{-(z-z_0)/L}$, with scale height $L = 54.0$ Mm. The pressure balance argument implied a lower bound of $B_0 > 50$ G at the base of the plasma sheet, $z_0 = 40$ Mm. The EOVSA observations of Gary et al. (2018) suggest field strengths greater than this lower bound.

In our exploration we consider four different values of B_0 in an effort to find one that yields a better match to observed dynamics and the EOVSA constraints. Figure 4.1 shows the field profiles resulting from the four different choices. The weakest case $B_0 = 60$ G, is slightly stronger than that in Longcope et al. (2018), with field strength falling to 13.8 G at the apex ($z = 120$ Mm). Other cases successively double B_0 up to 500 G in the strongest. That case has 115 G at its apex. While we consider dynamics only to $z = z_0 = 40$ Mm, the specified profile continues to a point, $z = z_c$ where $B(z_c) = B_x$, the guide field.

The flux tube is now placed within the current sheet with external magnetic field strength $B(z)$ described above. The axis is defined by a magnetic field line integrated rightward from the apex — the point of reconnection. In Unverferth & Longcope (2020) the field line was integrated assuming $\beta = 0$. Here we have included

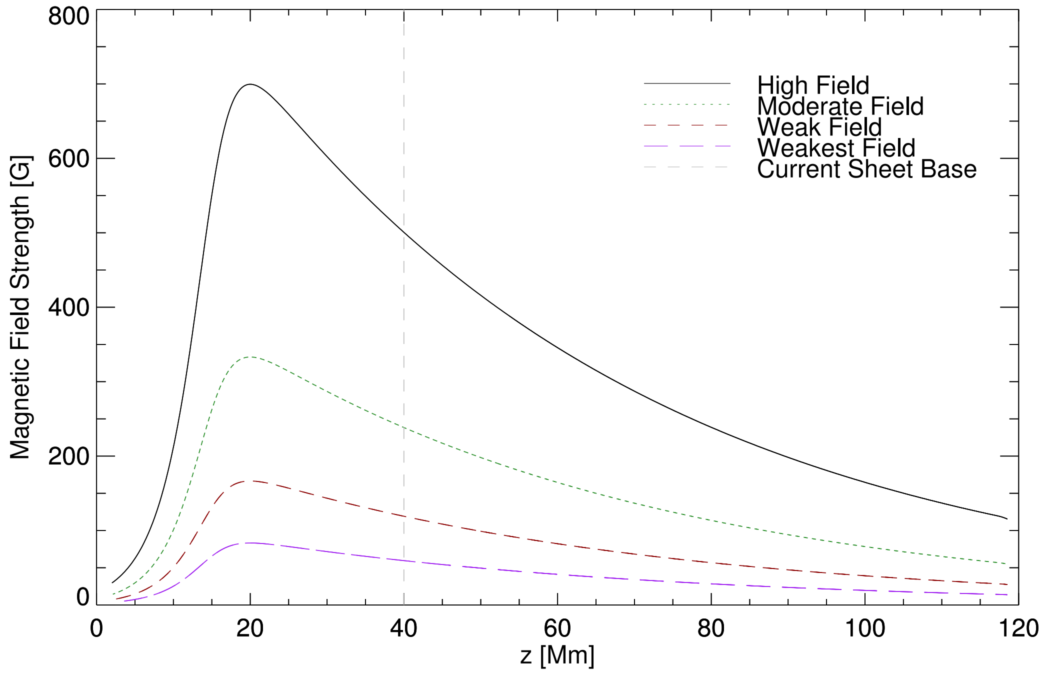

Figure 4.1: The four magnetic fields used in this work. The gray dashed vertical line is the base of the current sheet, with the region of interest to the right. The high field run is solid black, the moderate field in dotted dark green, the weak field in dashed red, and the weakest field in long dashed purple.

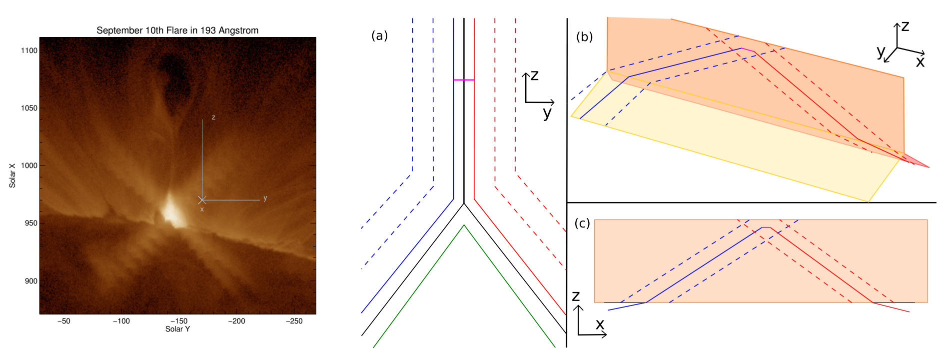

Figure 4.2: Left panel: 193 Å observation of the September 10th flare. Placed on top is the coordinate system used as seen from Earth. Right panel: rotation of the coordinate system from the observations (a) into the orientation used in the PREFT simulations (c).

a modification such that a finite beta is taken into account

$$dx = dl \frac{B_x}{B} \frac{1-\beta_{apex}}{1-\beta} \tag{4.4}$$

$$dz = dl \sqrt{1 - \frac{B_x^2}{B^2} \left(\frac{1-\beta_{apex}}{1-\beta} \right)^2}. \tag{4.5}$$

where x is the horizontal and z is the vertical coordinate, B_x is a uniform guide field component, and β_{apex} and β are the plasma beta at the apex of the flux tube, and the current height respectively. In the left panel of Fig. 4.2, the observed plasma sheet is shown with the coordinate system shown next to it. The right panel then shows how we rotate this coordinate system to obtain the layout for a PREFT simulation. Equations (4.4) and (4.5) result from taking Equation (4.1) and setting pressure to be a constant in the corona, and velocity to be zero. This leaves only the tension and magnetic pressure terms which then can be rearranged as seen. Unverferth & Longcope (2020) used this approach with the pressure set to zero, equivalent to setting β to zero in this field line integration. The integration proceeds until reaching $z = z_c$ where the magnetic field is solely the guide field. We place the rest of the flux tube at this elevation and preserve its length laying it horizontally and stop integration.

The integration above creates the right side of the tube, and the left side is created as its mirror image. A short section of cool dense chromosphere is added to either end of the flux tube. The chromosphere is set to be the specified lower bound temperature of the flux tube, and is isothermal. The chromosphere is affected by gravity and so adopts a stratified layering, with an increasing density and pressure closer to the edges. We place the chromosphere to serve as a mass reservoir for evaporation.

With the flux tube placed in the field, a few final modifications remain. The point at the apex is smoothed into a curve instead of a single point such that it

Drag coefficients D [Mm^{-1}]

Field Strength at $z = 40$ Mm	no/minimal drag	low drag	high drag
500 G	10.0	65.0	200.0
237 G	2.0	12.0	70.0
120 G	0.0	3.0	9.0
60 G	0.0	0.5	3.25

Table 4.1: Value of drag coefficient D for each case

is resolved by multiple points. After being placed in the magnetic field, the mass segments in each tube are recalculated for their new size, as the field controls the radius of each segment in a per flux sense. In Unverferth & Longcope (2020) the heating was rescaled after placing the flux tube in the new field, however this was found to have minimal effect and so is not done here.

In this work we consider 12 possible field and drag combinations. We have four different field strengths, 'strong', 'moderate', 'weak' and 'weakest', described above. Each field strength has a run with minimal or no drag, one with low drag, and one with high drag. The initialization length and temperature are the same. The only difference is the termination of the loop to the flat ends, given by the finite beta conditions. This leads to a slightly different height, but this variation is small compared to the overall extent of the flux tube. The initial conditions are seen in Figure 4.3 as the solid black lines for the moderate low drag case.

4.2.2 Anatomy of Retraction

Before beginning analysis in depth, we illustrate typical behavior with a single case of flux tube evolution. The flux tube under consideration here, is the moderate magnetic field, and low drag, resulting in retraction speeds in the 600 to 700 km/s range. We initialize the simulation as described above, and allow it to evolve. The first event of note happens immediately. The bend at the apex of the flux tube splits into two bends propagating downward along each of the legs, as seen in panel (a) of Fig. 4.3 as the blue dashed lines peel inward from the solid black initial configuration. These are rotational discontinuities (RDs) which travel along the flux tube at the local Alfvén speed. The RDs are difficult to see due to their transverse nature and the drag suppressing this. Another signature of these though is also the launching downward of the flux tube, so the edge of the strong downward velocity in panel (d). These RDs are the site of magnetic tension on the flux tube, which serves to accelerate a jet of material at each bend. These RDs move at the Alfvén speed, unaffected by drag.

Without the drag, the flux tube flattens in the middle, with a horizontal segment connecting the two outward moving RDs. With drag these middle segments are launched downward at a significant fraction of the Alfvén speed. In the drag-free case the middle segments move downward and remain at that velocity leading to the bar like feature in between the expanding RDs. With drag, the middle segments are slowed quickly and are continually tugged down by tension. This balance between the drag and tension results in the arched form as it retracts. This slowdown leads to the split between the Alfvénic signature of the RDs and the much slower retraction signature, reminiscent of the distinct signatures observed by EOVSA (Yu et al., 2020).

As the jets are powered by the RDs, the flow of material is primarily toward the apex of the tube. This evolution behaves similar to the simulations of Guidoni & Longcope (2011) and Unverferth & Longcope (2020). The jets push material to the apex where they interact via a shock and heat the plasma. The material is also significantly compressed by the collision of the two flows. The result then of the jets is that there is now a plug of material that has significantly higher density and temperature than the flux tube outside the jets. This effect is visible in panels (b)

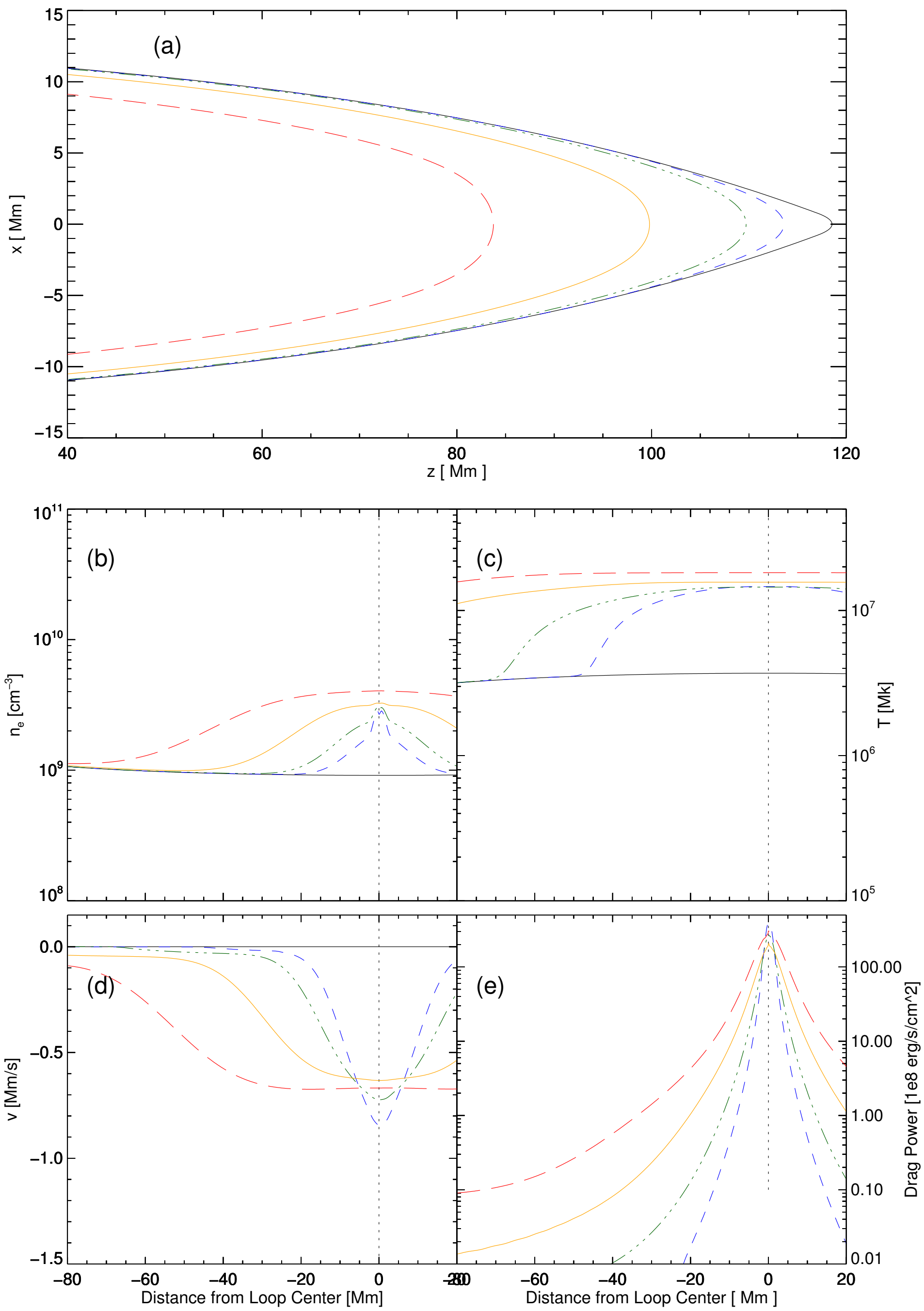

Figure 4.3: Evolution of the moderate field case with low drag. (a) Face on view of the flux tube, with the apex on the right and the base of the current sheet at the left. (b) Electron density as a function of tube length with the apex of the tube at 0. (c) Temperature. (d) Vertical velocity. (e) Drag force multiplied into velocity to give drag power. For each panel, the line style and color denotes the time; black solid is 0 s, dashed blue is 5 s, dashed dotted green is 10 s, solid yellow is 25 s, and long dashed red is 50 s.

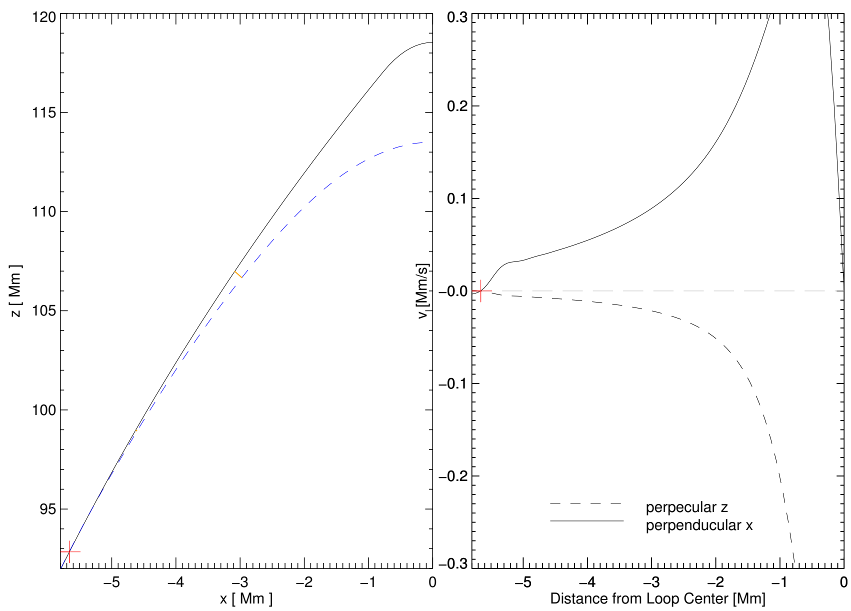

Figure 4.4: Left panel: Highlighting the rotational discontinuity with drag in the moderate field case. The initial position of the flux tube shown in solid black, with the blue dashed line shows the flux tube at 5.1 s. The orange lines marks where the angle from the damped RD is, and the red cross marks the location of the RD. Right panel: The two components of the perpendicular velocity of the flux tube. The solid line indicates the x motion, positive values moving rightward. The dashed line indicates the vertical component of the perpendicular velocity. To the right of the RD, the motion of the tube is downward and towards the center of the flux tube.

and (e) of Figure 4.3 in the dashed blue lines. The density peak is visible and the central plateau of high temperature at the apex is as well, with the temperature peak extending farther than the density.

As retraction continues, the RDs continue to move down the flux tube. The magnetic field increases from the apex to the base of the current sheet at 40 Mm. The RDs accelerate as the field strengthens, they move faster as they approach the base of the current sheet. The travel time for the RDs depends on the magnetic field strength and the initial density. The RDs move faster than the jets, and as such the material has not had any reason to change from the initial conditions by the time the RDs pass through. We can calculate the energy desnity available to the RDs as they propagate down the flux tube by

$$\delta E = 2\psi B^2/8\pi \ . \tag{4.6}$$

ψ is the angle of deflection caused by the RD as it propagates, and can be seen in Fig 4.4. For the moderate field case with low drag, we can measure it to be 0.014 radians. With the value of the magnetic field at the red cross in the left panel of Fig 4.4 of 89.5 gauss, the energy density available to the RD from t = 5.0 to 5.1 s is 6.99×10^7 erg/Mx/s. If this release is responsible for the microwave signatures seen by Yu et al. (2020) then at 100% efficiency it would radiate that energy into a sphere Assuming a flux tube with a flux of 2×10^{19} Mx then at Earth the microwave emission would have an intensity of approximately 0.14 erg/cm^2/s. If we assume that our RD emitted from evenly from 1 to 20 GHz, then we have a source emitting at 7.37×10^{-12} erg/cm^2/s/Hz, or near 7×10^7 sfu. This value would peak as the RD reaches the base of the current sheet, then decay away as RD vanishes. The higher the field strength used would also increase the radiated energy. The whole disk intensity seen by EOVSA during this event surpassed 10^3 sfu (Yu et al., 2020). Even if this source is incredibly inefficient or occurs on flux tubes 1% the size, we can expect that it would still be bright enough to observe.

The continuing retraction of the flux tube allows for the jets to pile more material into the apex of the flux tube. This contributes to the dense region at the apex growing as seen in panel Fig. 4.3 (b) where the dense central region not only is growing in extent, but also density is increasing in time from blue to green to yellow and red. This constant addition of material at speed allows for the conversion of more kinetic energy into thermal as the flows are halted by the material in the way. This constant release of thermal energy allows for the apex to stay hot while thermal conduction works to spread this energy down the legs. As the flux tube retracts, the entire coronal portion of the flux tube reaches temperatures near that of the apex, though the apex continues to have the highest density.

As the retraction progresses from start to finish, the downward velocity changes form primarily due to the drag. Panel (d) shows the evolution of the vertical velocity over the course of retraction. Initially the downward motion is highly peaked at the center of the flux tube. Over time this flattens out and spreads to more of the tube moving downward at a similar velocity. The power lost by drag is found by integrating the density

$$\mathcal{P} = -\rho\,\mathbf{F}\cdot\mathbf{v} = \rho\,D\,|\mathbf{v}_\perp|^3 \quad , \tag{4.7}$$

plotted in Figure 4.3 (e). As the drag force only acts perpendicular to the tube, drag power peaks where the motion is mainly perpendicular to the flux tube. This occurs near the apex and the power drops off quickly from there. As retraction continues, the power in the wings rises, as the drag force works on more of the tube to enforce a more uniform velocity.

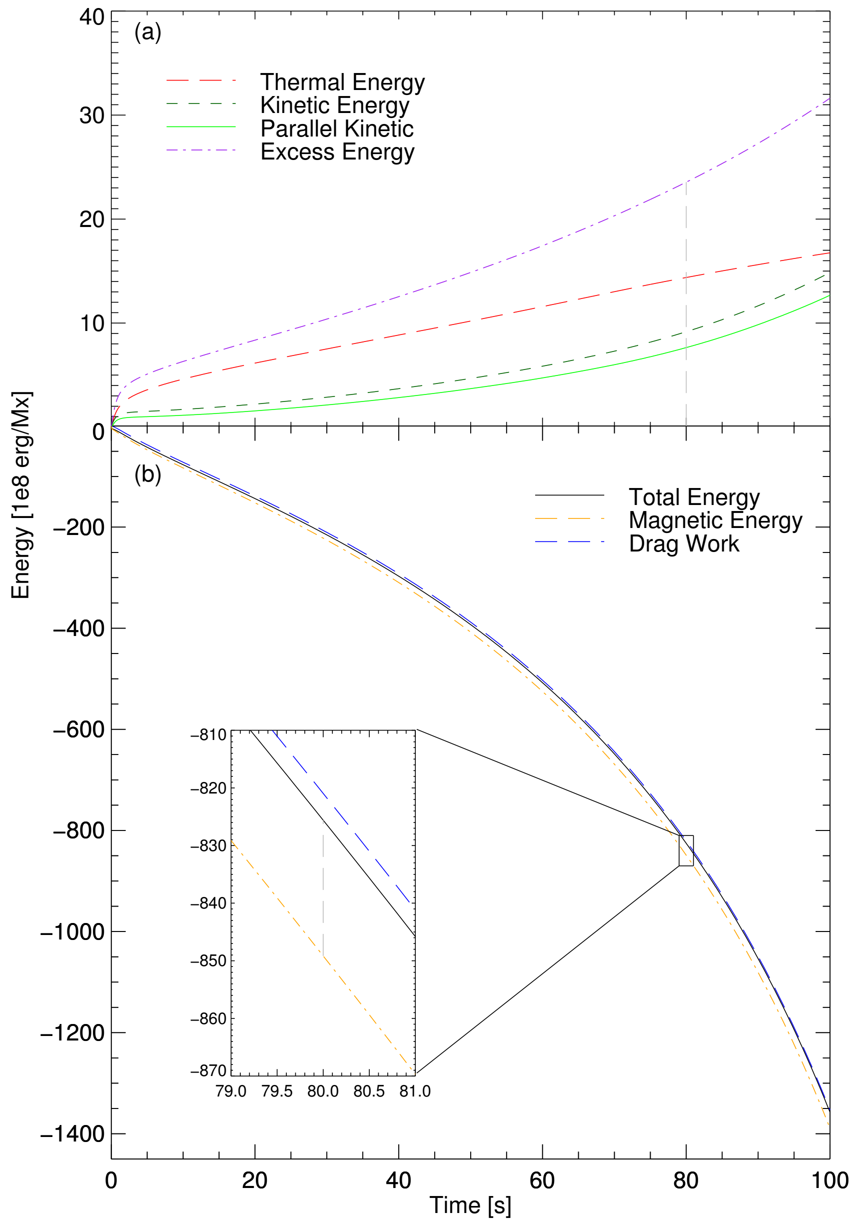

Figure 4.5: Energy for the moderate flux tube with low drag. (a) Energy partitioned during the run normalize to be 0 at the start. Purple Dashed dotted line indicates the excess energy available to be converted to other forms. Thermal energy is long dashed red, total kinetic energy is dashed dark green, and parallel component of kinetic energy is solid light green. The vertical gray line at 80 seconds shows the excess energy. (b) The energy lost, normalized to initial values. the total energy is show as solid black, magnetic as dashed dotted purple, and work removed by drag is long dashed blue. Inset shows a time interval from 79 to 81 seconds, with a vertical gray dashed line showing the excess energy at 80 seconds.

More insight into this specific flux tube can be gathered by considering the evolution and partition of its energies. The energies are shown in Fig. 4.5, where panel (a) shows the breakdown of the energy into kinetic (dark green dashes), kinetic energy in parallel flow (light green solid), thermal energy (red long dashes). The excess energy, plotted as dash-dotted purple, is expressed as $E_{excess} = E_{tot} - E_{mag}$. This is the energy that is available from the shortening of the flux tube and was not lost to drag or radiation. At the beginning of the simulation magnetic energy is quickly made available, as retraction happens rapidly before the drag force has time to act. As the drag force works to slow down the retraction, the rate of magnetic energy release slows. Then as the magnetic field strength increases, the rate of energy release increases again, along with the retraction speed. Most of the kinetic energy is in the parallel motion of the jets, with very little in the motion perpendicular to the tube. As the flux tube retracts, more energy is put into the jets while the amount of perpendicular motion is near constant. This is in direct contrast to the cases presented in Unverferth & Longcope (2020). There the perpendicular motion was the dominant component of the kinetic energy and rapidly increased during retraction. Throughout the run, as the jets continue to pile material into the apex of the loop, the thermal energy consistently increases.

In addition to the partition of available energy, we can also consider the losses. Panel (b) shows the loss of magnetic (dashed-dotted purple) and total energy (solid black). The total energy of the flux tube is the sum of the kinetic, magnetic and thermal energies of the tube. The long dashed blue line is the work done by drag. During retraction, the flux tube loses 1.358×10^{11} erg/Mx (45.4% of its initial total) to the surrounding plasma through drag. It releases 1.389×10^{11} erg/Mx from shortening the field line. Of the magnetic energy released, drag removes 1.353×10^{11} erg/Mx. Throughout the evolution the flux tube has 3.7×10^{9} erg/Mx to drive the internal dynamics. Without drag, roughly half the initial energy of the tube would be used to power internal dynamics and would drive the tube to far greater temperatures than are observed.

4.3 Assessing the Observable Consequences of Drag

To compare the flux tubes that we have created, we turn to the synthetic current sheet used in Longcope et al. (2018). We synthesize a current sheet composed of many flux tubes using copies of a single flux tube simulation at different instants in its evolution. The copies of the flux tube are separated in time by an interval appropriate to the reconnection rate and the flux in each tube. In this instance we will be using the reconnection rate found in Longcope et al. (2018), an average rate of $\dot{\Phi} = 5 \times 10^{17}$Mx/s. We consider the flux tube to be generated rapidly at a very high rate. This event is then followed by a period of no reconnection, resulting in the lower average rate. This work uses that average reconnection rate of 5×10^{17}Mx/s to set an interval between subsequent flux tubes. This current sheet is to be viewed edge on like in Longcope et al. (2018). We use the edge on view of the current sheet, seen in the left panel of Fig. 4.2. This flare provided us with a view of a thin extended plasma sheet, that is presumed to contain the current sheet. Longcope et al. (2018) also measured a temperature and emission measure profile along the height of the current sheet, as did Warren et al. (2018). Those profiles were compared to a synthetic current sheet whose flux tubes retracted too fast.

This work extends the previous work of Longcope et al. (2018) in two important respects. First, it was noted there that the retraction of the flux tube in that work was significantly faster than the observed downward moving features. While an ad hoc attempt was made to see how the retraction speed affected the plasma sheet, it did not do this self-consistently. Here we obtain slower retraction speeds self-consistently through the drag force. Second is the tracking of the rotational discontinuities. These features are a form of MHD shock, which have the potential to serve as sources of non-thermal electrons inferred from observations in MW and radio. We track the RDs from the time of reconnection to crossing the base of the current sheet.

To build the current sheet, the flux tube must first be given a radius, not treated as a one dimensional object. To expand the flux tube, we consider just the region from a height of $z = 40$ Mm to the apex of the flux tube. From this region we construct a cylindrical section for each segment of the flux tube using the formula,

$$r(l,t) = \sqrt{\frac{\Phi}{\pi B(l,t)}}, \tag{4.8}$$

r is our calculated radius of the cylinder, Φ is the flux of the tube, and B is the magnetic field of the current sheet at each position along the flux tube. Here we run into a complication from the previous work. Three of the four cases have stronger magnetic field than used by Longcope et al. (2018). As a consequence, the flux tubes in this work would be smaller for the same amount of flux in Longcope et al. (2018). We have adjusted the flux used to set each case to be the same apparent physical size. This change in flux adjusts the time between each reconnection event generating each flux tube with the rates given above. With this radius we construct an image of each flux tube centered along the axis. In Figure 4.6(a), the flux tube has a width shown, around the solid black line representing the axis of the flux tube. Our line of sight through these simulated flux tubes is in the x direction in Figure 4.3(a). We see through the flux tube, intersecting both legs at any height except the apex, where we see through a more extended apex. Choosing a line of sight enables the construction of the line of sight depth or column at each position.

More useful than the column is the emission measure, an observable quantity.

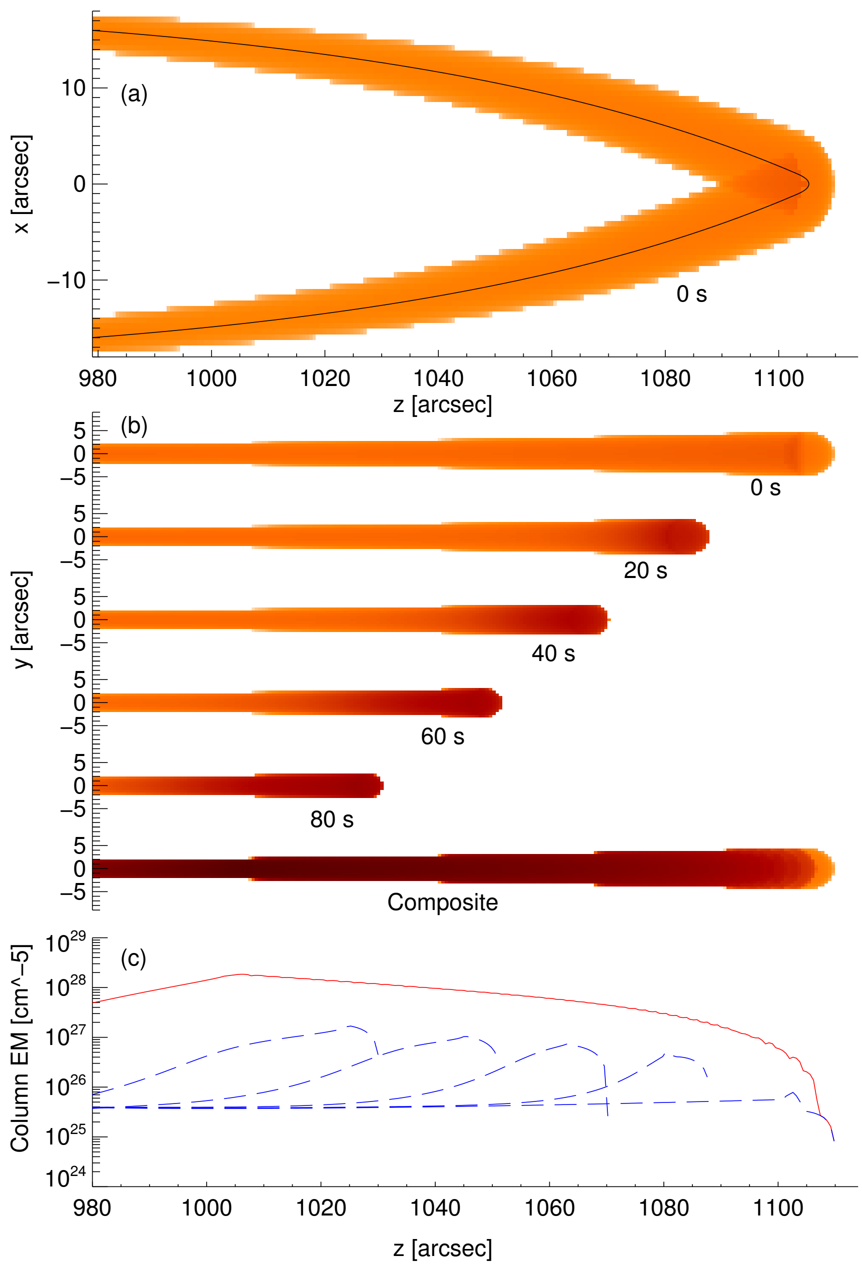

Figure 4.6: Construction of the synthetic plasma sheet from the flux tube. (a) Face on view of the retracting flux tube within the current sheet, plotted as the solid black line at $t = 0$. The orange surrounding shape is the emission measure of the tube for a flux of $2e19$Mx. (b) Edge on views of the emission measure of the same flux tube for multiple times during its retraction. The darker colors here indicate more material along the line of sight, ie more emission measure. (c) Emission measure taken from the centerline $y = 0$ of each flux tube. Individual flux tubes are in long dashed blue lines, and the composite is in solid red.

At each position we take the radius and density to construct the column emission measure as,

$$EM_i(y, z; t_i) = \int n_e^2[\,x, y, z, t_i\,]\, dx, \tag{4.9}$$

with EM_i as the emission measure of the flux tube at time t_i. The electron density is zero outside the flux tube radius, and the value of the flux tube element inside the radius. Figure 4.6 panels (a) and the top image in panel (b) show the initial distribution of the emission measure of the flux tube. Panel (a) shows the face on view, where the overlap near the apex of the tube leads to the increase in the EM there seen in panel (b) in the edge on view. All images in the figure are shown in reverse with darker colors indicating more material along the column. The further images in panel (b) show the flux tube edge on at later times in the retraction, as the apex appears denser and the area of increased density grows past the apex down the legs.

In panel (c) we plot the emission measure from the edge on view along the line $y = 0$, the centerplane of the plasma sheet. Each of these are shown in dashed blue lines and each can be mapped back to an image above by the height of the apex. In each case the peak emission measure is near the apex of the flux tube as it retracts. We have assigned the net flux in order to match the radius to the apparent width of the plasma sheet. We must accommodate this flux to the reconnection rate defined above. The flux values used here have an inherent reconnection time based on the rate set previously, $\tau_{rx} = \Phi/\dot{\Phi}$. For the flux values here, τ ranges from 10 to 80 seconds. These time intervals would lead to a current sheet with coarse features due to the inhomogeneity this causes. We produce a smoother profile by subsampling at a smaller interval, $\Delta t = 2.0$ s, and scaling the EM contribution of this sub-sampled loop by $\Delta t/\tau_{\rm rx}$ We correct for this by using a prefactor to scale the contribution from each time step. This prefactor then enables us to construct a smoother plasma sheet with a higher cadence. The prefactor is constructed by the interval between each step in evolution ($\Delta t = 2.0$ seconds) divided by the time required for the mean reconnection rate to generate a flux tube of this size ($\tau_{rx} = 40.0$ seconds for this field strength). This factor of $\Delta t/\tau_{rx}$ is the adjustment made to compensate for the use of a larger flux tube. If we compile each result spaced 2.0 seconds apart from 0 to 100, we generate the red line in panel (c) according to

$$EM(y,z) = \frac{\Delta t}{\tau_{rx}} \Sigma_{i=0}^{k} EM_i(y,z;t_i), \tag{4.10}$$

i denotes the ith snapshot, and k is the last snapshot used. The composite emission measure increases toward the base of the current sheet, reaching a maximum at the lowest flux tube apex. The peak has the most contribution to the composite curve at any given point in time.

For each of these flux tubes we take the emission measure and the temperature along to the tube to create an emission measure weighted temperature. The EM weighted temperature is compiled for complete current sheet,

$$TEM_i(y,z;t_i) = \int T_i(x,y,z;t_i) n_{e_i}^2(x,y,z;t_i)dx, \tag{4.11}$$

$$T_{EM} = \left(\frac{\Delta t}{\tau_{rx}}\right) \frac{\Sigma_{i=0}^{k} TEM_i(y,z;t_i)}{EM(y,z)}, \tag{4.12}$$

The first step takes a single flux tube and combines the electron density and the temperature and collapses them along the line of sight, x. From here, this integral is summed for all flux tubes in the current sheet, and divided by the EM of the combined sheet. The final product is normalized by the time between flux tubes divided by the reconnection time. This provides the brightest temperature at each point along the current sheet. The centerline values of this temperature for the four moderate field low drag cases are in Fig. 4.8 (c). All the temperatures increase from the apex to the base of the sheet. This is a result of the jets continuing to push material into the apex of the tube and the increase in temperature as the jets continue to collide.

4.3.1 Field Strength

With a synthesized plasma sheet from each case, we consider the effects that field strength has on the synthetic sheet. The field strength is only moderately constrained by observations. For the September 10th event, Longcope et al. (2018) came up with a lower limit on the magnetic field based on the pressure needed to confine the plasma sheet. This value is lower than values reported by Gary et al. (2018) obtained from fitting microwave data at the base of the current sheet. As such we vary the magnetic field strength to attempt to match the observed emission measure and tempearture profiles of the current sheet. As mentioned, we tested this with four different values of the magnetic field. The s̀trong’ field was 500 gauss at the base of the current sheet and 115 gauss at the apex of the flux tube. The ẁeakest’ field was 60 gauss at the base of the current sheet and 13 gauss at the apex. Each of these fields is separated from the nearest by a factor of 2, with the same shape.

Increasing the strength of the magnetic field decreases the travel time of the rotational discontinuities (RDs). The RDs are assumed to form at t=0 when the bend at the apex of the flux tube splits off the two rotational discontinuities. The transit time is calculated as the sum of each cell’s length divided by the local alfvén speed. We consider the arrival of the RD at the base of the current sheet when the point located at the base experiences the maximum outward displacement from transverse motion. In each flux tube the outward direction is considered to be away from the origin, or positive x for the right half and negative x for the left half. In Figure 4.7

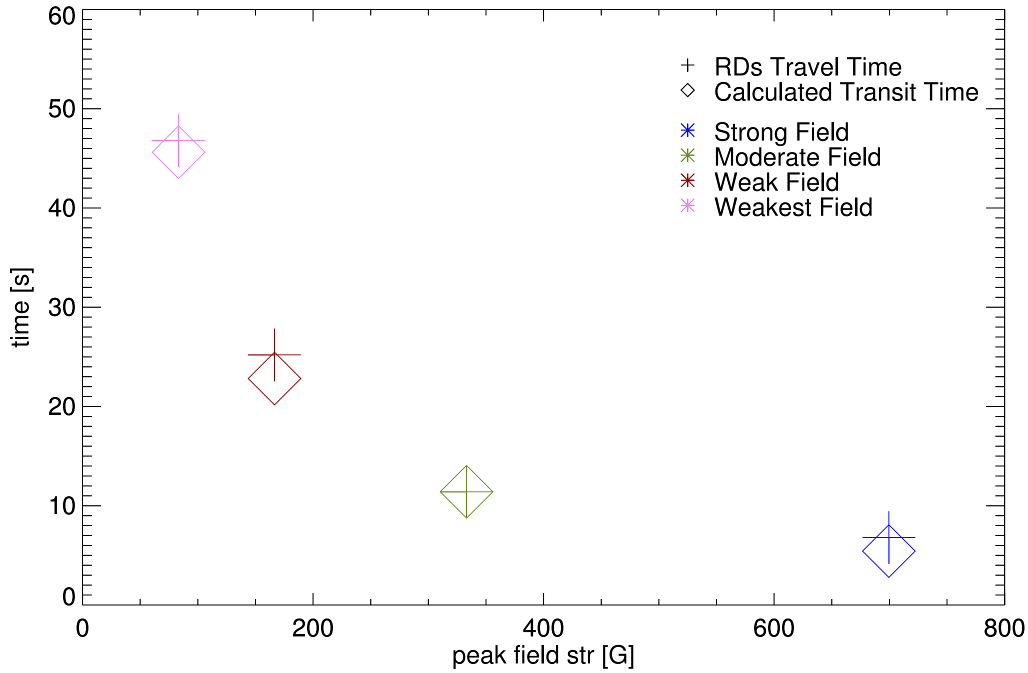

Figure 4.7: Arrival times of the rotational discontinuities (RDs). The diamonds show the calculated transit time from apex to current sheet base at $t = 0$. The crosses show the measured arrival time of the RDs at the base of the current sheet (40 Mm). The strong field is in blue, moderate field in dark green, weak field in dark red, and weakest field in magenta.

the transit time from apex to base is plotted for each case as the colored diamond with each color indicating a field strength. Each doubling of the field strength results in the transit time dropping by one half. The arrival time for each field strength is plotted in the plus symbol with the color matching the diamond of the same field strength. The arrival time also drops by roughly half for the doubling of the field strength.

The RD is slower than the calculated transit time in most cases, but is never faster than it. In all the flux tubes, the initial temperature and density distributions are the same. This is due to the same length and equilibrium condition (RTV) applied to create them. With the Alfvén speed being $v_a = B/\sqrt{4\pi\rho}$, our flux tubes only see one difference between each scenario, the magnetic field strength. In each case the field follows the same profile with the amplitude doubled or halved from the neighboring cases. This results in the arrival times and the transit times halving each step up from the 'weakest' field strength flux tube. This relationship is in line with the expectation that the RDs travel along the flux tube at the local Alfvén speed.

The slight delay in these cases between the transit time, and the actual arrival of the RD is worth discussing. The timing method that we use to time the RD is the maximum displacement of the leg outward at the base of the current sheet. This requires that we consider cases with minimal or no drag, as the drag serves to damp out the transverse oscillations. This is why we have the low or minimal drag flux tubes at all, as the tracking cases for the RDs. The two higher field strength runs still required the use of some drag to allow the run to continue long enough for the RD to reach the base of the current sheet. The use of the maximum does potentially impart a delay between the arrival of the RD and the detection of it. This is potentially exacerbated by this method only being used for the ending time, without the start time suffering the same bias. This drag could affect the timing of the detection of the

RD as well. In addition, the assumption that the bend immediately splits into the two RDs at time t=0 could be incorrect. The use of drag or low field strengths could result in a slower initial development of the RD than expected. As a result, these timings should be considered carefully. Each individual time may have some error to it, the halving between each run is consistent with expectations, and the arrival times match the transit times rather closely.

Weaker magnetic field amplitude increases the emission measure. Fig. 4.8 (b) shows this effect, where weaker field strengths lead to a brighter current sheet. Panel (a) shows that the runs all have approximately the same apex retraction velocities. Each run does differ in the initial velocity, though by approximately 1080 arc-second they have all settled to similar retraction speed. The initial velocity is quite different due to the strength of each field. The drag force does not apply to a flux tube at rest and so the forces working to shorten the flux tube accelerate the tube to a high speed abruptly. The primary driver here then is the magnetic tension, which quickly pulls the tube downward from the apex. As the tension works to drive the tube downward, the drag begins to counter this motion, slowing the tube.

In each individual case, the emission measure is highest near the apex of the flux tube. The jets of plasma mentioned earlier concentrate material there. This is clear in Fig. 4.6 (b), as the peak of the flux tube moves down, more material has been moved into the apex from the legs by the jets. As time moves on, the enhanced emission measure is now far less confined to the apex of the loop, seen in Figure 4.6 (c). While there are significantly more legs of a flux tube at any given height, the contribution they make to the current sheet is much smaller than that of the apexes. Near the base of the current sheet, where retraction halts, the contribution is on the order of 10%. The collection of apexes at or slightly above a given height are what contribute most to the emission of the current sheet.

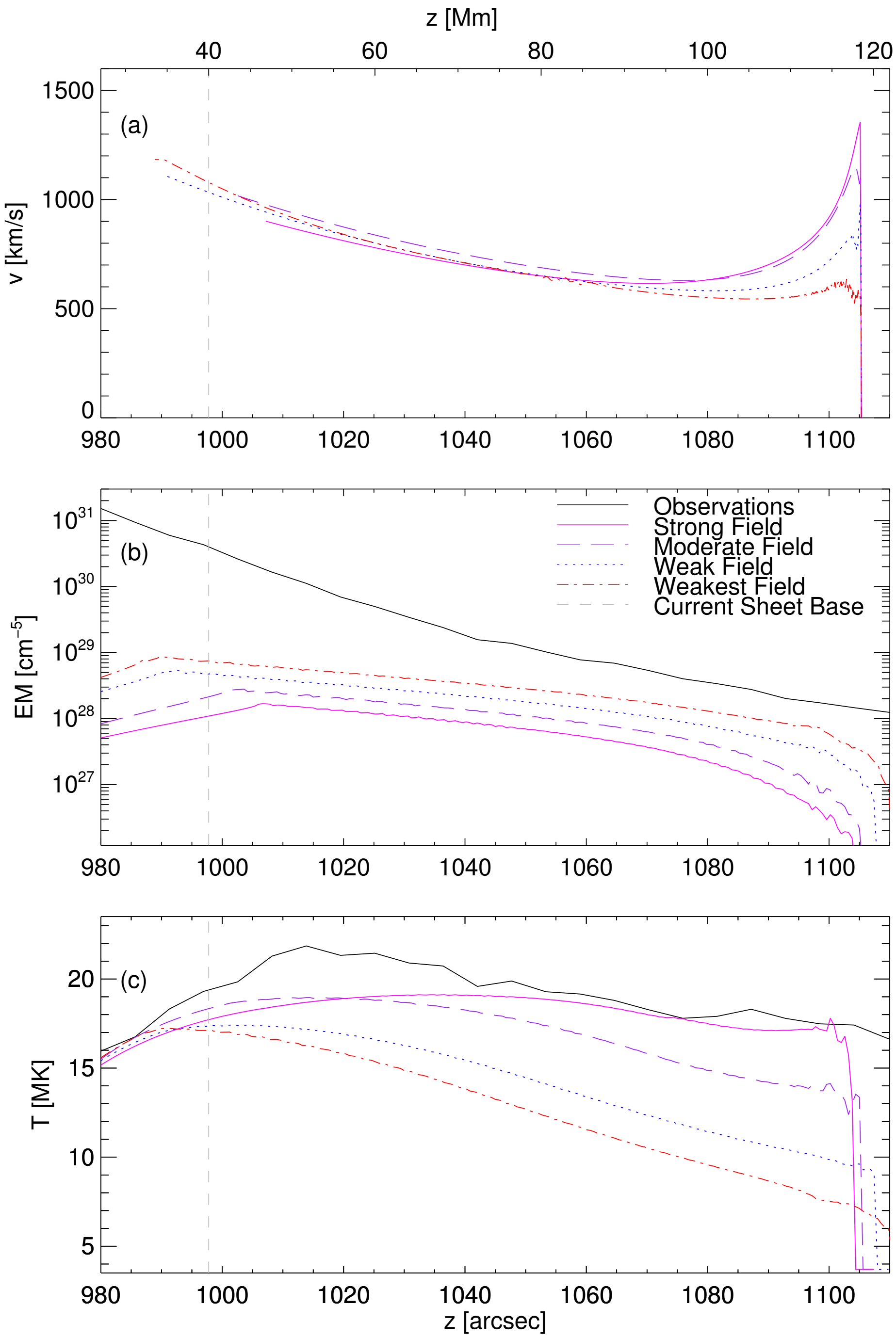

Figure 4.8: Synthetic current sheet results for low drag cases. (a) Retraction velocity at the apex. (b) Emission measure along the centerline of the current sheet. (c) Emission measure weighted temperature along the centerline of the current sheet. Observations of the current sheet from Longcope et al. (2018) in solid black, strong field flux tube in solid magenta, moderate field in long dashed purple, weak field in dotted blue, weakest field in dashed dotted red, and the base of the current sheet in dashed gray.

The temperature at the top of the synthetic plasma sheet is determined by the apex temperature at the start of retraction. Given the relatively few time intervals that contribute to the top of the plasma sheet, the conditions there favor the dense hot source created by jets in the middle of the flux tube, over the cold less dense initial conditions. The energy is stored in the magnetic field along the flux tube, so a higher field leads to a higher rate of release, powering stronger jets. The stronger jets lead to a higher temperature in the middle of the flux tube. These jets also affect the middle of the plasma sheet, as the apex dominates the temperature here to, increasing as it moves down and the jets continue to heat the middle of the flux tube.

At the base of the current sheet ($z = 40Mm$), the temperature of the four cases in Fig. 4.8 approach the same values. This is due to the abundance of samples there at the same low temperature. By the time the thermal conduction front has moved energy down to the lower legs to heat the plasma there, the plasma sheet has many more contributions from cooler legs. The legs of each case heat at a different time from the other cases. This results from the thermal conduction being dependent on the temperature generated in the apex, as well as the gradient of the temperature down the legs. With weaker jets generating lower temperatures in the apex, the thermal conduction fronts move down slower. The heated legs also do not share an increased emission measure for some time, putting them on par with the emission measures from an unheated leg. At later times, the apex reaches down to these heights, and does serve to raise the temperature there.

Of note is the two possible ways to normalize these synthetic current/plasma sheets to compare the cases. The first is to make the flux tubes the same apparent size, that is to allow for the flux to increase with the field strength to keep the area consistent. This works out to normalizing the line of sight depth along the current sheet. Alternatively, one can normalize the current sheet to keep the reconnection rates the same, forcing $\Delta t/\tau_{rx}$ constant for all the current sheets. This will allow the flux tubes to change radius as a function of magnetic field. In the constant line of sight depth case, the prefactor is larger. In the constant flux case, the tube itself is physically larger, making the column larger, despite a constant prefactor. To compare these cases to observations, picking the normalization depends on the purpose. If observations clearly dictate the size of the observed flux tubes, then varying flux to ensure the size matches is more reliable than matching the reconnection rate. Conversely if the reconnection rate is clear, then setting the rate of flux tube generation is a more correct approach. However, in this work neither approach reliably allowed for the synthetic current sheet to match observations in both EM and EM-weighted temperature.

The trends discussed are unaffected by the choice of normalization discussed earlier. The choice slightly changes the spread between the various cases emission measure. This comes about due to keeping a consistent column depth, while changing the prefactor is a larger change than keeping the prefactor consistent and changing depth due to the square root in Equation (4.8). For Figure 4.8 we have shown the value with a consistent prefactor, allowing the flux tubes to change radius as field amplitude changes. This allows for a more ready comparison to the following section which compares cases with the same prefactor.

4.3.2 Retraction Speed

We also varied the drag coefficient, in an attempt to produce speeds more consistent with the observations from the September 10th flare (Longcope et al., 2018). The downward moving features were seen moving downward at less than 1 Mm per second. We created two collections of flux tubes, one that retracts at 600-

700 km/s minimum increasing as it moves into stronger fields as seen in Fig. 4.8. This group of cases is at the faster end of the observations. The second retracts at a minimum of 300-400 km/s and also increases as it moves into stronger fields. This group is very close to the median retraction speed reported in Longcope et al. (2018). These two groups are joined by the no/minimal drag runs that we used to explore the RD travel times, giving three retraction speeds at each of the field strengths. It is worth noting that the stronger field runs release too much energy for the no or minimal drag runs to be useful past the RD measurements already discussed.

The flux tube increases speed as it nears the base of the current sheet. This is not only seen in panels (a) of Figs 4.9 and 4.8, but also in the energies in Figure 4.5 (a). As retraction nears the base of the current sheet, the higher field means that more energy is released per length and more of this energy is converted to kinetic energy before it can be converted into thermal through the viscous interactions of the two jets. This increase in kinetic energy will only boost the drag force by a fraction of the total velocity squared, as the drag is only acting on the velocity perpendicular to the tube. The retraction reaches a point where the drag is no longer siphoning enough energy out to keep the speed low and so the tube accelerates downward.

The retraction speed has a small but noticeable effect on the emission measure of the current sheet. Higher drag runs retract slower, and show elevated emission measure compared to faster runs of the same field. This is the contribution of more flux tubes, as they exist in the region of interest in the current sheet for longer. These additional flux tubes serve to enhance the brightness by their presence, without needed to have the enhanced EM from their apex.

Allowing for faster or slower retraction changes the EM weighted temperature along the current sheet. It affects the temperature profile differently than the field strength. Changing the field strength altered the value at the top of the current

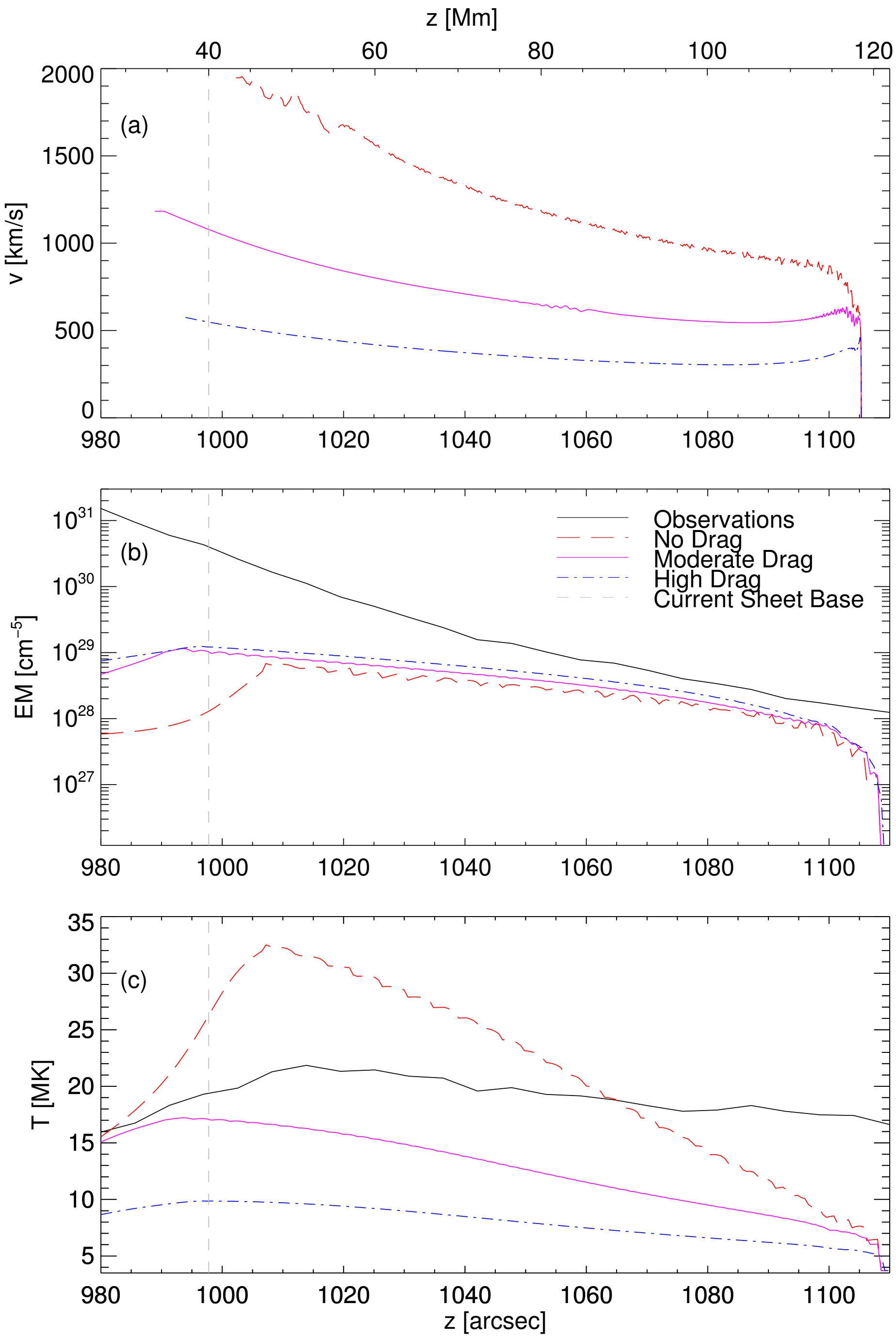

Figure 4.9: Synthetic current sheet results of the weakest field case. (a) Retraction velocity at the apex. (b) Emission measure along the centerline of the current sheet. (c) Emission measure weighted temperature along the centerline of the current sheet. Observations of the current sheet from Longcope et al. (2018) in solid black, no drag run in long dashed red, low drag in solid magenta, high drag in dashed dotted blue, and the base of the current sheet in dashed gray.

sheet, all field strengths tended toward similar values at the base of the current sheet. Allowing for different retraction speed changes the slope moving toward the base of the current sheet with the top of the current sheet starting at the same temperature. This also removes the converging of the sheets to a similar value. For each shortening of the flux tube at the same height in the current sheet, the same energy is converted from magnetic to other forms. Reducing the drag reduces the amount that is removed from the flux tube. The result is that the kinetic energy receives a larger portion of this, causing a faster retraction, and more powerful jets. The faster jets lead to a more dramatic heating in the apex of the flux tube. At the start of the retraction, before drag has had a chance to act significantly, the three runs proceed similarly, which leads to the top of the current sheet having similar temperatures. This heating continues as the retraction moves forward, and heats the plug of material in the middle even more. This continual heating leads to a drastic difference between runs with no drag, low and high drag. As the apex of the flux tube is denser than the legs, it contributes to the overall emission measure strongly, and raises the temperature of the whole current sheet substantially.

4.4 Discussion

This work has shown that the presence of drag changes multiple observables of a current sheet. We created four different field strengths of the same plasma sheet profile, and tested multiple speeds of retraction, mediated by a drag force with varying drag coefficients. This was done by creating a magnetic field of the same shape as used in Longcope et al. (2018). Each case used a different field strength, two times stronger the previous one. Further, each flux tube of a specified field strength was allowed to retract in two speed ranges. These speed ranges were controlled by changing the drag coefficient for each run. The flux tubes were allowed to retract with no drag, tracking the movement of the rotational discontinuities moving down the flux tube from the reconnection site. The timing of these RDs moving down the legs of the flux tube matched the calculated transit times rather well. With the flux tubes, we constructed a synthetic plasma sheet for each case. The weaker the field in the current sheet, the brighter the plasma sheet was, which was also the case for a slower retraction. A faster retraction resulted in a hotter plasma sheet as we moved down to the base. The stronger fields raised the temperature at the top of the current sheet.

We also find that the flux tubes consistently experience a sharp deceleration after initial retraction begins. This slowing then damps down as the drag establishes a rather uniform speed of retraction. Then as the retraction moves into stronger field regions, the flux tube accelerates downward, despite the presence of the drag. This acceleration can be small, a few km/s^2, and seems to peak at 10 km/s^2 at the base of the current sheet. This contrasts with what was observed in Savage & McKenzie (2011), where a large sample of SADs had shown either decelerations or no acceleration.

Slower retractions lead to a brighter plasma sheet. Many models have been attempting to explain the brightness in a plasma sheet through density enhancing shocks. Here we find that a slower retraction allows more flux tubes to exist in the current sheet at a time, contributing to a higher brightness overall. Without drag, the plasma sheet is too dim and too hot. These plasma sheets also reach EM-weighted temperatures in excess of 30 MK, well above the observed values for the September 10th Event, which the previous work drew from.

The increased drag that causes the slower retraction has an interesting consequence. In this work we considered the retraction of an isolated flux tube against a static background. The consequence of the drag is that this kinetic energy being siphoned off the retracting flux tube must go somewhere. In fact, that energy is being distributed to the surrounding material and flux tubes. The energy imparted to the surrounding material is potentially then involved in turbulent motions and heats the surrounding material. This could further increase the temperature of a plasma sheet past what we have seen in this work, especially in weaker magnetic fields but higher drag regimes (McKenzie, 2013). The transfer of energy from the the flux tube to the plasma sheet leading to heating of the current sheet material could be similar to the results of Hanneman & Reeves (2014); Reeves et al. (2017), with the SADs appearing to have colder material than the ambient material in the current sheet.

The propagating RDs in the flux tube were not slowed by the addition of the drag. The signatures of the RDs were damped out by the drag due to both being a perpendicular effect however. More robust definitions of drag and interaction between flux tubes could result in more complex effect on these signatures. We expect that the rotational discontinuities could produce emission detectable in the MW range, even with the effect of drag dampening the amplitude.

The observations reported in Yu et al. (2020) of both a prompt set of potentially paired loop top and loop leg emission, and of the slowly retracting loops are useful. If we take these observations at face value, then it is consistent with reconnection models that the prompt transit of emission from the loop top to the loop leg would serve as a fast signature of reconnection. The slow retraction is consistent with other observations (Longcope et al., 2018). In our TFT model of the current sheet, the reconnection contains both a prompt and a slow signature. The fast signature propagates down the loop leg via the RDs, where it releases microwave and radio signatures, like those observed by Yu et al. (2020). The slow signature is the slow moving retraction of the reconnected flux tube itself, slowed by the tube interacting with the remainder of the plasma sheet. Linking these two is the presence of some drag or similar force that works to mediate interaction between the ambient plasma in the current sheet and the retracting flux. The result of the drag is to take originally Alfvénic outflow, and reduce its speed before it becomes observable.

Going forward, the use of drag in more complex simulations may reveal how the flux tubes would properly interact with each other. This approach could explore where the dissipated energy from the flux tube ends up. Also a more complex definitions of drag in this type of TFT model may also prove enlightening.

CHAPTER FIVE

CONCLUSION

In the introduction for this work we posed three open questions in flare dynamics. Each of these was an area in which models met each other, or observations and the model fell short of explaining the interaction between the two. How do the magnetic canopy and evaporation during a flare interact? What is the magnetic field profile along a flaring current sheet? Can drag mediate Alfvénic outflows to speeds consistent with observations? The work in each of these chapters addressed in turn each of the questions, providing explanations for these interactions.

Chapter 2 investigated the connection between the magnetic canopy and the energy release in the corona. It was unclear at the start of this project how the canopy would interact with the driving of evaporation from below. This project showed the existence of a shock forming during flow through a chamber. This shock could either remain in the chamber or move upstream. Moving upstream changed the incoming conditions, leading to a slower, less dense flow into the remainder of the flux tube. If the shock remained in the flux tube, then it allowed for material to leave the chamber rapidly, near the sound speed. As the material was shocked it was denser than the outflowing material was in the unshocked case. This study provided an answer, the magnetic canopy could hinder or enhance the emission and flow of material into coronal loops. The shock also had a side effect in that in spectral lines, it split the spectrum into a subsonic and supersonic component and could bias observations against the supersonic upflow. This would help to explain observations where Fe XXI only appears to evaporate subsonically from the chromosphere, despite models showing otherwise. This approach could be further enhanced by the inclusion of a non-isothermal fluid and still retain the simplicity of a one-dimensional model.

The primary goal of Chapter 3 was to determine whether the variation of magnetic field strength along the current sheet resulted in observable consequences. Instead of simply working with a uniform field along the current sheet as many other studies, we tested three kinds of profiles. One was the uniform case as a comparison, while the second had the reconnection site placed at the height of maximum field and the third placed above that maximum field. These three cases lead to distinct observables. Reconnection at the maximum field leads to a flux tube without a pronounced central plug of hot dense material like the other two cases. It also lacks significant emission at hotter temperatures despite reaching these temperatures, a feature of the other two cases. Both the uniform field and reconnection above the maximum field had more of a dense plug of material at the apex. These two cases also showed excess emission in the ten to twenty megakelvin range. These signatures could be captured in observations to help determine the location of reconnection and indicate that the reconnected flux should experience a difference based on the reconnection locations.

Chapter 4 explored whether interactions of a retracting flux tube with the surrounding current sheet may have an observable impact. The interaction of the flux tube with the current sheet was considered as an added drag force to the thin flux tube momentum equation. By adding a drag term to the TFT model, this enhances the brightness of the current sheet overall. In addition, this drag helps to limit the temperature in the current sheet. Without drag, the field strengths used caused the temperature in the flux tube to exceed observed values. Weaker field strengths show lower temperatures, though the weakest run here still is hotter than observations without drag. The drag siphons out enough of the converted kinetic energy that the thermalization in the apex of the flux tube is mild. The transfer of energy from the flux tube to the surrounding plasma is potentially the cause for the surrounding plasmas higher temperature as seen in Hanneman & Reeves (2014); Reeves et al. (2017). This drag serves three important purposes. It slows the retraction of flux, bringing the speeds into agreement with the observed values of SADs and SADLs. While the drag does manage to bring speeds into line, the implementation used is lacking in some ways. This is what results in the discrepancy between the accelerations seen with the drag and the work done by Savage & McKenzie (2011). The drag slows the retraction from Alfvénic velocity, and the flux then spends longer in the current sheet, which leads to more emission measure in the current sheet. This is useful as even with the gas dynamic shocks increasing the apex density, it falls short of observations. Finally, the drag siphons off a significant portion of the released energy, feeding it into the surroundings and preventing the overheating of the model tube compared to observations.

The three projects all used a form of one-dimensional models, either directly or in the form of the TFT. Despite the simplicity of such a model, each investigation yielded novel results that reveal important considerations. In each case there was an additional effect resulting from the added dynamics. The dynamics were motivated by observations, and the results imply that these effects should be considered in full three-dimensional MHD simulations. The TFT model is not full MHD but serves this important role of exploring potential effects on a simple scale to determine if they even work. That the TFT reproduces expected results in simple cases lends validity to the results that it obtains in works with additional novel effects.

Bibliography

Aly, J. J., & Amari, T. 1989, A&A, 221, 287

Antonucci, E., & Dennis, B. R. 1983, Sol. Phys., 86, 67

Antonucci, E., et al. 1982, Sol. Phys., 78, 107

Aurass, H., Vršnak, B., & Mann, G. 2002, A&A, 384, 273

Baty, H., Priest, E. R., & Forbes, T. G. 2006, Physics of Plasmas, 13, 022312

Benz, A. O. 2017, Living Reviews in Solar Physics, 14, 2

Benz, A. O., & Smith, D. F. 1987, Sol. Phys., 107, 299

Berger, M. A., & Asgari-Targhi, M. 2009, ApJ, 705, 347

Berger, T. E., & Title, A. M. 1996, ApJ, 463, 365

Bhattacharjee, A., Huang, Y.-M., Yang, H., & Rogers, B. 2009, Physics of Plasmas, 16, 112102

Biernat, H. K., Heyn, M. F., & Semenov, V. S. 1987, J. Geophys. Res., 92, 3392

Birn, J., et al. 2001, J. Geophys. Res., 106, 3715

Biskamp, D., & Schwarz, E. 2001, Phys. Plasmas, 8, 4729

Bradshaw, S. J., Del Zanna, G., & Mason, H. E. 2004, A&A, 425, 287

Bradshaw, S. J., Emslie, A. G., Bian, N. H., & Kontar, E. P. 2019, ApJ, 880, 80

Braginskii, S. I. 1965, in Reviews of Plasma Physics, ed. M. A. Leontovich (New York: Consultants Bureau), 205

Brosius, J. W. 2009, ApJ, 701, 1209

Brosius, J. W. 2013, ApJ, 762, 133

Brosius, J. W., & Phillips, K. J. H. 2004, ApJ, 613, 580

Cargill, P. J., & Bradshaw, S. J. 2013, ApJ, 772, 40

Cargill, P. J., Mariska, J. T., & Antiochos, S. K. 1995, ApJ, 439, 1034

Cargill, P. J., & Priest, E. R. 1982, Sol. Phys., 76, 357

Carmichael, H. 1964, A Process for Flares, Vol. 50 451

Carrington, R. C. 1859a, MNRAS, 20, 13

Carrington, R. C. 1859b, MNRAS, 19, 81

Carroll, B. W., & Ostlie, D. A. 2007, An introduction to modern astrophysics (Pearson Addison Wesley)

Caspi, A., & Lin, R. P. 2010, ApJ, 725, L161

Caspi, A., Shih, A. Y., McTiernan, J. M., & Krucker, S. 2015, ApJ, 811, L1

Chen, B., Shen, C., Reeves, K. K., Guo, F., & Yu, S. 2019, ApJ, 884, 63

Cheng, C. C., Oran, E. S., Doschek, G. A., Boris, J. P., & Mariska, J. T. 1983, ApJ, 265, 1090

Cowling, T. G. 1956, MNRAS, 116, 114

Dabrowski, B. P., & Benz, A. O. 2009, A&A, 504, 565

Del Zanna, G. 2008, A&A, 481, L69

Doschek, G. A., Warren, H. P., Dennis, B. R., Reep, J. W., & Caspi, A. 2015, ApJ, 813, 32

Drake, J. F., Cassak, P. A., Shay, M. A., Swisdak, M., & Quataert, E. 2009, ApJL, 700, L16

Dungey, J. W. 1953, MNRAS, 113, 679

Emslie, A. G., Kontar, E. P., Krucker, S., & Lin, R. P. 2003, ApJ, 595, L107

Emslie, A. G., Li, P., & Mariska, J. T. 1992, ApJ, 399, 714

Erkaev, N. V., Semenov, V. S., & Jamitsky, F. 2000, Phys. Rev. Lett., 84, 1455

Fan, Y., Fisher, G. H., & McClymont, A. N. 1994, ApJ, 436, 907

Fang, X., Yuan, D., Xia, C., Van Doorsselaere, T., & Keppens, R. 2016, ApJ, 833, 36

Faurobert, M., & Arnaud, J. 2002, A&A, 382, L17

Fisher, G. H., Canfield, R. C., & McClymont, A. N. 1984, ApJ, 281, L79

Fisher, G. H., Canfield, R. C., & McClymont, A. N. 1985, ApJ, 289, 425

Fletcher, L., et al. 2011, Space Sci. Rev., 159, 19

Fletcher, L., Pollock, J. A., & Potts, H. E. 2004, Sol. Phys., 222, 279

Forbes, T. 2010, Models of coronal mass ejections and flares, ed. C. J. Schrijver & G. L. Siscoe 159

Forbes, T. G., & Malherbe, J. M. 1986, ApJ, 302, L67

Forbes, T. G., & Priest, E. R. 1987, Rev. Geophys., 25, 1583

Forbes, T. G., Priest, E. R., Seaton, D. B., & Litvinenko, Y. E. 2013, Physics of Plasmas, 20, 052902

Forbes, T. G., Seaton, D. B., & Reeves, K. K. 2018, ApJ, 858, 70

Foukal, P. 1990, Solar astrophysics

Gabriel, A. H. 1976, Philosophical Transactions of the Royal Society of London Series A, 281, 339

Gary, D. E. 2016, in 2016 URSI Asia-Pacific Radio Science Conference (URSI AP-RASC), 1

Gary, D. E., et al. 2018, ApJ, 863, 83

Gary, G. A. 2001, Sol. Phys., 203, 71

Graham, D. R., & Cauzzi, G. 2015, ApJ, 807, L22

Green, R. M. 1965, in IAU Symposium, Vol. 22, Stellar and Solar Magnetic Fields, ed. R. Lust, 398

Guidoni, S. E., & Longcope, D. W. 2010, ApJ, 718, 1476

Guidoni, S. E., & Longcope, D. W. 2011, ApJ, 730, 90

Hanneman, W. J., & Reeves, K. K. 2014, ApJ, 786, 95

Hasan, S. S. 2008, Advances in Space Research, 42, 86

Hesse, M., Schindler, K., Birn, J., & Kuznetsova, M. 1999, Phys. Plasmas, 6, 1781

Hirayama, T. 1974, Sol. Phys., 34, 323

Howard, R., & Stenflo, J. O. 1972, Sol. Phys., 22, 402

Hudson, H. S. 1972, Sol. Phys., 24, 414

Hudson, H. S., Wolfson, C. J., & Metcalf, T. R. 2006, Sol. Phys., 234, 79

Jaeggli, S. A., Judge, P. G., & Daw, A. N. 2018, ApJ, 855, 134

Jing, J., Qiu, J., Lin, J., Qu, M., Xu, Y., & Wang, H. 2005, ApJ, 620, 1085

Karimabadi, H., Krauss-Varban, D., Huba, J. D., & Vu, H. X. 2004, JGR, 109, A09205

Karlický, M., & Bárta, M. 2011, ApJ, 733, 107

Karlický, M., Chen, B., Gary, D. E., Kašparová, J., & Rybák, J. 2020, ApJ, 889, 72

Karlický, M., & Kosugi, T. 2004, A&A, 419, 1159

Kawabata, K. A., Ogawa, H., & Suzuki, I. 1983, Sol. Phys., 86, 247

Kazachenko, M. D., Lynch, B. J., Welsch, B. T., & Sun, X. 2017, ApJ, 845, 49

Kopp, R. A., & Pneuman, G. W. 1976, Sol. Phys., 50, 85

Kosugi, T., Sakao, T., Masuda, S., Hara, H., Shimizu, T., & Hudson, H. S. 1994, in Proceedings of Kofu Symposium, 127

Kundu, M. R., Schmahl, E. J., & Velusamy, T. 1982, ApJ, 253, 963

Landau, L. D., & Lifshitz, E. M. 1959, Fluid mechanics

Landi, E., Young, P. R., Dere, K. P., Del Zanna, G., & Mason, H. E. 2013, ApJ, 763, 86

Landi, S., Del Zanna, L., Papini, E., Pucci, F., & Velli, M. 2015, ApJ, 806, 131

Lemen, J. R., et al. 2012, Sol. Phys., 275, 17

Levine, R. H. 1974, ApJ, 190, 457

Lin, R. P., et al. 2002, Sol. Phys., 210, 3

Lin, R. P., & Hudson, H. S. 1976, Sol. Phys., 50, 153

Linton, M. G., DeVore, C. R., & Longcope, D. W. 2009, Earth, Planets, and Space, 61, 573

Linton, M. G., & Longcope, D. W. 2006, ApJ, 642, 1177

Lites, B. W., Skumanich, A., & Martinez Pillet, V. 1998, A&A, 333, 1053

Litvinenko, Y. E., Forbes, T. G., & Priest, E. R. 1996, Sol. Phys., 167, 445

Liu, W., Liu, S., Jiang, Y. W., & Petrosian, V. 2006, ApJ, 649, 1124

Livingston, W. 2002, Sol. Phys., 207, 41

Longcope, D., Qiu, J., & Brewer, J. 2016, ApJ, 833, 211

Longcope, D., Unverferth, J., Klein, C., McCarthy, M., & Priest, E. 2018, ApJ, 868, 148

Longcope, D. W. 2005, Liv. Rev. Solar Phys., 2, Online Article

Longcope, D. W. 2014, ApJ, 795, 10

Longcope, D. W., Des Jardins, A. C., Carranza-Fulmer, T., & Qiu, J. 2010, Sol. Phys., 267, 107

Longcope, D. W., & Forbes, T. G. 2014, Solar Phys., 6, 2091

Longcope, D. W., Guidoni, S. E., & Linton, M. G. 2009, ApJ, 690, L18

Longcope, D. W., & Klimchuk, J. A. 2015, ApJ, 813, 131

Longcope, D. W., Qiu, J., & Brewer, J. 2016, ApJ, 833, 211

Machado, M. E., & Rust, D. M. 1974, Sol. Phys., 38, 499

MacNeice, P., Burgess, A., McWhirter, R. W. P., & Spicer, D. S. 1984a, Solar Phys., 90, 357

MacNeice, P., McWhirter, R. W. P., Spicer, D. S., & Burgess, A. 1984b, Sol. Phys., 90, 357

Magara, T., Mineshige, S., Yokoyama, T., & Shibata, K. 1996, ApJ, 466, 1054

Marsh, K. A., & Hurford, G. J. 1982, ARA&A, 20, 497

Masuda, S., Sato, J., Kosugi, T., & Sakao, T. 2000, Advances in Space Research, 26, 493

McIntosh, P. S. 1981, in The Physics of Sunspots, ed. L. E. Cram & J. H. Thomas, 7

McIntosh, P. S., & Donnelly, R. F. 1972, Sol. Phys., 23, 444

McKenzie, D. E. 2013, ApJ, 766, 39

McKenzie, D. E., & Hudson, H. S. 1999, ApJ, 519, L93

McKenzie, D. E., & Savage, S. L. 2009, ApJ, 697, 1569

Melnikov, V. F., Shibasaki, K., & Reznikova, V. E. 2002, ApJ, 580, L185

Michael, A. T., Opher, M., & Tóth, G. 2018, ApJ, 860, 171

Milligan, R. O. 2015, Sol. Phys., 290, 3399

Milligan, R. O., & Dennis, B. R. 2009, ApJ, 699, 968

Muller, R. 1983, Sol. Phys., 85, 113

Nagai, F. 1980, Sol. Phys., 68, 351

Najita, K., & Orrall, F. Q. 1970, Sol. Phys., 15, 176

Neupert, W. M. 1968, ApJ, 153, L59

Nindos, A., White, S. M., Kundu, M. R., & Gary, D. E. 2000, ApJ, 533, 1053

Nisenson, P., van Ballegooijen, A. A., de Wijn, A. G., & Sütterlin, P. 2003, ApJ, 587, 458

Parker, E. N. 1957, J. Geophys. Res., 62, 509

Parker, E. N. 1963, ApJS, 8, 177

Parker, E. N. 1973, ApJ, 180, 247

Parker, E. N. 1975, ApJ, 198, 205

Penn, M. J., Uitenbroek, H., Clark, A., Coulter, R., Goode, P., & Cao, W. 2016, Sol. Phys., 291, 2243

Peres, G., & Reale, F. 1993, A&A, 267, 566

Peres, G., Serio, S., Vaiana, G. S., & Rosner, R. 1982, ApJ, 252, 791

Petschek, H. E. 1964, in AAS-NASA Symposium on the Physics of Solar Flares, ed. W. N. Hess (Washington, DC: NASA), 425

Petschek, H. E., & Thorne, R. M. 1967, ApJ, 147, 1157

Priest, E. 2014, Magnetohydrodynamics of the Sun

Priest, E., & Forbes, T. 2000, Magnetic Reconnection

Priest, E. R., & Forbes, T. G. 1986, J. Geophys. Res., 91, 5579

Priest, E. R., & Raadu, M. A. 1975, Solar Phys., 43, 177

Pritchett, P. L., & Coroniti, F. V. 2004, JGR, 109, 1220

Radziszewski, K., Rudawy, P., & Phillips, K. J. H. 2011, A&A, 535, A123

Reale, F. 2014, Living Reviews in Solar Physics, 11, 4

Reeves, K. K., Freed, M. S., McKenzie, D. E., & Savage, S. L. 2017, ApJ, 836, 55

Rosner, R., Tucker, W. H., & Vaiana, G. S. 1978, ApJ, 220, 643

Rutten, R. J. 2007, in Astronomical Society of the Pacific Conference Series, Vol. 368, The Physics of Chromospheric Plasmas, ed. P. Heinzel, I. Dorotovič, & R. J. Rutten, 27

Sanderson, T. R., Appourchaux, T., Hoeksema, J. T., & Harvey, K. L. 2003, Journal of Geophysical Research (Space Physics), 108, 1035

Savage, S. L., & McKenzie, D. E. 2011, ApJ, 730, 98

Savage, S. L., McKenzie, D. E., & Reeves, K. K. 2012, ApJ, 747, L40

Savage, S. L., McKenzie, D. E., Reeves, K. K., Forbes, T. G., & Longcope, D. W. 2010, ApJ, 722, 329

Schrijver, C. J., & Siscoe, G. L. 2010, Heliophysics: Space Storms and Radiation: Causes and Effects

Schrijver, C. J., & Siscoe, G. L. 2011, Heliophysics: Plasma Physics of the Local Cosmos

Scott, R. B., Longcope, D. W., & McKenzie, D. E. 2016, ApJ, 831, 94

Shay, M. A., Drake, J. F., & Swisdak, M. 2007, Phys. Rev. Lett., 99, 155002

Shen, C., Kong, X., Guo, F., Raymond, J. C., & Chen, B. 2018, ApJ, 869, 116

Silva, A. V. R., Wang, H., Gary, D. E., Nitta, N., & Zirin, H. 1997, ApJ, 481, 978

Solanki, S. K. 2003, A&A Rev., 11, 153

Solanki, S. K., & Steiner, O. 1990, A&A, 234, 519

Somov, B. V., & Kosugi, T. 1997, ApJ, 485, 859

Soward, A. M. 1982, Journal of Plasma Physics, 28, 415

Spruit, H. C. 1981a, A&A, 102, 129

Spruit, H. C. 1981b, A&A, 98, 155

Stenflo, J. O. 1973, Solar Phys., 32, 41

Sturrock, P. A. 1966, Nature, 211, 695

Sui, L., Holman, G. D., & Dennis, B. R. 2004, ApJ, 612, 546

Sweet, P. A. 1958, in IAU Symposium, Vol. 6, Electromagnetic Phenomena in Cosmical Physics, ed. B. Lehnert, 123

Syrovatskiĭ, S. I. 1971, Soviet Journal of Experimental and Theoretical Physics, 33, 933

Tsuneta, S., Masuda, S., Kosugi, T., & Sato, J. 1997, ApJ, 478, 787

Unverferth, J., & Longcope, D. 2018, ApJ, 859, 170

Unverferth, J., & Longcope, D. 2020, ApJ, 894, 148

van Driel-Gesztelyi, L., & Green, L. M. 2015, Living Reviews in Solar Physics, 12, 1

Vasyliunas, V. M. 1975, Rev. Geophys. and Space Phys., 13, 303

Veronig, A. M., Karlický, M., Vršnak, B., Temmer, M., Magdalenić, J., Dennis, B. R., Otruba, W., & Pötzi, W. 2006, A&A, 446, 675

Warren, H. P., Brooks, D. H., Ugarte-Urra, I., Reep, J. W., Crump, N. A., & Doschek, G. A. 2018, ApJ, 854, 122

Warren, H. P., O'Brien, C. M., & Sheeley, J., Neil R. 2011, ApJ, 742, 92

Yeates, A. R., Bianchi, F., Welsch, B. T., & Bushby, P. J. 2014, A&A, 564, A131

Yokoyama, T., & Shibata, K. 1994, ApJ, 436, L197

Yu, S., Chen, B., Reeves, K. K., Gary, D., Musset, S., Fleishman, G. D., Nita, G. M., & Glesener, L. 2020, ApJ, Submitted

Zirin, H. 1988, Astrophysics of the sun

Zwaan, C. 1987, ARA&A, 25, 83